STUDY OF Sn-Ag-Cu ALLOY RELIABILITY THROUGH MATERIAL MICROSTRUCTURE EVOLUTION AND LASER MOIRE INTERFEROMETRY

A Dissertation
Presented to
The Academic Faculty

by

Krishna Rajaram Tunga

In Partial Fulfillment
of the Requirements for the Degree
of Ph.D in the
School of Mechanical Engineering

Georgia Institute of Technology
August 2008

STUDY OF Sn-Ag-Cu ALLOY RELIABILITY THROUGH MATERIAL MICROSTRUCTURE EVOLUTION AND LASER MOIRE INTERFEROMETRY

Approved by:

Dr. Suresh K. Sitaraman, Chair
School of Mechanical Engineering
Georgia Institute of Technology

Dr. Arun M. Gokhale
School of Materials Science and Engineering
Georgia Institute of Technology

Dr. Richard W. Neu
School of Mechanical Engineering
Georgia Institute of Technology

Dr. Rao R. Tummala
School of Electrical and Computer Engineering
Georgia Institute of Technology

Dr. I. Charles Ume
School of Mechanical Engineering
Georgia Institute of Technology

Date Approved: [June 30th, 2008]

ACKNOWLEDGEMENTS

I would like to thank Dr. Suresh K. Sitaraman for providing me with an opportunity to pursue my studies at Georgia Tech and for keeping me funded throughout with assistantship. It has been a pleasure working under his guidance. I would also like to thank all my committee members - Dr. Richard W. Neu, Dr. Arum M. Gokhale, Dr.Charles I. Ume and Dr.Rao R. Tummala – for agreeing to serve as members of my thesis reading committee and for providing me with valuable suggestions and recommendations.

I had a great time working in Computer-Aided Simulation of Packaging Reliability (CASPaR) Lab all these years. Thanks to Andy Perkins for all the insightful discussions we have had on electronic packaging, solder joint fatigue and many other topics in general. I would like to thank Kevin Klein, Jamie Ahmad, Shashikant Hegde and Karan Kacker for all their help in various different ways throughout my study. Everyone from CASPaR Lab kept my morale high whenever things were not going as planned. I would also like to thank Melissa Raine for placing orders for research materials and ensuring that I received all the items in a timely fashion.

I would like to thank Mike Toole, Dean Sutter and Baik-Woo Lee from the Packaging Research Center for providing me assistance with various tools and equipment in the assembly Lab. Mike ensured that the thermal chamber and the reflow oven was functioning properly throughout my year long experiment schedule and was quick to

rectify any malfunction within a short notice. I would like to thank Arun Sreeranganathan for helping me with imaging the failed samples.

This research was funded by the US Army Research Office, Research Triangle Park, NC through contract W911NF-06-1-0304, IBM Corporation and NSF Packaging Research Center. I thank them for their financial support.

Finally, I thank my family for their constant love, encouragement and moral support all though my life.

TABLE OF CONTENTS

LIST OF TABLES

LIST OF FIGURES

SUMMARY

This research aims to understand the reliability of Sn-Ag-Cu solder interconnects used in plastic ball grid array (PBGA) packages using microstructure evolution, laser moiré interferometry and finite-element modeling. A particle coarsening based microstructure evolution of the solder joint material during thermal excursions was studied for extended periods of time lasting for several months. The microstructure evolution and particle coarsening was quantified, and acceleration factors were determined between benign field-use conditions and accelerated thermal cycling (ATC) conditions for PBGA packages with different form factors and for two different lead-free solder alloys. A new technique using laser moiré interferometry was developed to assess the deformation behavior of Sn-Ag-Cu based solder joints during thermal excursions. This technique can used to estimate the fatigue life of solder joints quickly in a matter of few days instead of months and can be extended to cover a wide range of temperature regimes. Finite-element analysis (FEA) in conjunction with experimental data from the ATC for different lead-free PBGA packages was used to develop a fatigue life model that can be used to predict solder joint fatigue life for any PBGA package. The proposed model will be able to predict the mean number of cycles required for crack initiation and crack growth rate in a solder joint.

CHAPTER 1

INTRODUCTION

1.1. Packaging Functions

Electronic packages contain hundreds to millions of transistors on a silicon chip in addition to many discrete components such as resistors, inductors and capacitors. All these different transistors and discrete components should be connected to each other and suitably powered to ensure optimal functionality and speed. With the technology increasingly being moved to the silicon chip level, protection of the silicon chip from outside environment and from shock and vibration is necessary. Increased functionality and increased power consumption also causes the electronic package to overheat. The package should be designed so as to provide adequate means for thermal heat dissipation and cooling. Thus electronic packaging has four main functions [1]:

- Signal distribution which involves topological and electromagnetic consideration.
- Power distribution, involving electromagnetic, structural and material consideration.
- Heat dissipation, involving structural and materials consideration.
- Mechanical, chemical and electromagnetic protection of components and interconnections.

1.2. Evolution of Electronic Packages

All technologies from the silicon chip level to the printed wiring board level collectively belong to the packaging hierarchy. A schematic of the packaging evolution from early 1970s to today is given in Figure 1.1 and Figure 1.2. Dual In-Line package (DIP) was the initial packaging technology started in the 1970s. In a DIP, the Input/Output (I/O) connections in the form of pins are arranged along the periphery of the package. The DIP had a very low silicon efficiency of about 2%. Silicon efficiency is defined as the percentage of the functional Printed Circuit Board (PCB) area taken by the silicon. The packaging technology has evolved significantly since then to meet the demands of higher signal speed, smaller package size, increased functionality for a given area and lower cost. To achieve higher I/O connection per package, the peripheral array evolved into an area array package known as Pin Grid Array (PGA) package. The Small Outline Package (SOP) was developed because of the cost benefits it offered. This later evolved into Quad Flat Packs (QFP) which allowed greater I/O connections per package.

All the packages mentioned above are through-hole packages which require drilling a hole in the PCB to assemble the packages. Through-hole packages leave significant amount of area on the back side of the board unutilized. Surface mount alternatives to these packages were developed in the 1980s. Surface mount packages, also known as Ball Grid Array (BGA) packages, used solder joints instead of pins to assemble the packages on the board. In addition to making available an increased board surface area for additional components placement, the solder joints also reduces the electrical parasitics significantly due to their smaller interconnect lengths. BGA packages have smaller form factors compared to through-hole packages. The BGA packages evolved

further in the 1990s to Chip Scale Package (CSP). In a CSP, a package size to silicon size ratio of 1.2 can be achieved.

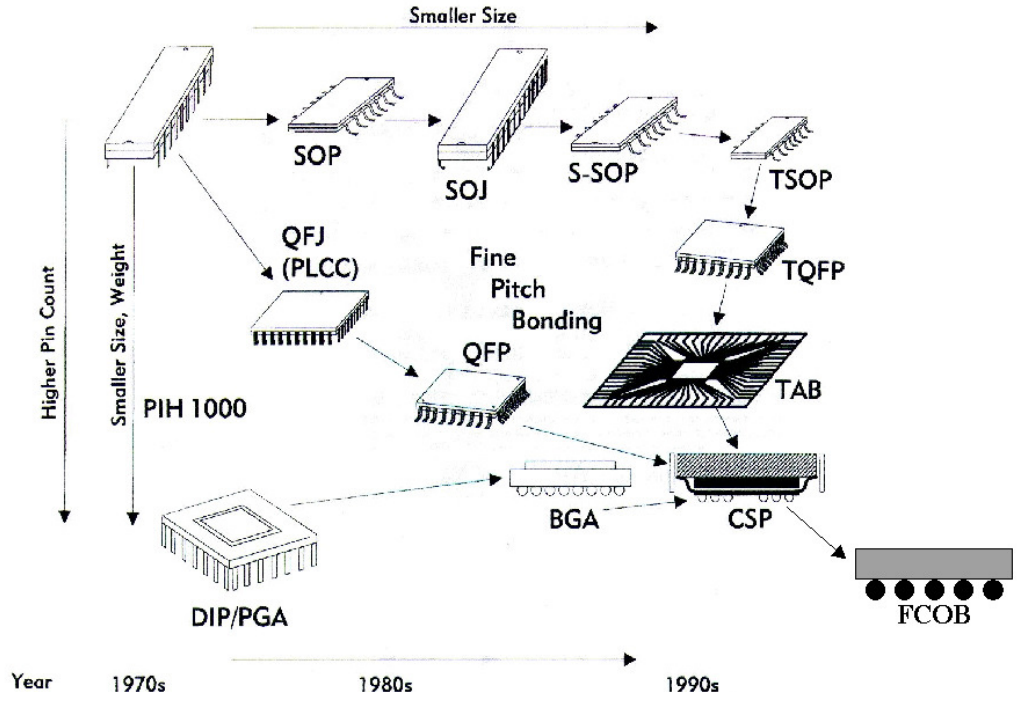

Figure 1.1. Evolution of electronic packaging technology [1]

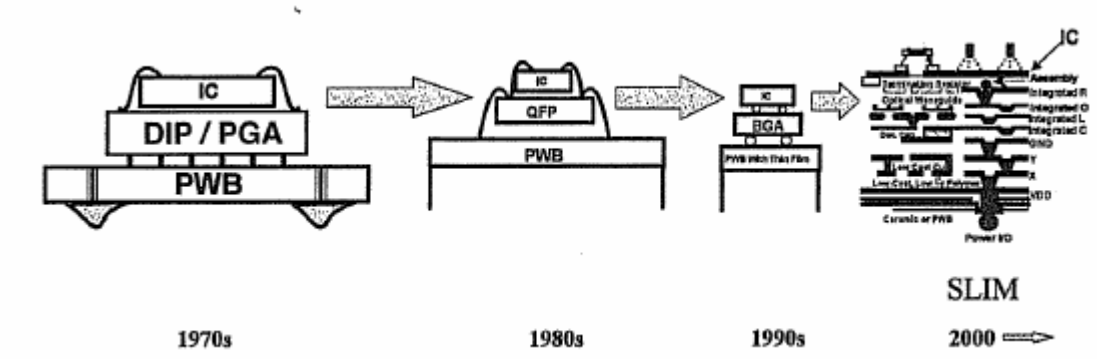

Figure 1.2. Packaging Evolution [1]

BGAs and CSPs meet most of the requirements of today's microelectronic industry's demands. A large number of variations exist within BGA and CSP package types. To name a few, the variations are based on the type of material used for the package substrate, the number of silicon chips in the package and the manner by which the silicon chips are assembled on the package substrate.

The BGA and CSP packages have evolved into Flip Chip On Board (FCOB) packages where the silicon chip is directly placed on the board. This reduces the number of levels in the packaging hierarchy to one, thereby increasing the signal speed significantly. However, increased difference in the thermal expansion coefficient between the silicon chip and the board leads to large number of reliability issues. Design considerations also require additional precaution to protect the silicon form outside environment.

Current state-of-the art in packaging technology is a single level integrated module (SLIM) as shown in Figure 1.2. This method allows inclusion of the silicon chips and discrete components into one single level module. Due to shorter interconnect lengths higher signal speed can be achieved compared to any surface mount package. BGA packages allow only placement of finite number of discrete components inside the package. The remaining discrete components have to be placed on the PCB. BGA packages can therefore achieve a silicon efficiency of only about 25%. SLIM, on the other hand, has the capability of achieving up to 75% of silicon efficiency. The SLIM technology is however still in the research stage at the Packaging Research Center (PRC) at Georgia Institute of Technology.

1.3. Plastic Ball Grid Array Packages

Plastic ball grid array (PBGA) package is a type of BGA package which is increasingly being used as a convenient low cost packaging solution. PBGA packages use an organic material as a package substrate. Variations exist within the PBGA packaging designs. Some of these variations include the face-up wire-bonded silicon chip configuration as shown in Figure 1.3 and stacked die configuration as shown in Figure 1.4. The location of the dies in the stacked die configuration is dependent on many factors including the electrical and mechanical requirements of the package. To reduce the interconnect signal delay, the face-up wire-bonded silicon chip can be replaced by the face-down solder bumped variant. For the present study a face-up wire bonded configuration was chosen. As the focus of the research is on the second level solder interconnections from the package to the PCB and not on the package itself, the methodology presented in this research can easily be extended to all other package configurations as well.

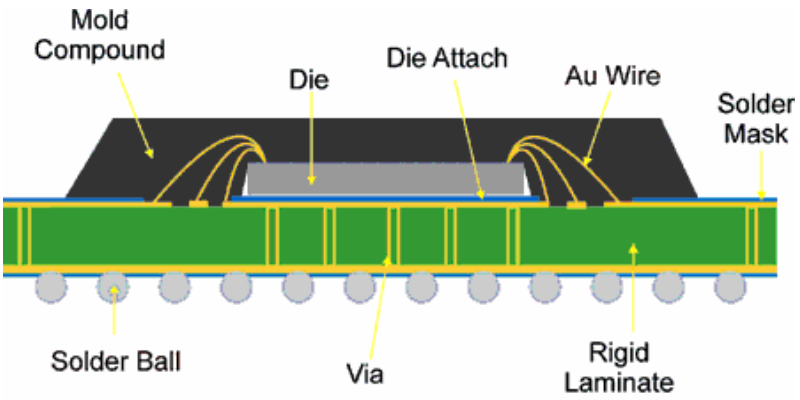

Figure 1.3. Schematic of a wire-bonded face-up silicon chip PBGA [Courtesy: Amkor®]

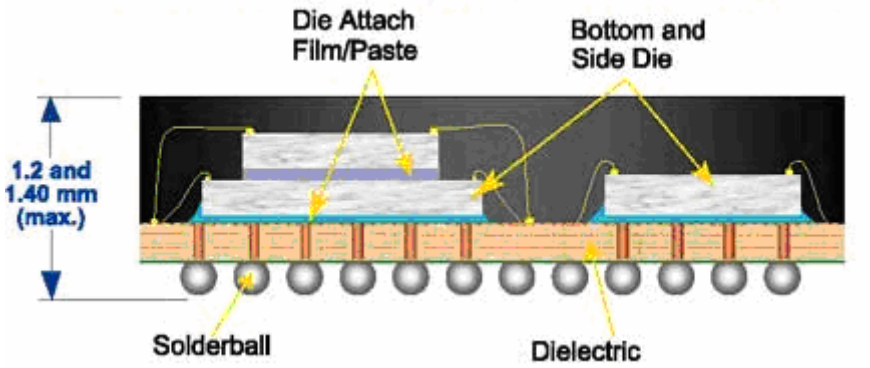

Figure 1.4. Schematic of a stacked die PBGA[Courtesy: Amkor®]

A three dimensional view giving the schematic of a PBGA package is shown in Figure 1.5. Bimaleimide Triazene (BT), polyimide and flame retardant fiber reinforced epoxy (FR4) are commonly used substrate materials in a PBGA package. The silicon chip is attached to the substrate using an epoxy based die attach material. The I/O pads on the chip are wire bonded to the I/O pads on top of the substrate. The chip and the wire bonds are encapsulated with a polymer mold compound. The mold compound protects the wire bonds and the silicon chip from moisture, ionic contaminants and hostile operating conditions such as vibrations and mechanical shock loadings. I/O pads on top of the substrate are routed out to I/O pads on the bottom of the substrate through multilayered copper traces and vias within the substrate. The I/Os on the bottom of the substrate are solder bumped thereby allowing the package to be reflowed and assembled onto a PCB.

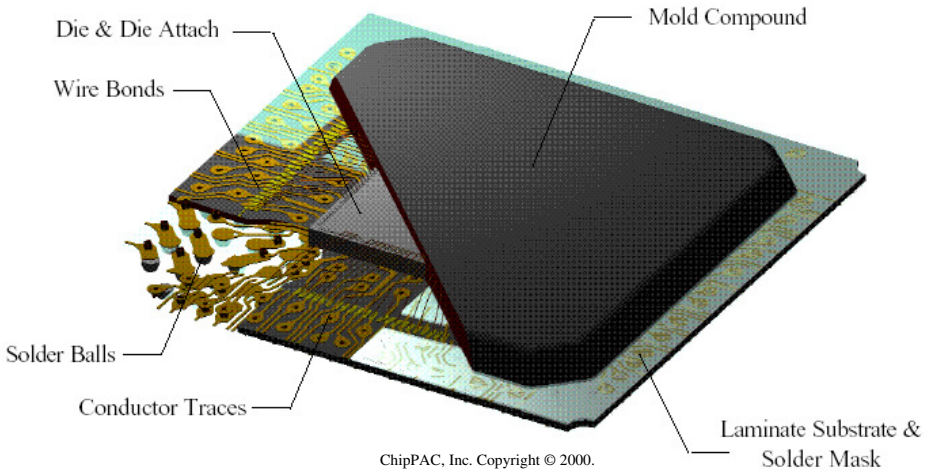

Figure 1.5. Plastic ball grid array package [Courtesy: ChipPAC incorporated]

PBGA packages are typically used for Static Random Access Memory (SRAM) applications, Application Specific Integrated Circuits (ASICs) and lower frequency microprocessors. The self aligning ability of ball grid array (BGA) packages ensures a very high yield with defect rates less than 1 ppm on a per-joint basis [2].

1.4. Lead Free Solders

The solder joints provide electrical connection between the BGA package and PCB and also provide mechanical support to the package. Tin-lead based solders have been used for the past few decades due to their low melting point and good mechanical properties. However, over the past few years, legislations in Europe and Japan have been passed banning the use of lead in any solder alloys due to potential environmental and health concerns. The European Commission's (EC) draft directive, Waste Electrical and Electronic Equipment (WEEE) and Restriction of Hazardous Substances (ROHS) have proposed the ban on lead in electronics by the 1st of July 2006. Legislation for banning lead in United States was proposed in 1989 but was dropped due to the then existing

small lead consumption by electronic industries and due to increased pressure from the electronic industry to retain lead based solders. The need for conversion to lead-free electronics in United States is therefore now driven by market competition. It is not possible to sell leaded products in Europe or Japan or in any country where the use of lead based products is banned. The conversion to lead-free electronics therefore seems imminent.

A consortium conducted by National Center for Manufacturing Sciences (NCMS) concluded that there is no drop-in replacement to lead-based alloys [3]. Sn based solder alloys with minor additions of Ag, Cu, Bi and Zn have been recommended by National Electronics Manufacturing Initiative (NEMI) and Japan Electronic Industry Development Association (JEIDA). Prominent among them were the Sn-Ag alloy for the wave soldering process and Sn-Ag-Cu (SAC) based solder alloy for reflow soldering process. NEMI has recommended Sn4.0Ag0.5Cu (SAC405) alloy [4] and JEIDA has recommended Sn3.0Ag0.5Cu (SAC305) for reflow soldering process [5]. SAC405 and SAC305 based alloys will be the focus of the present research.

Tin-lead solders have been used for the past few decades and their mechanical behavior is very well understood. Extensive legacy data related to their deformation behavior during thermo-mechanical loading is available. SAC alloy on the other hand is a relatively new alloy having about 35°C higher melting point compared to eutectic Sn-Pb solders [6]. The microstructure and mechanical behavior of SAC alloy is known to be very different from lead-based alloys. The microstructure of a typical Sn-Pb solder joint is poly-crystalline and consists of a uniform distribution of tin-rich and a lead-rich phase [7]. SAC based solder joints however have very few grains per solder joint (typically one

to ten) [8] and can be described as multi-crystalline. Sn has an orthogonal body centered cubic (BCC) lattice and therefore has an orthotropic coefficient of thermal expansion (CTE) and modulus [9-11]. With very few grains present in a solder joint, the mechanical behavior of a solder joint is expected to be not homogeneous. These Sn grains are made up of colonies of β-Sn dendrites and Sn-Ag-Cu eutectic. The Sn-Ag-Cu eutectic regions contain Ag_3Sn and Cu_6Sn_5 precipitates which offer resistance to creep deformation at low stresses [12]. At high stresses however, these precipitates do not seem to be effective enough and the creep deformation rate is known to be higher than that for eutectic Sn-Pb solder [12].

1.5. Fatigue Life Estimation

The integrity of the solder joint is very crucial to the reliability of the BGA packages during field-use conditions. During field-use conditions, the BGA package is subjected to different temperature regimes either due to the heat liberated from the functioning integrated chip (IC) or due to exposed ambient temperature. A BGA package is made of different materials having different CTE. Exposure to different temperature regimes causes the solder joints connecting the BGA package and the PCB board to undergo thermo-mechanical fatigue shear loading. The reliability of a solder joint under field-use for a solder joint is typically determined by subjecting the BGA package to an accelerated thermal cycling (ATC) testing characterized by increased ramp rates and temperature regimes. The life of the package when subjected to ATC can then be translated using an acceleration factor to the life of the package during field-use condition.

Significant amount of work done in the recent past few years have focused on developing a constitutive model for lead-free solder material at various temperatures [13-

16]. Some amount of work has also been done to formulate a fatigue predictive model for assessing its reliability [17-20]. However, very little work has been done to understand the microstructural evolution of lead free solders during ATC and field-use conditions. An acceleration factor that would relate the life of the package during ATC to life of the package during field-use conditions based on microstructure evolution would be more fundamental in nature when compared to phenomenological models.

Microelectronic packaging industry spends typically several months building and reliability testing prototype test vehicles. With the dramatic changes in the electronic packaging industry in terms of new package designs, new materials, wide variation of dimensions, aggressive lead time for development and testing, and reduced cost considerations, it is necessary to quickly assess the thermo-mechanical reliability of solder joints. Traditional fatigue life qualification method involves subjecting the packages to ATC and checking for daisy chain electrical continuity to determine the solder joint failure. In addition to daisy chain measurements, dye-and-pry technique is also widely used to determine the extent of crack propagation in various solder joints. Although ATC is being widely used, it suffers several shortcomings: 1) ATC typically takes more than three months to complete. 2) Whenever a package material or geometry or processing condition is changed, the ATC or other similar tests will have to be re-performed to understand the reliability implications, and thus valuable time is lost for each one of these design changes. Thus there is a compelling need for an alternative reliability assessment technique that is much faster than the current ATC testing and is still dependable for package qualification. Tests such as mechanical bending can accelerate the qualification time. However, they are usually done at room temperature,

and therefore, do not always capture the low cycle fatigue deformation behavior as observed during thermal cycling. Finite element analysis and laser moiré interferometry are two attractive choices that can help accelerate the qualification times for a newly designed package.

Finite-element models have been used in the past to determine the stresses and strains in the solder joints. These stresses and strains are commonly used in a predictive model to estimate the failure life of the whole package instead of a single solder joint [17, 21]. This result could be misleading. The solder joints in a package typically fail by crack initiation and crack propagation through the solder joint. Crack propagation accounts for significant fraction of life of a solder joint. Compressive stresses and strains in a solder joint can potentially hinder the crack growth rate and increase the life of the joint [22]. Existing predictive models for solder joint life prediction do not take the nature of the normal stresses and strains in a solder joint into consideration. There is a need to develop a predictive model that takes the results from experimental analysis (such as crack initiation and crack growth rate) and results finite-element analysis (FEA) (such as number of solder joint in a package and normal strains in the solder joint) to determine the life for a single solder joint.

Laser moiré interferometry has been used in the past by several researchers to measure the in-plane deformation of cross-sectioned electronic packages that are subjected to mechanical [23], thermal [24-26], concurrent vibration and thermal [27] and electrical power loading [28]. The technique can be easily applied to cross-sectioned solder joints to find deformation and hence the strain contours in the solder material. Researchers have used the laser moiré technique to measure deformation contours at

different temperatures and have used the contours to validate the FEA results. However, these strain contours have not been used to estimate the strain range during thermal cycling or to estimate fatigue life of solder joints. The solder joints experience complex multi-axial deformation behavior when subjected to thermal loading. Attempts to estimate the fatigue life and correlate the results with experimental thermal cycling data, taking into account the multi-axial nature of the strains in the solder joint, have not been done before.

1.6. Outline of the Thesis

Chapter 2 will present the background and literature review relevant to this work. The gaps in the existing research and the research objectives will be presented in Chapter 3. The microstructure evolution of lead-free solder joints during long term field-use thermal cycling will be discussed in Chapter 4. The microstructure evolution during accelerated thermal cycling and acceleration factor determination will be discussed in Chapter 5. In Chapter 6, the virtual reliability assessment of PBGA packages during accelerated thermal cycling will be described. The fatigue predictive model development using results from experimental thermal cycling and finite element analysis will be dealt with in Chapter 7. In Chapter 8 a procedure for fatigue life estimation of solder joints using laser moiré interferometry will be outlined. The contribution of the research work will be provided in Chapter 9. The possible future work will also be discussed.

CHAPTER 2

BACKGROUND AND LITERATURE REVIEW

The following sections outline details regarding SAC solder microstructure and the available methods in literature for its quantification. This will be followed by an explanation on the finite element modeling procedure. The constitutive models used for modeling the material behavior of solder joint and various other materials used in the package will be elaborated. The damage metrics used for fatigue life prediction of solder joints and the commonly used fatigue life predictive models and their drawbacks will be discussed. The final section will provide theoretical background on laser moiré interferometry. Phase shifting, which is a technique used for increasing the fringe counting accuracy of the laser moiré interferometry system, will be discussed towards the end.

2.1. Solder Microstructure Evolution

2.1.1. Lead Free Solder Microstructure

The BGA packages are assembled on a PCB using a reflow process with a cooling rate from melting temperature typically under 4°C/s. The presence of additional components on the PCB lowers the cooling rate even further to under 2°C/s. A typical solder joint exposed to such low cooling rates will have very few grains [8]. Each Sn grain is made up of colonies of β-Sn dendrites and Sn-Ag-Cu eutectic. The Sn-Ag-Cu eutectic regions consists of Sn, Ag_3Sn and Cu_6Sn_5 precipitates. These precipitates are in needle form and appear as particles in a cross-section image. Undercooling plays an

important role in the final microstructure of the solder alloy. Undercooling is a phenomenon where a substance retains its liquid state well below its freezing temperature. Sn is known to exhibit significant undercooling amounting to over 25°C [29, 30]. The Ag_3Sn and Cu_6Sn_5 precipitates on the other hand have very low undercooling amounting to only few degrees [30]. When cooled at a slow rate, some of these precipitates have sufficient time to grow in the form of plates [31], as shown in Figure 2.1, before Sn dendrites starts to nucleate. The locations at which the Ag_3Sn plates are formed are random and cannot be predicted.

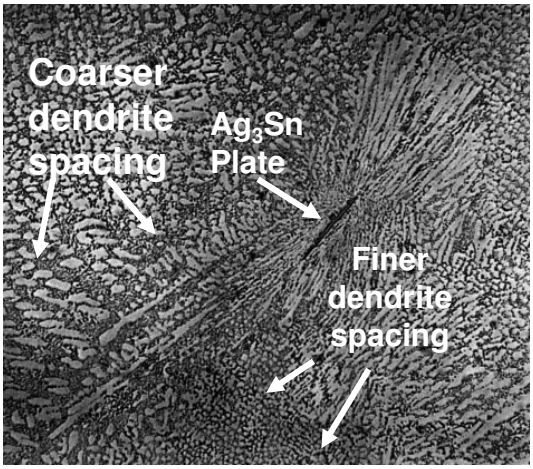

Figure 2.1. Dendrite spacing in a SAC solder joint [31]

2.1.2. Quantifying the Lead Free Solder Microstructure

There are different ways to characterize and quantify the microstructure of SAC alloy. These microstructural parameters can be monitored at regular intervals during ATC or field-use conditions and the reliability of the solder joint can be determined. The following are the possible parameters that can be used for monitoring microstructural evolution:

- Grain size

- Dendrite arm spacing
- Intermetallic growth at the solder joint and copper pad interface
- Ag_3Sn and Cu_6Sn_5 Particle coarsening

Grain boundaries store energy and when a solder alloy is subjected to thermo-mechanical loading, the grain tends to grow to lower the grain boundary surface area and hence the stored energy. The method however cannot be used to monitor the microstructure evolution for the SAC solder alloy because given the slow cooling rate, the solder joints have very few grains in a cross-section. Any increase in grain size will be too small to be detected.

Dendrite arm spacing is another metric used to quantify the microstructure. The dendrite arm spacing is not constant within a solder joint. It varies widely within a solder joint and around the Ag_3Sn plate region as shown in Figure 2.1. Moreover, Gibson et al [32], have also reported that aging at 120°C for 100 hours makes the solder joint lose its dendrite structure. Dendrite arm spacing can therefore not be used as damage metric to monitor microstructural evolution when we are interested in looking for hundreds of ATCs where the cumulative dwell time at higher temperature is significantly higher than 100 hours.

The copper pads on which the solder joints are reflowed usually have an organic protective coating to protect the copper pads from oxidation. During the reflow process, the solder alloy dissolves the organic protective coating and wets the copper pad. A Cu_6Sn_5 intermetallic compound (IMC) layer is then formed at the interface. This layer is known to grow significantly with ATC and has been used as a parameter to monitor

microstructure evolution [33]. Increased IMC growth, increases the chances of brittle failures. Therefore, the organic protective coating is now being replaced with Ni/Au under bump metallurgy (UBM). The Au acts as a protective coating preventing oxidation of the copper pad and Ni acts as a barrier preventing migration of copper from copper pads into the molten solder. This reduces the IMC thickness considerably. The IMC has $(Cu_xNi_{1-x})_6Sn_5$ composition [34] with Cu obtained not from copper pad but from migration from the solder alloy to the solder-Ni/Au interface. Subjecting the package to ATC leads to growth of the intermetallic compound. This growth rate is however considerably lesser than the growth rate observed when no Ni/Au UBM is used. Previous work [35] has shown that the $(Cu_xNi_{1-x})_6Sn_5$ IMC in a BGA package grows less than 10% when subjected to 3000 accelerated thermal cycles between -40°C to 125°C. For more benign field-use conditions, the IMC growth rate will be much slower than during ATC. These reasons make using the IMC growth rate as a parameter to monitor microstructure evolution for both ATC and field-use conditions not a good choice.

During ATC, the solder joints are subjected to high temperatures and high stresses due to CTE mismatches between the package substrate and the PCB. Under these conditions, the Ag_3Sn and Cu_6Sn_5 phases are known to coarsen at the solder-copper pad interface[36, 37]. A grain growth process from grain boundary diffusion theory proposed by Speight [38] and Ardell [39] was extended to phase growth process by Senkov and Myshlaev [40]. According to this theory, if atoms or vacancies diffuse mainly along phase or grain boundaries, the microstructure evolves such that the derivative of the fourth power of the average grain or phase size *d* is constant according to Equation 2.1.

$$(d^4)' = AD \tag{2.1}$$

where, d is the average diameter of the phase, A is a constant and D is a coefficient of solute diffusion in the phase boundary. Sayama et. al have performed microstructure evolution studies on lead-free solder used in surface mount resistors [36]. They have defined an Ag_3Sn phase growth parameter, S, and have observed that when subjected to periodic thermal loading, the phase growth parameter evolves linearly. The phase growth parameter is defined as given in Equation 2.2.

$$S = d^4 \tag{2.2}$$

The linear variation of the phase growth parameter can be expressed as shown in Equation 2.3.

$$S = A_1 N + S_o \tag{2.3}$$

where, S_o is the phase growth parameter before thermal cycling, S is the phase growth parameter after thermal cycling, A_1 is a constant and N is the number of cycles experienced by the package.

A drawback with the work done by Sayama et al is that, the microstructure evolution has been determined for only 1000 ATCs. When subjected to higher number of ATCs the linearity assumption might not be applicable. Dutta [37] has formulated an Ag_3Sn phase growth equation, shown in Equation 2.4, based on coarsening seen in Sn3.5Ag flip chip solder joints .

$$r \approx \left\{ \left[\left(\frac{B_1 \gamma_s V_m C_o}{RT} \right) \overline{D}_{sol} (t + 2N \dot{\gamma} t_{hc} v_c \phi) + r_o^3 \right]^{1/3} \right\} \qquad 2.4$$

where, r_o is the initial phase size, r is the phase size after v_c thermal cycles and time t. B_1, γ_s, V_m, C_o, $\overline{D}_{sol}$ and N are phase coarsening parameters. R is the universal gas constant, T is the temperature in absolute scale, $\dot{\gamma}$ is the shear strain rate experienced by the solder joint during thermal cycling, t_{hc} is the time period of half the thermal cycle and φ is the thermal cycling parameter. Dutta [37] has shown that the rate of coarsening decreases with thermal cycling. The formulation given in Equation 2.4 also has drawbacks. It does not take the alloy composition into consideration. The rate of coarsening might be different for alloys with different Ag content. Moreover, the equation applies for flip-chip solder bumps where the strains are mainly due to CTE mismatch between the silicon chip and the board. For plastic ball grid array (PBGA) packages, where the package substrate and the board both have similar CTE (about 17 ppm/K), the coarsening due to CTE mismatch between the solder joint material and the copper pads becomes important. Since, tin is an anisotropic material (CTE: 15 ppm/K to 30 ppm/K) and a solder joint has very few tin grains, the CTE mismatch between the solder joints and the copper pads might be a significant factor driving the phase coarsening in the solder joint in addition to the CTE mismatch between the package substrate and the board.

2.2. Finite Element Analysis and Fatigue Life Prediction

The fatigue life of solder joints is estimated through four stages as shown in Figure 2.2. The first stage involves determining the material property of the solder material and other materials used in the BGA package using experiments. The material

property should be cast in a form convenient for subsequent FEA. The elastic-plastic-creep and the elastic-viscoplastic formulations are the ones commonly used to model solder joints. Since the material of interest is solder joint, all other materials are modeled as either elastic or elastic-plastic. In the second stage, the finite element model of the BGA package which incorporates the material properties as mentioned above is constructed. For a quick trend analysis a 2D model is sufficient. But for a detailed analysis, a 3D model is necessary. If the package possesses symmetry, the 3D model can be simplified to a one-half, one-fourth or a one-eighth model. The finite element model is then subjected to cyclic thermal loading conditions and damage metrics are then extracted from the simulation results. Inelastic strain energy density (ΔW) and inelastic strain range ($\Delta\varepsilon$) are the damage metrics commonly used. These damage metrics are then used in a suitable predictive equation to determine the number of cycles for solder joint failure. The details regarding each of the above mentioned steps are elaborated below.

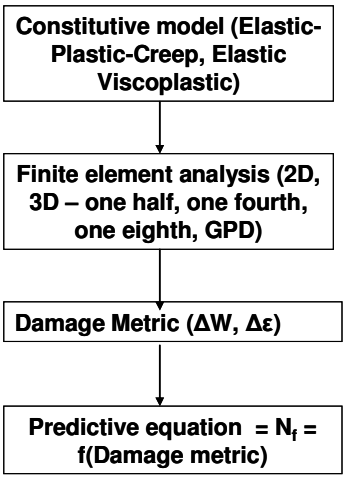

Figure 2.2. Steps used for solder joint fatigue life estimation

2.2.1. Constitutive Modeling of Packaging Materials

An electronic package is made up of various materials – polymer and metallic. The temperature range of interest for modeling purposes corresponds to the thermal cycling ranges experienced by the package. This range is typically between -55°C to 125°C. The constitutive behavior of some of these materials varies widely within this range and their variation with temperature should be taken into account.

All polymer based materials are modeled as linear elastic. The PCB board and the package substrate are typically composed of fiber reinforced epoxy laminates. This leads to different elastic properties in the out of plane direction. These two materials are therefore modeled as orthotropic. Silicon is a brittle material and has a high melting point of over 1500K. It is therefore modeled as linear elastic. Copper also has a high melting point. However because of its ductility, at high stresses, which typically occur at the copper pad-solder joint interface, there is a possibility for the copper material to exhibit local yielding. It is therefore modeled as an elastic-plastic material. Solder joints have a high homologous temperature even at room temperature. Materials with high homologous temperatures are known to exhibit significant time dependent creep deformation even at small loads [41, 42]. Due to its lower melting point and ductility, the yield strength of solder joints is also low making them easily susceptible to time independent plastic deformation. Solder joints are therefore modeled with either elastic-creep or elastic-plastic-creep properties. There has been some effort by researchers [43, 44] to combine the time dependent creep and time independent creep deformation behavior into a formulation that can be easily implemented in a FEA routine. Such combined formulations, known as unified viscoplastic formulation, make no assumption

of an explicit yield stress and hence plastic deformation is assumed to occur at all possible stress levels. The details regarding the unified viscoplastic formulation used for the present study will be outlined in the next section.

The material properties of all polymer materials vary widely between -55°C and 125°C. This is especially true if the glass transition temperature (T_g) falls within this temperature range. Temperature dependency is therefore taken into account to model any polymer based material. As mentioned before, solder joints typically have a low melting point of less than 230°C. Solder properties are therefore modeled as temperature dependent. Copper and Silicon have a very high melting temperature and their properties don't significantly change within the ranges of temperatures seen during thermal cycling. Temperature effect is therefore not taken into consideration to model these two materials.

2.2.1.1. Unified Viscoplastic Model for Solder

Anand's model [43] is one of commonly used unified viscoplastic model mentioned above. The model combines time independent plasticity and time dependent plasticity into one viscoplastic term. Although the formulation is complex, the entire material behavior model can be described by nine material parameters. The model can also be easily implemented in ANSYS commercial finite element software and takes a lot less execution time when compared to elasto-plastic-creep model. The viscoplastic strain rate is given by,

$$\dot{\varepsilon}_{vp} = Ae^{(-Q/RT)}\left[\sinh\left(\xi\frac{\sigma}{s}\right)\right]^{1/m} \qquad 2.5$$

where, $\dot{\varepsilon}_{vp}$ is the viscoplastic (inelastic) strain rate, A is a pre-exponential factor, Q is the activation energy, R is the universal gas constant, T is the current absolute temperature, σ is the current tensile stress, ξ is a multiplier of stress, m is the strain rate sensitivity, and s is the internal state variable whose evolution is described by,

$$\dot{s} = \left\{ h_o \left| 1 - \frac{s}{s^*} \right|^a \cdot sign\left(1 - \frac{s}{s^*} \right) \right\} \cdot \dot{\varepsilon}_p ; a > 1 \qquad 2.6$$

where h_o is the hardening/softening constant, a is the strain rate sensitivity of hardening/softening, and s^* is the saturation value of s associated with a given temperature/strain rate pair and is described by,

$$s^* = \hat{s} \left[\frac{\dot{\varepsilon}_p}{A} e^{(Q/RT)} \right]^n \qquad 2.7$$

where, $\hat{s}$ is a coefficient for saturation and n is the strain rate sensitivity for s saturation. The Anand's constants for the SAC405 alloy have been determined by Reinikainen et al [14] and are shown in Table 2.1.

Table 2.1. Anand's constants for the SAC405/SAC387 solder

Constant	Constant Value
s_o, MPa	1.3 MPa
$Q/R, K$	9000 K
$A, \sec^{-1}$	500 $\sec^{-1}$
ξ	7.1
m	0.3
h_o, MPa	5900 MPa
$\hat{s}, MPa$	39.4 MPa
n	0.03
a	1.4

2.2.2. Finite Element Analysis and Damage Metric Evaluation

Full 3D model gives an accurate representation of the behavior of the package. The computational time for running such a model is very high. However, if the 3D model possesses symmetry, the geometry size can be reduced by a factor of two, four or eight as shown in Figure 2.3a. The one-eighth model for a PBGA package is shown in Figure 2.3b. All the nodes at the left most edge are constrained with symmetry boundary condition. Finally, a single node at the bottom left-corner is constrained in all three directions to prevent rigid body motion.

The package is then simulated with several thermal cycles as seen during ATC. Damage metrics such as accumulated inelastic strain (or inelastic strain range), accumulated total strain (or total strain range) and accumulated inelastic strain energy density can be extracted for each solder joint per thermal cycle. The damage metrics are known to vary with mesh density. To obtain these parameters which are mesh independent, a volume averaging technique has been suggested to be suitable [18]. These volume averaged damage metric parameters can serve as an input to solder joint life estimation predictive models.

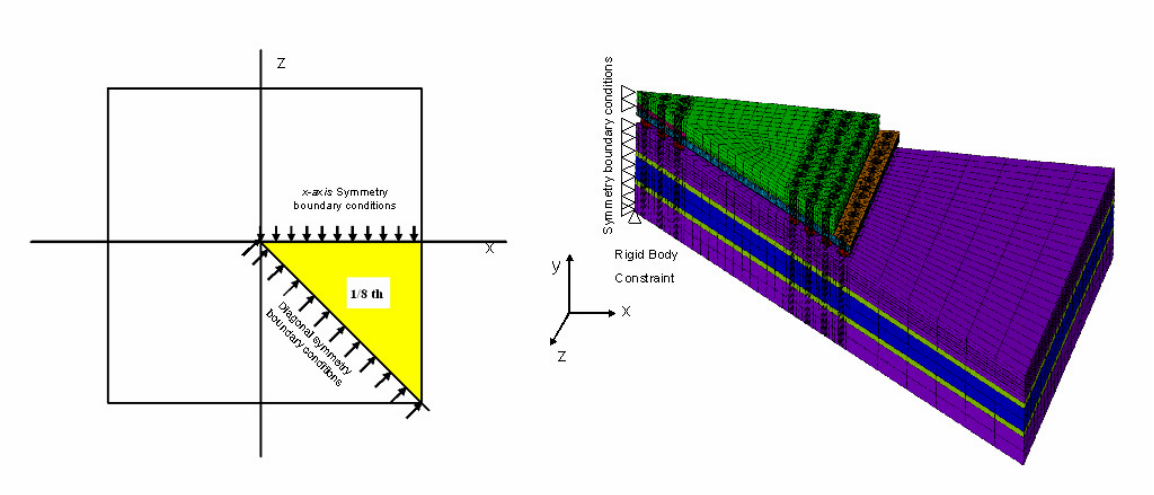

Figure 2.3. a) Slice of one eighth model b) One eighth finite-element model

2.2.3. Solder Joint Predictive Modeling

Predictive models are used to determine the fatigue life of a solder joint. Most fatigue models are of Coffin-Manson type as shown in Equations 2.8 and 2.9.

$$N_f = k_1 \Delta \varepsilon_{in}^{\ k_2} \qquad 2.8$$

$$N_f = k_3 \Delta W_{in}^{\ k_4} \qquad 2.9$$

where, N_f is the mean cycles to failure of the package, $\Delta\varepsilon_{in}$ is the volume averaged inelastic strain range, ΔW_{in} is the volume averaged inelastic strain energy density, k_1, k_2, k_3 and k_4 are constants. The constants for the above equations for the SAC405 alloy have been determined by Syed [17] and Pang et al [21, 45]. Syed found that for thermo-mechanical loading of SAC405 alloy, the contribution from creep strain to the total inelastic strain was over 95% for BGA packages. Hence, the constants have been determined by using volume averaged creep strain range and creep strain energy density as obtained from FEA with mean cycles to failure as obtained from experimental thermal cycling of BGA packages. The equations above have drawbacks. The damage metrics

used were obtained for a single solder joint. However, the number of cycles to fatigue failure was not for a single solder joint but for the whole package. A package consists of hundreds of solder joints. It is reasonable to suppose that the number of solder joints in a package has an effect on the life of the package. The effect of multiple solder joints is not taken into account in the above two equations.

Darveaux model [18] overcomes this problem by using the number of cycles for fatigue failure as obtained from experiments for a single solder joint. Darveaux model is an energy based model and uses accumulated inelastic energy density as a damage metric to find the number of cycles to failure. The accumulated inelastic energy density for an element can be found by Finite Element Analysis (FEA) and is given by Equation 2.10 [46].

$$\Delta W_{acc} = \sum_{i=1}^{NINT} \sum_{j=1}^{NCS} \{\sigma\}^T \{\Delta\varepsilon^{in}\} vol_i \qquad 2.10$$

where, *NINT* is the inelastic strain increment, *NCS* is the total number of converged substeps, σ is the current stress, $\Delta\varepsilon^{in}$ is the inelastic strain increment and vol_i is the volume of the element. The inelasticity mentioned in the above equation includes rate-dependent effects. If a combination of plasticity and creep models are used in the FEA, then the plastic strain and creep strain should be combined before using them in Equation 2.10. Under such case, the damage metric will be regarded as accumulated inelastic energy density.

Darveaux performed thermal cycling experiments on several ceramic BGA samples with Sn-Pb-Ag solder alloy [18]. At regular intervals few samples were pried off and the dye-n-pry technique was used to measure crack length in the solder ball during

thermal cycling. It was observed that the crack growth rate remains essentially constant during thermal cycling. The number of cycles for crack initiation was determined by extrapolation. Finite element models were built and the volume averaged inelastic energy density accumulated during one thermal cycle was output as a damage metric. The volume averaged accumulated inelastic energy density is given by Equation 2.11.

$$\Delta W_{acc,avg} = \frac{\sum_{element} \Delta W_{acc} \cdot V}{\sum_{element} V} \qquad 2.11$$

Where, V is the volume of a single element. This volume averaged damage metric obtained from FEA was then used to correlate the number of cycles for crack initiation and crack growth rate obtained from experiments according to Equations 2.12 and 2.13.

$$N_o = K_1 \Delta W_{ave,acc}^{K_2} \qquad 2.12$$

$$\frac{dx}{dN} = K_3 \Delta W_{ave,acc}^{K_4} \qquad 2.13$$

where, K_1, K_2, K_3, and K_4 are the constants which depends on the FEA mesh size used in the simulation, x is the crack length and $\Delta W_{ave,acc}$ is the average accumulated inelastic energy density. The constants has been provided by Darveaux [18]. For ceramic BGA packages, the crack growth rate was found to be fairly constant. For such cases, the number of cycles for crack propagation can be reduced to the form shown in Equation 2.14, where R is the radius of the solder joint.

$$N_p = \frac{2R}{da/dN} \qquad 2.14$$

The total number of cycles to failure is then given by Equation 2.15.

$$N_f = N_o + N_p \tag{2.15}$$

There are two drawbacks with Darveaux's predictive model. The model is based on experimental results from ceramic BGA packages with SnPbAg solder alloy. It is currently not known if Darveaux's model with uniform crack growth rate is applicable for PBGA packages with lead-free solder alloy. Even though, the effect of all the solder joints in the package to package life is not taken into account in any of the equations mentioned above, Darveaux has provided a de-rating factor that takes into account the effect of multiple critical solder joints in a package. This model is therefore superior to the model by Syed [17] and Pang et al [21]. However, for a PBGA package due to inherent lack of CTE mismatch between package substrate and the PCB, the difference in strains between the critical solder joint and other non-critical solder joint will not be significant. The effect of all the solder joints on the life of the package should therefore be taken into consideration.

2.3. Laser Moiré Interferometry

2.3.1. Theory of Laser Moiré Interferometry

Moiré interferometry is an optical method which provides whole field contour maps of in-plane displacements. A schematic diagram of the setting used for moiré interferometry is shown in Figure 2.4 [47] where coherent He-Ne laser beams are incident on the moiré grating having a cross-line pattern on the surface with a frequency of 1200 lines/mm. Sensitivity as low as 417nm per fringe order can be achieved with this setup. Coherent beams *A* and *B* when incident on the grating create a virtual reference

grating in their zone of intersection. When the specimen deforms, the grating also deforms with it. This deformed grating interacts with the virtual reference grating to produce the moiré interference pattern. The beams *A* and *B* when incident in the horizontal direction produces vertical fringes and these fringes are termed as *U* field fringes. Analogous beams when incident in the vertical direction would create another virtual reference grating which interacts with the second set of lines, perpendicular to the first one, to create the *V* field fringes.

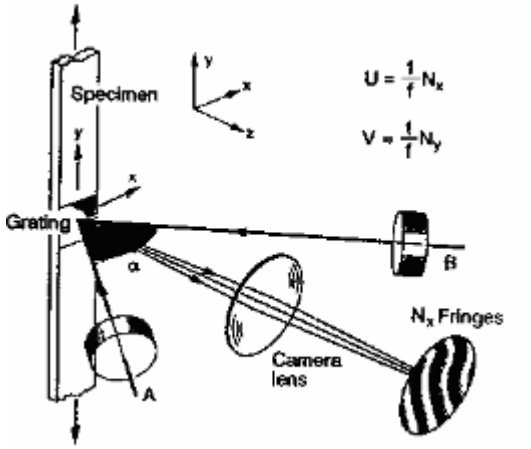

Figure 2.4. Schematic of laser moiré interferometry setup [47]

The displacements can then be determined from the fringes using Equation 2.16 [48].

$$U = \frac{N_x}{f}, \quad V = \frac{N_y}{f} \tag{2.16}$$

where, N_x and N_y are the fringe orders in the *U* and *V* field moiré patterns respectively. f is the frequency of virtual reference grating and is given by Equation 2.17,

$$f = \frac{2}{\lambda}\sin\alpha \tag{2.17}$$

where, λ is the wavelength of the laser light used for the coherent beam and α is the angle at which the coherent beam is incident. It should be noted that in moiré interferometry, the frequency of the virtual grating is related to the cross-line grating frequency using,

$$f_s = \frac{f}{2} \qquad 2.18$$

where f_s is the number of lines per millimeter length in the cross-line grating and is equal to 1200 lines/mm. When studying the deformation of the package as a whole, a sensitivity of 417nm/fringe order is sufficient. However, to obtain a more accurate deformation for small sized solder joints which exhibit higher strain gradients, higher fringe counting accuracy is needed. Various methods have been proposed to increase the fringe counting accuracy of the laser moiré interferometry system. Prominent among them are the immersion interferometer [49] and phase shifting technique [49, 50]. When used in combination, these methods have the capability to increase the fringe counting accuracy over tenfold [47]. Immersion interferometer requires the whole interferometer to be immersed in a liquid, typically water. This prohibits performing in-situ measurements of the package deformation. Phase shifting technique involves moving the whole interferometer parallel to the surface of the specimen and obtaining phase shifted fringes between the existing fringes thus increasing the fringe counting accuracy. The phase shifting process is done in a finite time interval and therefore care should be ensured to minimize the presence of vibrations.

2.3.2. Phase Shifting and O/DFM Method for Improved Fringe Counting Accuracy

Phase shifting is a method used to increase the fringe counting accuracy of the fringes obtained from laser moiré interferometry. The process involves moving the whole

interferometer parallel to the specimen grating in small increments, using a piezo-electric motor, so as to obtain interpolated fringes between the existing fringes. Moving the interferometer has an effect of moving the virtual reference grating parallel to the surface of the specimen. If the reference grating is moved by a distance *d* the change in phase of an existing fringe pattern is given by Equation 2.19 [49].

$$\Delta\phi = 2\pi df \qquad 2.19$$

where, *f* is the frequency of the virtual reference grating. If $d = 1/\beta f$, $\Delta\Phi = 2\pi/\beta$. By moving the interferometer in increments of *d*, fringe patterns with phase changing from 0 to 2π can be obtained. Phases 0 and 2π correspond to the same original fringe pattern before performing the phase shifting operation. Any phase between the existing fringe patterns correspond to an interpolated fringe pattern which can be used to improve the fringe counting accuracy.

If phase shifting is performed *n* times, *n* images are obtained which needs to be processed digitally into a single image for fringe counting. The original fringe pattern image and the phase shifted images might contain random noise thereby preventing combining these images digitally as it is. The noise needs to be eliminated by digital image processing. In addition, the digital image processing should also be able to sharpen the fringe pattern for clarity. Post et al [49] have proposed a digital image processing technique to combine two complementary fringe pattern images i.e. which are 180º degrees apart in phase, into one image. The processing algorithm helps eliminate noise and provides an option to sharpen the image to the desired level. If four phase shifted fringe patterns are available, they can be divided into two sets of complimentary image patterns. These two sets of complimentary image patterns can be combined, using the

image processing technique described by Post et al [49], to obtain two image patterns which are free from any noise effects. These noise-free images can then be easily combined digitally into a single image which has four times the fringe counting accuracy of the original fringe pattern.

The digital image processing technique outlined by Post et al [49] can be divided into three steps as given below.

- Subtraction
- Truncation
- Binarization

The fringe pattern image captured by a digital camera is typically a grey scale image with intensity ranging from 0 to 255. Black color corresponds to zero intensity and white color to 255. Any other shade of grey takes a value between 0 and 255. The two complimentary image patterns, $I(x)$ and $I^{\pi}(x)$, along with the non-uniform illumination and noise is shown in Figure 2.5. As can be seen from the Figure, the fringe patterns are affected by the presence of external noise. It is important to note that at points where both the complimentary fringe patterns have same intensity, the amount of attenuation due to noise and non-uniform illumination is same.

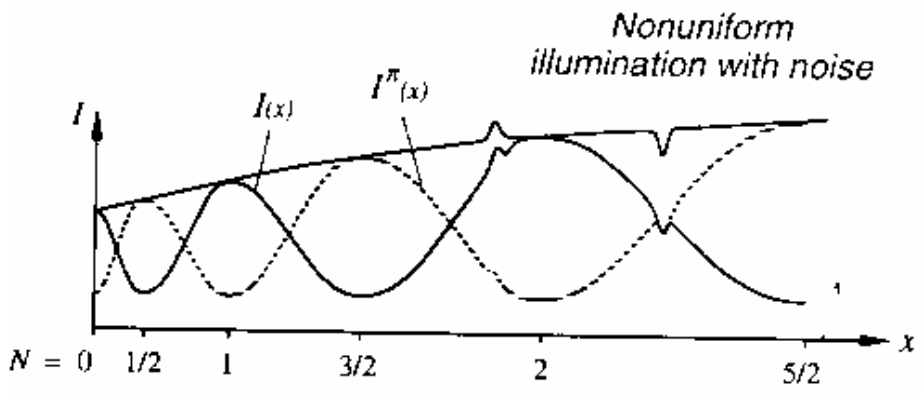

Figure 2.5. Complimentary fringe patterns

The first step involves subtraction of complimentary fringe patterns as shown in Figure 2.6. It can be seen that the influence of noise is cancelled at points where both fringe patterns have same intensity.

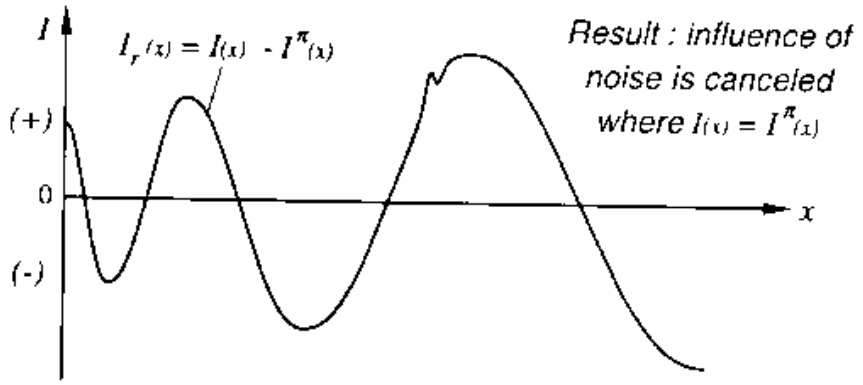

Figure 2.6. Subtraction of complimentary fringe patterns

The third step involves taking the absolute value of the intensity of the subtracted fringe pattern and truncating it at an intensity close to zero level intensity. The sharpness of the resulting fringe pattern can be controlled at this step. Lower the truncation threshold, sharper the resulting image will be. If the truncation threshold is too low

however, there is a possibility of losing the fringe altogether. So an optimal truncation threshold should be chosen.

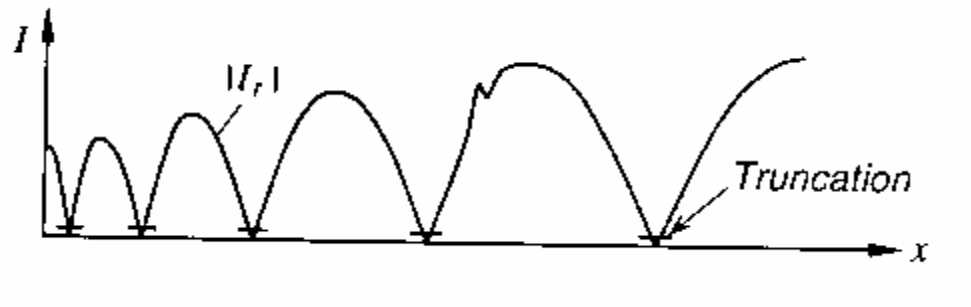

Figure 2.7. Truncation of the subtracted fringe pattern

In the final step, all intensities above the truncation threshold intensity are given a value of 255, which corresponds to the white level intensity. This step ensures that the dark fringes are observed against a white background thereby increasing the contrast and sharpness of the resulting fringe pattern.

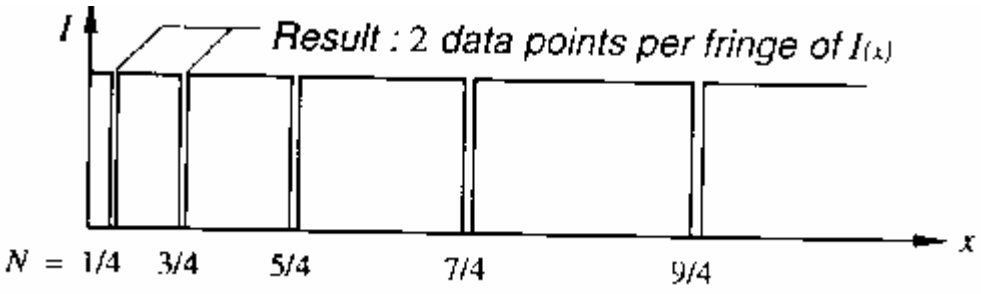

Figure 2.8. Binarization to obtain sharp fringes

2.3.3. Strain estimation

Using the deformation fringe patterns, the average in plane strains in a given region can be computed. The average normal strains are given by Equations 2.20 and Equations 2.21 [49].

$$\varepsilon_{xx} = \frac{\partial u}{\partial x} = \frac{1}{nf}\left(\frac{\Delta N_x}{\Delta x}\right) \qquad 2.20$$

$$\varepsilon_{yy} = \frac{\partial v}{\partial y} = \frac{1}{nf}\left(\frac{\Delta N_y}{\Delta y}\right) \qquad 2.21$$

where, N_x is the fringe order in the U field, N_y is the fringe order in the V field, Δy is the height and Δx is the width of the chosen region and n is the factor by which the fringe counting accuracy has been increased by phase shifting. ΔN_y is the number of fringes observed in the vertical direction and ΔN_x is the number of fringes observed in the horizontal direction. The average shear strain in a solder joint is given by Equation 2.22 [49]. It should be pointed out that the strains computed include thermal strains in addition to strains due to mechanical deformation and should therefore be subtracted before performing any further analysis.

$$\varepsilon_{xy} = \frac{1}{2}\left(\frac{\partial u}{\partial y} + \frac{\partial v}{\partial x}\right) = \frac{1}{2nf}\left(\frac{\Delta N_x}{\Delta y} + \frac{\Delta N_y}{\Delta x}\right) \qquad 2.22$$

.

CHAPTER 3

GAPS IN EXISTING RESEARCH, THESIS OBJECTIVES AND RESEARCH APPROACH

3.1. Gaps in Existing Research

The following sections outline some of the research gaps in the existing body of literature in the area of SnAgCu solder alloy reliability.

- The existing body of literature has not studied the microstructure evolution of SAC solder alloy over extended period of time, as in typical field-use conditions. Most of the available literature on SAC microstructure, although limited in scope has focused on ATC alone. Therefore, there is no existing study that compares the SAC solder microstructure evolution under field-use conditions and under ATC to be able to develop thermal cycling guidelines that will mimic field-use behavior.

- Unlike lead-based solder alloys, there are no widely-accepted fatigue life prediction models for SAC solder alloys. Also, the available models are limited in scope, and can predict only the mean cycles to solder joint failure. The existing models do not account for crack initiation and crack propagation in SAC solder alloys. Furthermore, the existing models only consider damage metrics such as inelastic strain or plastic work density to determine the fatigue life

without considering whether the solder joints are under compressive or tensile loading conditions

- Given that ATC takes a lot of time, lasting few months, existing body of research has not developed experimental techniques to assess reliability in an accelerated fashion. Isothermal mechanical flexing has been employed by some researchers to accelerate SAC solder alloy qualification. However, such isothermal mechanical flexing is not representative of the thermo-mechanical loading seen in actual solder joints. Furthermore, mechanical flexing cannot assess the reliability of solder joints under a wide range of temperature conditions without repeating the experiments for a number of temperature conditions.

3.2. Research Objectives

Given the above gaps in the existing body of literature, this research study aims to study Sn-Ag-Cu solder alloy thermo-mechanical reliability and microstructure evolution under long-term thermal excursions and accelerated thermal conditions. The research also aims to develop a suitable predictive equation for fatigue life estimation during ATC and to develop an expedient laser-moire based technique to assess thermo-mechanical reliability of solder joints. In particular, this proposal has the following specific objectives:

- To study the microstructure evolution of SAC solder alloy under thermal excursions over an extended period of time and to develop correlations or acceleration factors between field-use thermal excursions and ATC, using microstructure evolution over long thermal excursions as well as ATC.

- To develop a reliability predictive model to determine crack initiation and propagation in SnAgCu solder alloy by performing accelerated thermal cycling experiments, and thus to estimate the thermal cycling fatigue life of the package. Such a predictive model should take into account the effect of compressive strains in the solder joints and the effect of multiple solder joints on package life.

- To develop a laser moiré interferometry based experimental technique to quickly assess the thermal cycling fatigue life of SAC solder alloy, and to employ the technique to cover a wide range of temperatures without having to repeat the entire suite of laser moiré experiments.

3.3. Research Approach

The following sections outline the research approach that will be followed to achieve each of the objectives mentioned above.

3.3.1. Study of Microstructure Evolution over Extended Thermal Excursions

Three different PBGA package types with different lead-free SAC alloy compositions will be assembled on organic printed circuit boards, and these assemblies will be subjected to a typical field-use condition characterized by extended period of thermal excursion per cycle. Field-use thermal cycling involves thermal cycling between room temperature and 90°C with 4-hour dwell time at each of the temperature extremes. Eight samples for each package type will be used. Two PBGA samples will be taken out at various intervals ranging between 0 days to 90 days of thermal cycling. The packages will be molded, cross-sectioned along the centerline and polished to reveal the solder microstructure. High magnification SEM images will be taken near the solder joint and

copper pad interface. The particle coarsening and phase growth will be quantified and will be monitored during field-use thermal excursion.

3.3.2. Correlation of Microstructure Evolution between ATC and Field-use

The same PBGA package types used for the extended thermal excursion study will be assembled on organic boards and will be subjected to ATC. ATC involves thermal cycling between -55°C to 125°C with 15 minutes dwell at either temperature extremes. The electrical failure of the packages during ATC will be monitored. The packages will be taken out of the ATC thermal chamber at regular intervals between 0 cycles and about 4000 cycles and cross-sectioned along the centerline to reveal the solder bumps. Two packages of each type will be used for a given interval. The particle coarsening and phase growth parameter will be measured and quantified for the outermost solder bumps along the centerline. The phase growth parameter during field-use conditions as determined from the previous study will be used to determine the acceleration factor for solder joint failure in each package type during ATC.

3.3.3. Development of Predictive Model for Crack Initiation and Crack Propagation

Finite element models for three different packages will be built taking into consideration the symmetry of the package. The packages will be simulated with similar thermal cycling loading conditions as experienced during ATC. Damage metrics such as accumulated volume averaged inelastic work (ΔW_{acc}), accumulated inelastic strain range ($\Delta \varepsilon_{in}$) and accumulated total strain range ($\Delta \varepsilon_{tot}$) will be obtained for all the solder joints along the centerline of the package. Along with these damage metrics, the volume averaged normal strains in the out of plane direction will be extracted from the model.

In conjunction with the FEA, two different BGA package types will be subjected to ATC between -55°C to 125°C with 15 min dwell at either temperature extremes. These packages will be taken out from the thermal chamber at regular intervals and will be cut along the center line. The cut package will be polished to reveal the cross-section of the solder bumps along the center line. The length of cracks will be inspected for all the solder joints below the die shadow and package edge.

The results from the experimental crack analysis and FEA will then be used to formulate a predictive equation that takes into account the normal strains in the solder joint and the number of solder joints in the package, in addition to the three damage metrics mentioned above, to estimate the fatigue life of a package. The third package type, which is different from the two package types used for the experimental crack growth study, will be used for verifying the developed predictive model.

3.3.4. Development of a New Approach to Assess ATC Fatigue Life through Laser Moiré Contours

As part of the fourth objective, the in-plane deformation for a PBGA package assembly with SAC405 lead-free solder will be determined at various temperature regimes. The PBGA package assembly will be cut along the centerline of the package in a direction parallel to one of the sides of the square package. The cut package will be then ground and polished so as to expose half a row of solder balls. Grating, with 1200 lines/mm will then applied on the polished sample at room temperature. As discussed before, this grating gives a sensitivity of 417 nm/fringe order. An epoxy material will be used to adhere the grating to the sample. The sample will then be subjected to different temperature regimes in a thermal chamber. The deformation fringes on the grating

observed due to temperature excursion can be captured in-situ using a lens and a CCD camera. Phase shifting method will be used to increase the fringe counting accuracy by fourfold. The strains obtained from the experiment will be used along with the equation determined as part of the third objective to estimate the fatigue life of the solder joint.

3.3.5. Extension of Laser Moiré Approach to Assess ATC Fatigue Life over a number of Thermal Regimes

As part of this objective, the same PBGA package used for the previous study will be subjected to thermal excursion between -55°C and 125°C at a rate of 5°C/s. The sample will be dwelt at intermediate temperatures between these two extremes for 15 minutes and the deformation contours will be measured. The intermediate temperatures chosen for the study will be: 0°C, 65°C and 100°C. Once the contours at these temperatures are obtained, the equivalent strain range between all possible combinations of temperatures will be determined. Fatigues lives can then be easily assessed from the respective strain ranges.

CHAPTER 4

MICROSTRUCTURE EVOLUTION DURING EXTENDED DURATION THERMAL EXCURSION

This chapter discusses the phase coarsening based microstructure evolution of SAC305 and SAC405 based solder alloys used in PBGA packages when subjected to long term extended thermal excursions. To experimentally study the microstructure evolution, three different package types were assembled on an FR4 board and the as-reflowed microstructure recorded. The packages were also subjected to 90 days of field-use thermal cycling, taken out at regular intervals and cross-sectioned to quantify the microstructure evolution. Variation of the microstructure with days of thermal cycling has been plotted for different package configurations. The plots can be used to develop a relationship between the particle growth and thermal excursion.

4.1. Package Assembly

The three different package types that were used for the study are shown in Table 4.1. PBGA 676 is a large size package with higher standoff height and larger solder volume. PBGA 160 is a small size package with a lower standoff height and smaller solder volume. Both packages had solder joints with 1.0mm pitch. The footprints of PBGA 676 and PBGA 160 packages are shown in Figure 4.1.

Table 4.1. Package types used for the microstructure evolution study

Package Type	I/O count	Solder Alloy	pitch (mm)	Solder Volume(mm^3)	Stand off (mm)	Die size (mm x mm)	Package size (mm x mm)
PBGA	160	SAC405	1.0	0.067	0.30	6.3 x 6.3	15 x 15
PBGA	676	SAC405	1.0	0.119	0.43	6.3 x 6.3	27 x 27
PBGA	676	SAC305	1.0	0.119	0.43	6.3 x 6.3	27 x 27

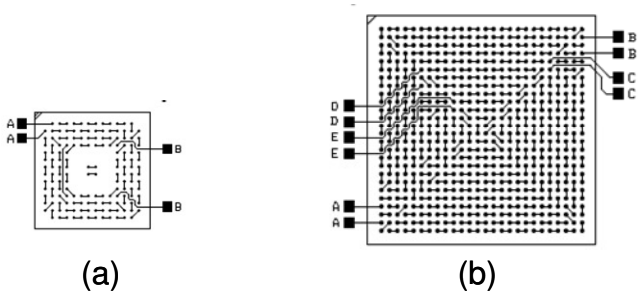

Figure 4.1. Footprints of (a) PBGA 160 and (b) PBGA 676 package

A schematic of a PBGA package is shown in Figure 1.3 and Figure 1.5. The package consists of a face-up silicon chip which is attached to the organic substrate below using a die-attach material. The pads on the silicon chip are wire-bonded to the pads on the package substrate. The chip and the wire bonds are over molded to protect them from outside environment. The copper pads on top of the package substrate are connected to the copper pads on the bottom of the substrate through vias. The copper pads at the bottom of the substrate are solder bumped with either SAC305 or SAC405 alloy. All the packages had Ni/Au under bump metallization on the package side copper pads. The copper pads on the package side were solder mask defined.

The packages were manually assembled on a single layer 1.5 mm thick FR4 board having Ni/Au under bump metallization on the copper pads. The copper pads on the board were non-solder mask defined. Tacflux 20B by Indium Corporation was applied on

the FR4 board before package placement. The packages were reflowed in a reflow oven having seven temperature zones maintained at different temperatures. The reflow profile recommended by Indium Corporation [51] was used for the study. The temperature was monitored by attaching a thermocouple near the package edge on the board. The measured thermal profile is shown in Figure 4.2. The melting point of the solder alloy was 217°C. The ramp rate during heating was about 0.75°C/s. The maximum temperature reached in the reflow oven was 248°C. The time above liquidus was 60s and the cooling rate was about 2.5°C/s. All packages were daisy chained so that the daisy chain electrical resistance could be monitored during thermal cycling. The resistances of the packages were measured soon after reflow to ensure that the package assembly was successful. A failure in any of the solder joint would lead to increase in the measured daisy chain resistance. Successfully assembled packages were either cross-sectioned to reveal the as-reflowed microstructure or subjected to thermal cycling.

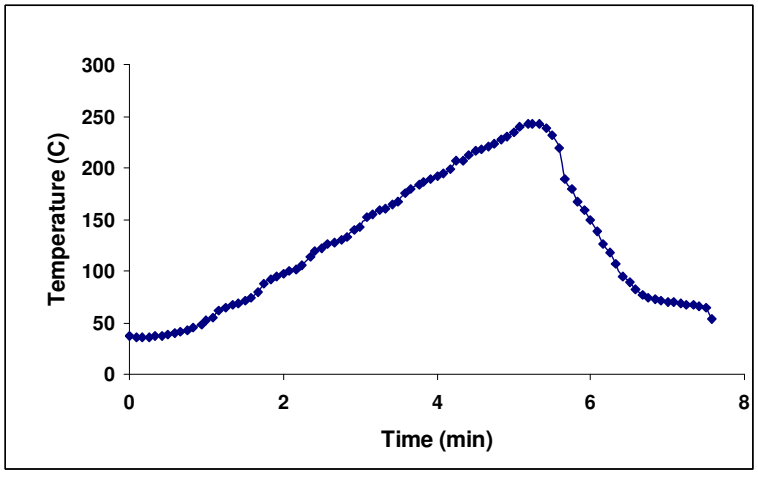

Figure 4.2. Temperature measured on a FR4 board

4.2. As Reflowed Microstructure

To observe the as-reflowed solder microstructure, the packages were molded in an acrylic compound and cross-sectioned to reveal the solder bumps. Cross-sectioning without molding might lead to failures in the package due to the cutting process. The cross-sectioning can be done either along the package diagonal or at the centerline parallel to the package edge. However, mounting and cutting the package along the diagonal is difficult. Therefore all cross-sections were taken along the centerline of the package, parallel to the package edge. A PBGA 160 package before and after molding is shown in Figure 4.3.

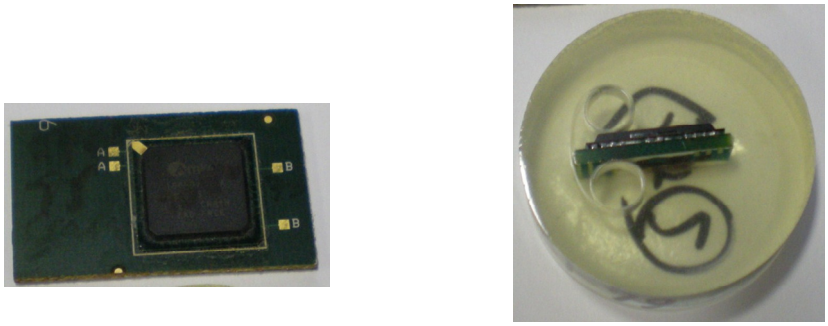

Figure 4.3. PBGA 160 package a) before molding and b) after molding

The cross-sectioned package was grounded on a silicon carbide grinding sheet to reveal the solder joints along the centerline. The ground package was then polished in a 1μm alumina suspension to get rid of the scratch marks on the solder joints and to obtain a clean smooth surface. Polishing in an alumina suspension does not reveal the precipitates. To reveal the precipitates, the package was again polished in an alkaline 0.05μm silica suspension. The alkaline solution preferentially etches the tin grains at a

higher rate and therefore helps to clearly identify the Ag_3Sn precipitates. To maintain consistency between samples, the etching was performed for 8 minutes on all samples. A typical microstructure of three cross-sectioned neighboring solder joints as observed in a polarized light microscope is shown in Figure 4.4. It can be seen from Figure 4.4 that the number of grains per solder joint is very few and that these grains are randomly oriented within the solder joint. The number of grains per cross-section measured from 50 solder joints for each package types is shown in Table 4.2. It can be seen that lower solder volume has an effect of lowering the number of grains per cross-section and hence the whole solder. The composition of the alloy is seen not to have a significant effect on the number of grains per solder cross-section.

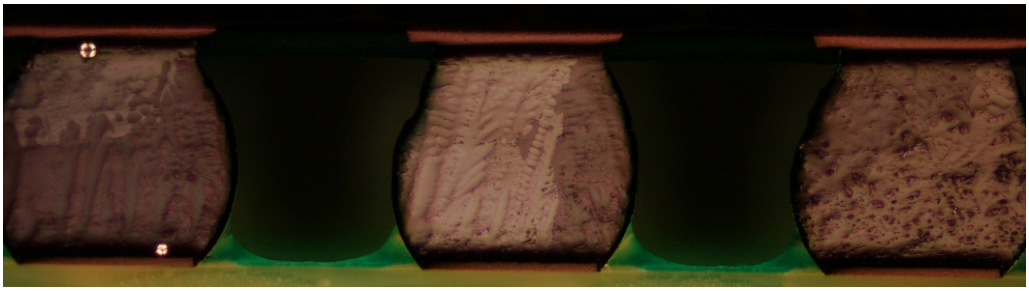

Figure 4.4. As reflowed solder joints observed in a polarized microscope

Table 4.2. Number of grains per cross-section

Package Type	Average grains per solder cross-section (50 joints)	Solder Volume
PBGA160 – SAC405	1.54±0.787	0.067mm^3
PBGA676 – SAC405	2.60±1.80	0.119mm^3
PBGA676 – SAC305	2.96±1.77	0.119mm^3

A scanning electron microscope (SEM) image of the solder cross-section near the package side for PBGA 676 with SAC405 alloy is shown in Figure 4.5. The image

reveals that the microstructure is made of β-Sn dendrites and Sn-Ag-Cu inter-dendritic eutectic. The Sn-Ag-Cu eutectic region consists of β-Sn, Ag_3Sn and Cu_6Sn_5 intermetallic compounds. The dendrite arm spacing was found to be similar for all three different package configurations. The size of the intermetallic compounds was found to vary between package configurations. The quantification of particle size after reflow will be outlined in the following section.

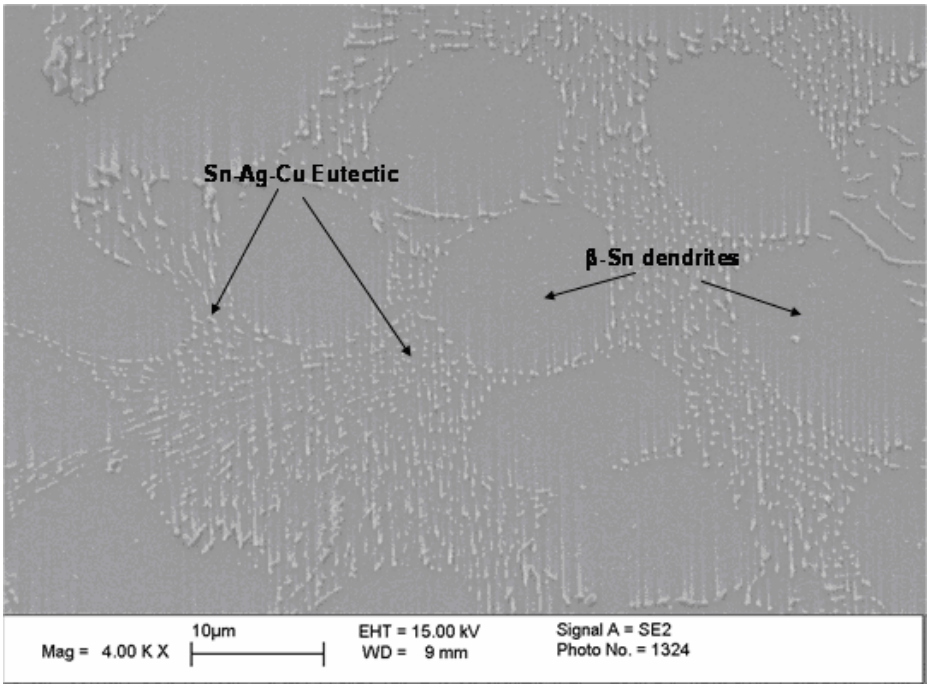

Figure 4.5. SEM image of the cross-sectioned solder joint

4.2.1. Image Analysis

Unlike flip-chip packages, plastic BGA packages are not characterized by high CTE mismatch between the package substrate and the FR4 board. Therefore, the variation of strain between neighboring solder joints is not very high. To monitor the as reflowed phase size and phase growth during thermal cycling, three outermost solder

joints, along the centerline of the package parallel to the package edge, were monitored together for microstructure evolution. The coarsening of the particles in the inter-dendritic eutectic region was monitored to quantify the microstructure evolution.

All images were taken using an SEM as it offers higher magnification ability and greater depth of focus when compared to an optical microscope. All commercially available image analysis software uses the grey scale level of the precipitates to identify the particles and to determine their sizes. The particles in an SEM image do not have a distinct grey scale level compared to its background. The particles were therefore identified manually as shown in Figure 4.6. ImageTool software was then used to analyze the image and to obtain the average particle size for the entire image. A 50μm x 60μm area at the corner of the solder neck region at the package side was chosen for microstructure quantification. As will be discussed in the next chapter, the size of the region was chosen based on the observation that coarsening occurred in a localized region near the package-solder interface. This process was repeated for all the three outermost solder joints along the centerline of the package at both the solder neck corner regions as circled and shown in Figure 4.7. Totally twelve images needs to be analyzed per package type to obtain the average phase size.

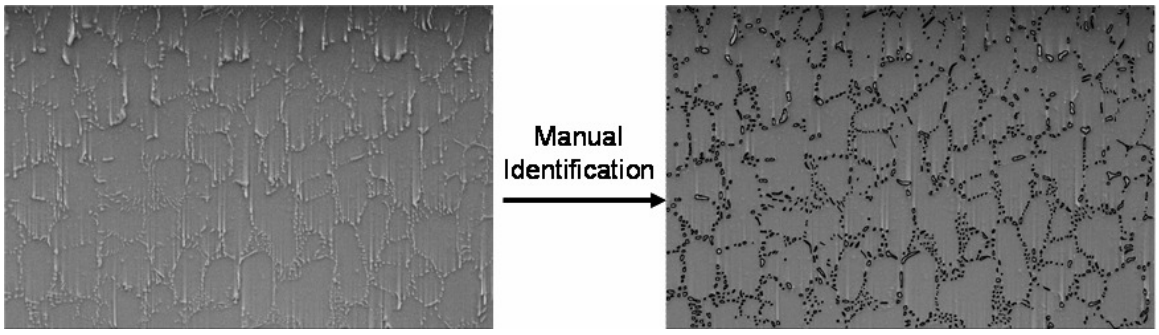

Figure 4.6. Manual identification of the particles

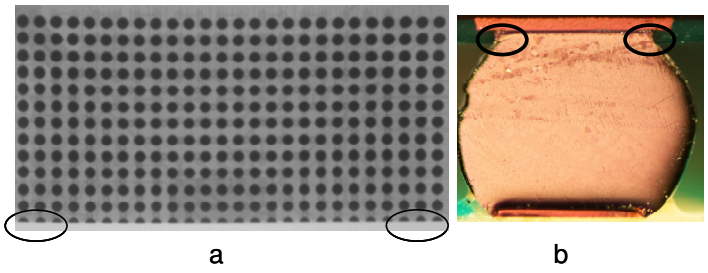

Figure 4.7. a) X-ray image showing the outer most solder joints along the center line of the package b) Corners of the solder joint neck region at the package side

4.2.2. Microstructure After Reflow

The average Feret diameter of the Ag_3Sn phase size just after reflow was measured for all the three package types and is shown in Figure 4.8. All phases observed were mostly convex in shape. However, if the phases were concave in shape, a mean intercept method[52] should be used to measure the size of the phases. PBGA 676 package with SAC405 alloy has a higher average phase size when compared to the one with SAC305 alloy even though they both have the same solder volume. SAC405 alloy has higher amount of Ag (4%) available in the solder joint when compared to the SAC305 alloy (3%). Sn is available in plenty in both alloys. The size of the Ag_3Sn precipitate is therefore determined by the amount of Ag in the solder alloy. The higher Ag content available in the SAC405 alloy makes the Ag_3Sn precipitates grow to a larger size after reflow. PBGA 676 package with SAC405 alloy has a higher average phase size when compared to PBGA 160 package with SAC405 alloy. PBGA 676 is a large size package, has higher number of I/Os per package and has large solder volume compared to the PBGA 160 package. The PBGA 676 package therefore has a higher heat capacity compared to PBGA 160 package and therefore experiences slower cooling rate during

reflow. The slower cooling rate allows the Ag_3Sn precipitates to grow thereby leading to larger phase size.

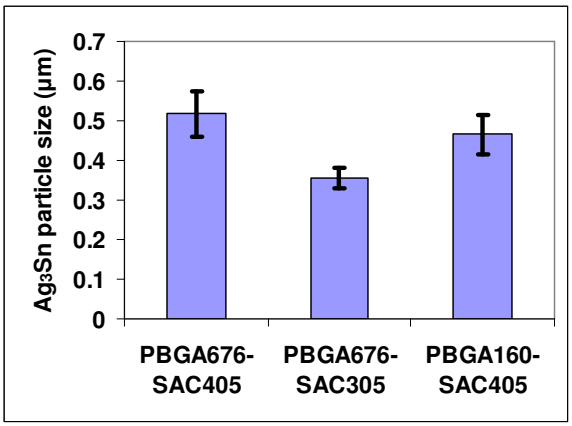

Figure 4.8. Average Ag_3Sn particle size after reflow

The average phase growth parameter *S*, as given in Equation 2.2, after reflow for all three package types is shown in Figure 4.9. The phase growth parameter is obtained by taking the fourth power of the phase size. This magnifies the deviation seen in the measured phase growth parameter between different package types. The deviation in the initial phase growth parameter is very substantial for the PBGA 676 package with SAC405 alloy. The same package with SAC305 alloy exhibits significantly lesser deviation.

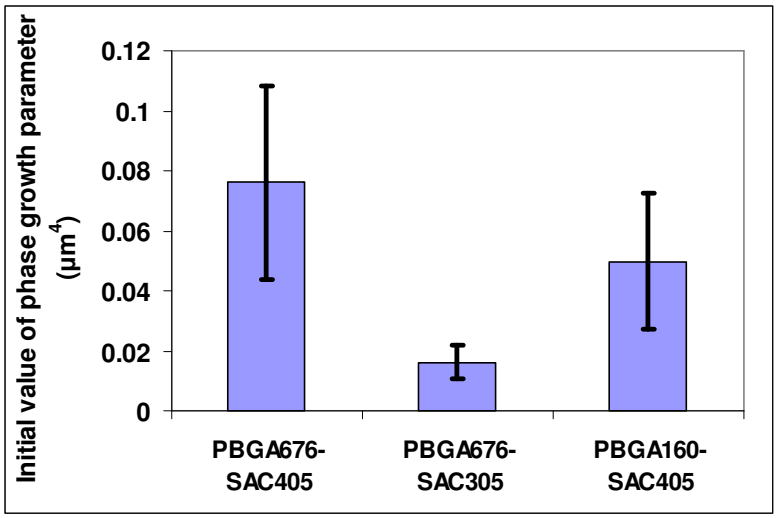

Figure 4.9. Average Ag_3Sn phase growth parameter after reflow

4.3. Field-use Thermal Cycling

During field-use, a package can be subjected to various thermal cycling conditions. All these thermal cycling profiles tend to be benign when compared to ATC. For this study, a simplified profile was used to determine the microstructure evolution of the solder alloy material when used in a desktop computer. The silicon chip in the package is typically designed so as to function optimally under 85°C [53]. The maximum temperature during field-use thermal cycling was therefore assumed to be 90°C to be slightly more conservative. Assuming that the desktops in which these packages are used are typically switched off and on three times a day, the packages were subjected to a thermal cycling frequency of three cycles per day. The field-use thermal cycling that was used therefore involved thermal cycling between room temperature and 90°C with four hour dwell time at either temperature extremes. The packages were kept in a heating oven and the temperature of the oven was increased to 90°C at a rate of 5°C/s to mimic the heating that occurs in a package used in a desktop computer. After four hours dwell at

90°C, the oven was switched off for four more hours to allow the package to cool down back to room temperature. The temperature profile monitored in the thermal chamber during field-use is shown in Figure 4.10. Cooling of the package was seen to occur at a slower rate than heating. This is expected to occur for components used in a desktop computer. It should be pointed out that the field-use thermal cycling tends to be benign compared to ATC where the maximum temperatures can go to 125°C and the minimum temperatures can go to -55°C. The maximum temperature of 90°C seen during field-use thermal cycling is far less than the melting temperature of 217°C for Sn-Ag-Cu alloy.

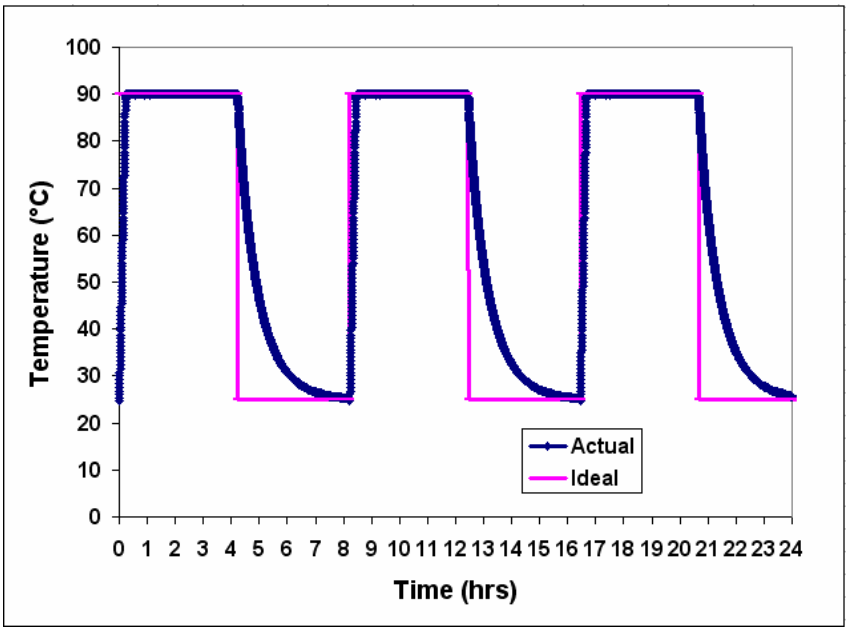

Figure 4.10. Monitored temperature profile during field-use thermal cycling

4.4. Phase Coarsening During Extended Thermal Excursion

Eight packages of each type were subjected to extended duration field-use thermal cycling lasting 90 days. Two samples of each package type as shown in Table 4.1 were taken out at regular intervals from the thermal chamber used for field-use thermal cycling. The packages were taken out at three intervals between 0 days to 90 days. The daisy

chain resistance was monitored during each interval. Due to benign nature of the thermal cycling and because thermal cycling was done only for 90 days, no electrical failures were observed. The packages were then molded and cross-sectioned along the centerline to reveal the solder bumps for microstructure evaluation. No solder joint failures due to crack propagation were observed in the cross-sectioned solder joints. A 50µm x 60µm rectangular area near the package side interface was chosen for all microstructural evolution study. The phase coarsening for all the three package types before subjecting the packages to field-use thermal cycling and after 90 days of field-use thermal cycling is shown in Figure 4.11, Figure 4.12 and Figure 4.13.

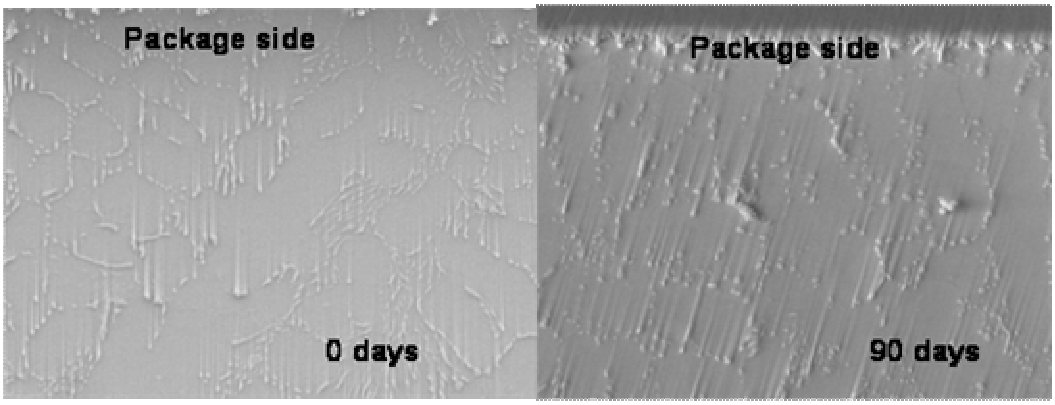

Figure 4.11. Phase coarsening during 90 days of field-use for PBGA 676 package with SAC405

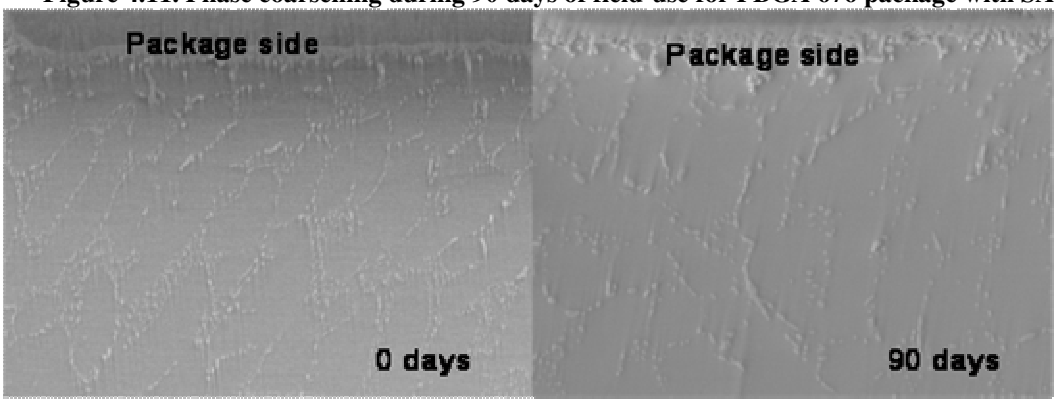

Figure 4.12. Phase coarsening during 90 days of field-use for PBGA 676 package with SAC305

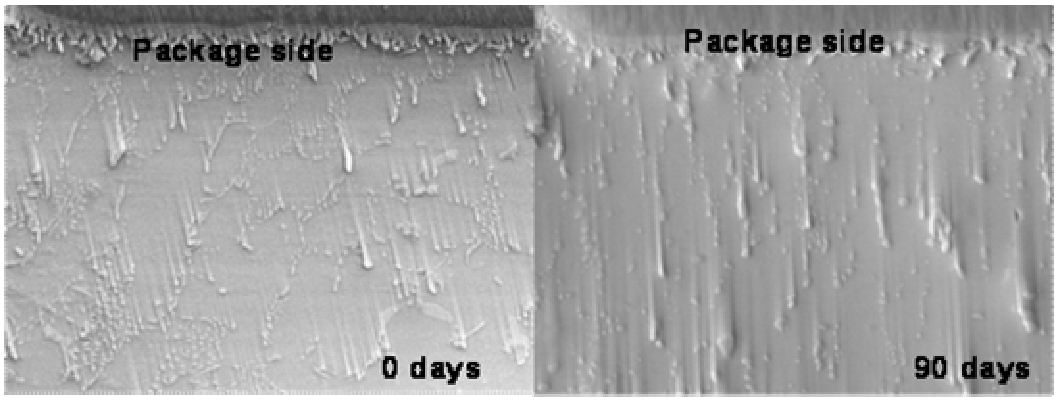

Figure 4.13. Phase coarsening during 90 days of field-use for PBGA 160 package with SAC405

The evolution of the phase growth parameter in the solder joints for all the three package configurations is shown in the Figure 4.14 through Figure 4.16. The variation for all the three cases was found to be close to linear.

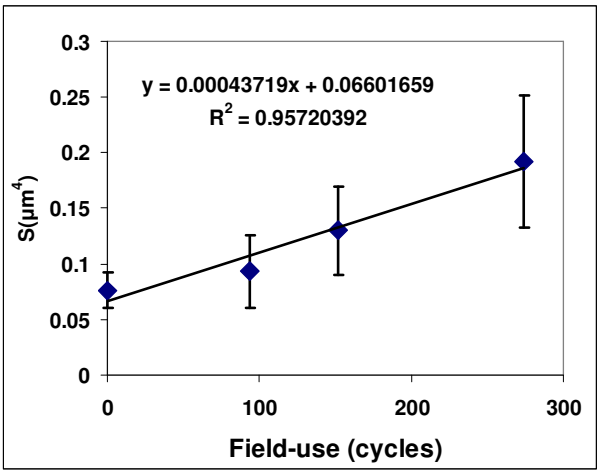

Figure 4.14. Evolution of the phase growth parameter during field-use for PBGA676 package with SAC405 alloy

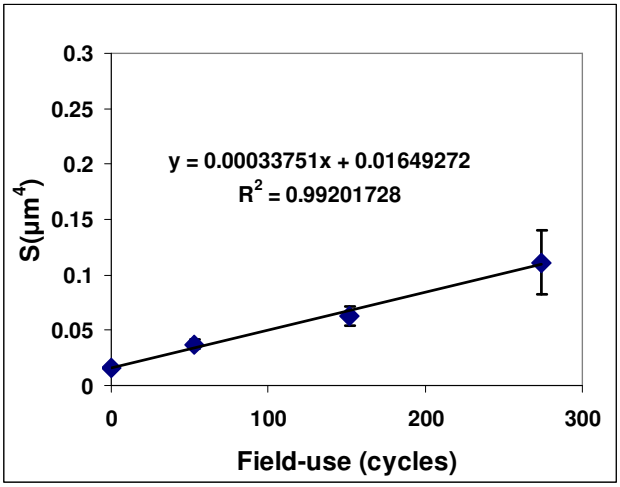

Figure 4.15. Evolution of the phase growth parameter during field-use for PBGA676 package with SAC305 alloy

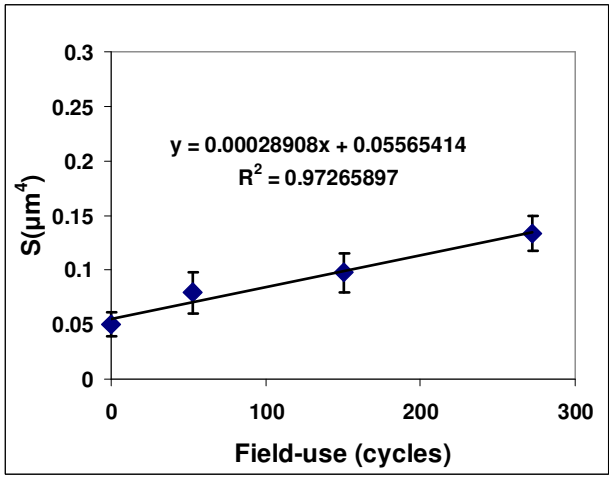

Figure 4.16. Evolution of the phase growth parameter during field-use for PBGA160 package with SAC405 alloy

The change in the phase growth parameter per cycle for all the three package configurations is shown in Table 4.3.

Table 4.3. Change in the phase growth parameter in the solder joint per cycle during field-use thermal cycling

Package Type	ΔS/cycle (x10^{-4} μm^4)
PBGA676 – SAC405	4.37
PBGA676 – SAC305	3.38
PBGA160 – SAC405	2.89

The SAC405 alloy has a higher amount of Ag to supply to the growing Ag_3Sn phase. PBGA 676 package with SAC405 therefore coarsens at a higher rate when compared to the PBGA 676 package with SAC305 alloy. PBGA 676 with SAC405 also coarsens at a higher rate when compared to the PBGA 160 package with SAC405 alloy. This is because PBGA 676 package is a bigger package with larger solder volume and higher I/O connections. The larger package size leads to increased strains from CTE mismatch between the package and the board thereby leading to increased rate of coarsening. The larger package size also implies increased heat capacity and therefore the package would cool at a slower rate from the high temperature. Slower rate of cooling from high temperature during thermal cycling means that the package on an average is maintained at a higher temperature. This allows the Ag_3Sn particles to coarsen at a higher rate.

CHAPTER 5

MICROSTRUCTURE EVOLUTION AND DETERMINATION OF ACCELERATION FACTOR DURING THERMAL CYCLING

This chapter outlines the microstructure evolution study for lead-free PBGA packages during accelerated thermal cycling. The package types and the solder alloys used are similar to the ones used for the microstructure evolution study during benign field-use thermal cycling. The experimental procedure will be discussed first followed by the phase coarsening based microstructure evolution study for the different packages types. Using the microstructure evolution results from field-use thermal cycling and ATC acceleration factors will be determined for all the different package types. Summary of the evolution study will be provided towards the end.

5.1. Accelerated Thermal Cycling Experiments

The package types used for this study are similar to the ones mentioned in the previous chapter and are shown in Table 4.1. The packages were assembled using the same reflow process mentioned in the previous chapter. Over ten packages of each type were subjected to a representative military standard ATC. The packages were placed in a basket and the basket was moved between two thermal chambers maintained at -55°C and 125°C. The dwell time at each thermal chamber was 15 minutes. Thermocouples were placed on the package to monitor the temperature profile as experienced by the package. The monitored temperature profile is shown in Figure 5.1. It can be seen from

the plot that the actual measured temperature lags behind the set temperature of the thermal chamber due to thermal masses of the basket and the packages. Two samples of each type were taken out from the thermal chamber at various intervals of time ranging from 0 ATC to about 4000 ATC. These samples were then molded and cross-sectioned along the center line of the package for microstructure evaluation.

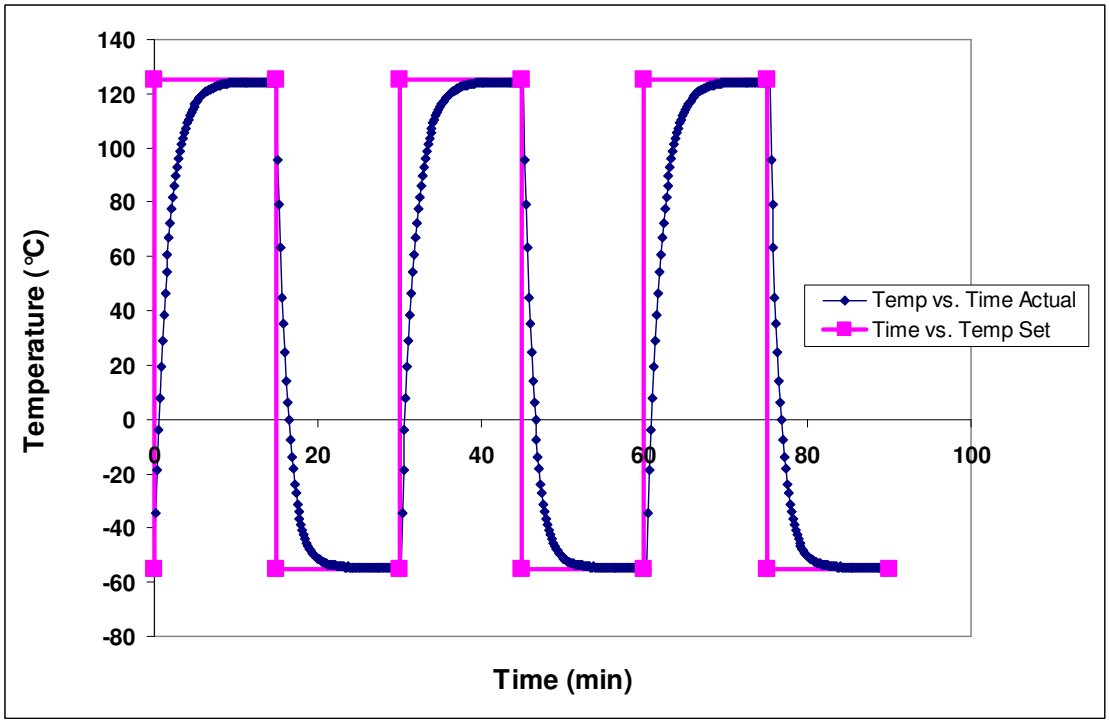

Figure 5.1. Monitored temperature profile for ATC

5.2. Microstructure Evolution During ATC

A 50μm x 60μm rectangular area at the solder joint neck region at package side interface as shown in Figure 5.2 was chosen for all microstructural evolution study. The size of the area is same as the size of the area chosen for microstructural quantification during field-use thermal cycling. Image analysis and microstructural quantification was performed on all the three outermost solder joints along the centerline of the package at

both the solder neck corner regions as circled and shown in Figure 4.7. Totally twelve images were analyzed per package type to obtain the average phase size.

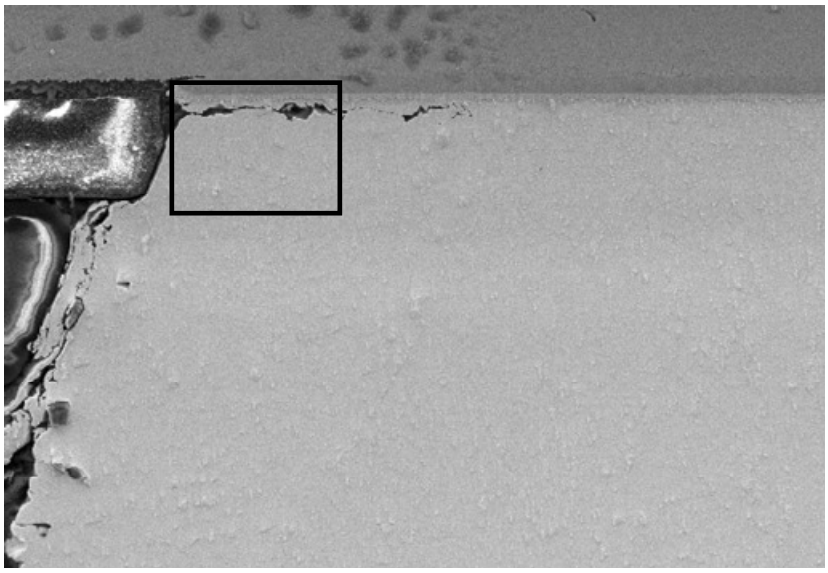

Figure 5.2. SEM image of the cracked solder joint in the PBGA 676 sample

During ATC, the Ag_3Sn phase coarsens significantly in the indicated region. The coarsening for PBGA 676 package with SAC405 alloy is shown in Figure 5.3. A clear dendrite structure can be seen at 0 ATC. At 571 thermal cycles, the phase coarsens and the dendrite structure can still be seen faintly. At 1276 and 2506 thermal cycles, the dendrite structure has completely vanished. The coarsening effect is also seen to be not homogeneous. More coarsening is seen near the package side interface (top part of the figure) of the solder alloy due to increased stresses in this region. Similar trends can be seen for PBGA 676 package with SAC305 alloy and for PBGA 160 package with SAC405 alloy as shown in Figure 5.4 and Figure 5.5 respectively. Both these packages can be seen to not coarsen as much as PBGA 676 package with SAC 405 alloy.

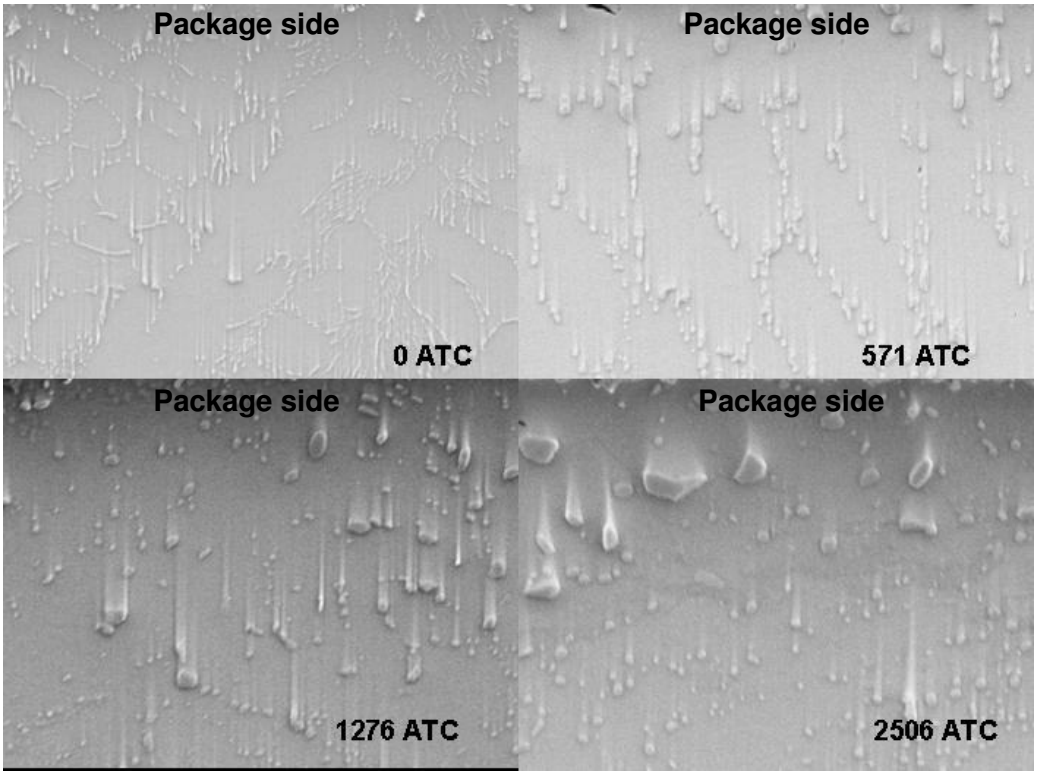

Figure 5.3. Microstructural coarsening of Ag_3Sn in PBGA 676 package with SAC 405 alloy

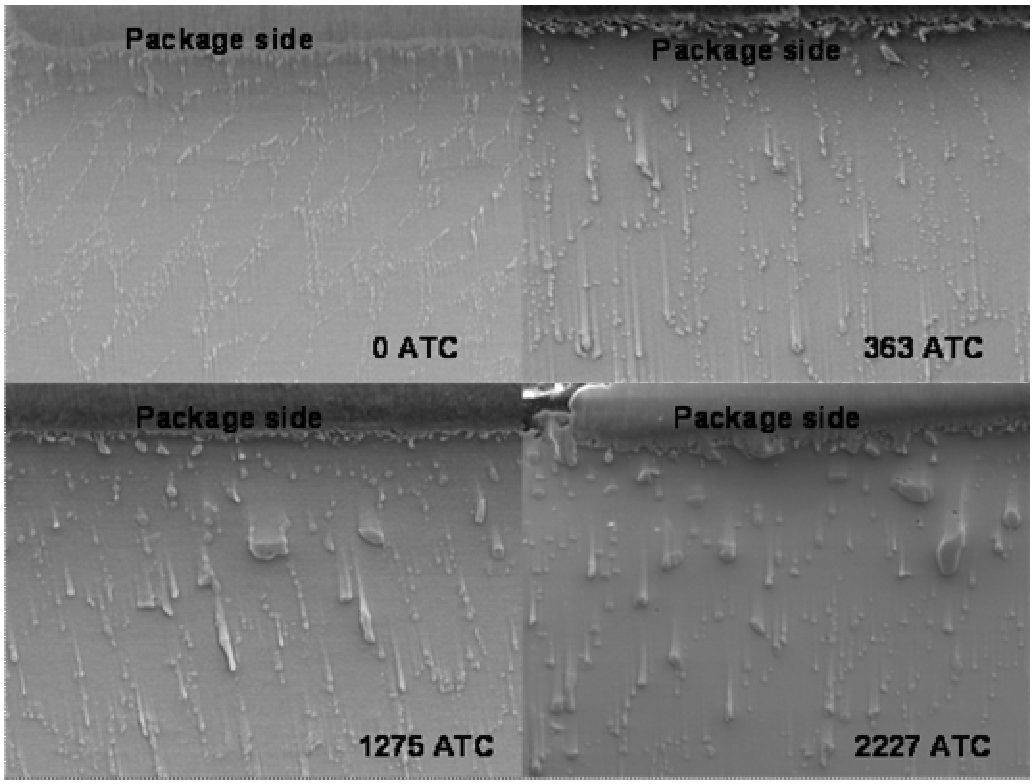

Figure 5.4. Microstructural coarsening of Ag_3Sn in PBGA 676 package with SAC 305 alloy

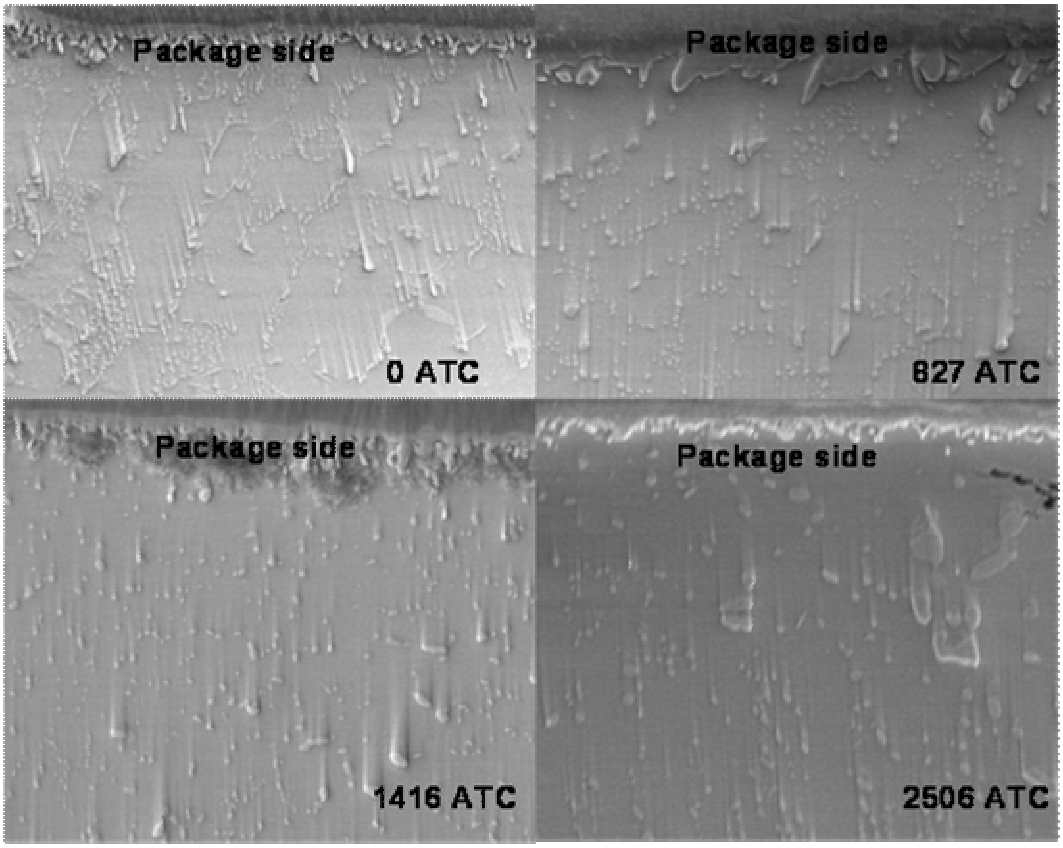

Figure 5.5. Microstructural coarsening of Ag_3Sn in PBGA 160 package with SAC 405 alloy

The evolution of the phase growth parameter for the three different package types is shown in Figure 5.6 through Figure 5.8. The phase growth parameter increase monotonically thereby it an appropriate metric for characterizing microstructure evolution. The rate of increase is seen to decrease with thermal cycling. This could either be due to limited amount of Ag available in the solder alloy or due to failure of the solder joint from crack initiation and propagation. Both linear and quadratic equations were used to fit to the phase coarsening data obtained from ATC. From the R^2 value we can conclude that the quadratic equation fits very well to the experimental data than the linear equation. Looking at the shape of the fitted curve, it is evident that the variation of the

phase growth parameter is almost linear for the first 2000 ATCs. After that, a gradual decrease in the rate of increase in phase growth parameter can be seen. PBGA676 package with SAC305 solder has less Ag to supply for the growing Ag_3Sn phase. This results in slower rate of increase in the phase growth parameter during thermal cycling. Decreased availability of Ag also implies the rate of increase in the phase growth parameter decreases more rapidly for the package with the SAC 305 alloy as can be seen in Figure 5.7.

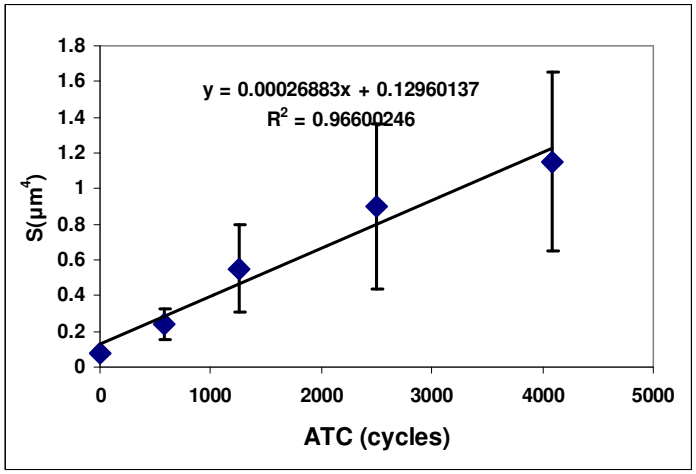

a

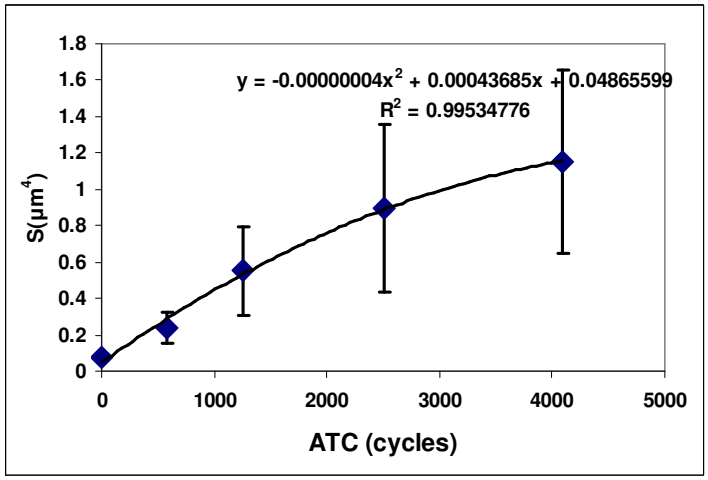

b

Figure 5.6. Evolution of the phase growth parameter during ATC for PBGA 676 package with SAC 405 alloy a) Linear fit b) Quadratic fit

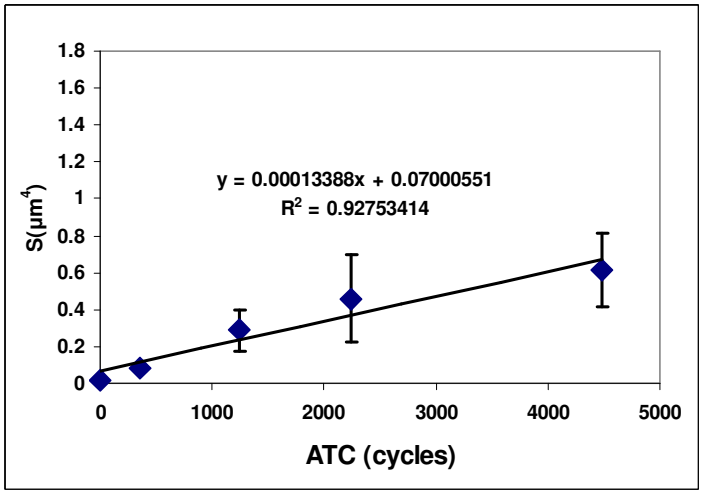

a

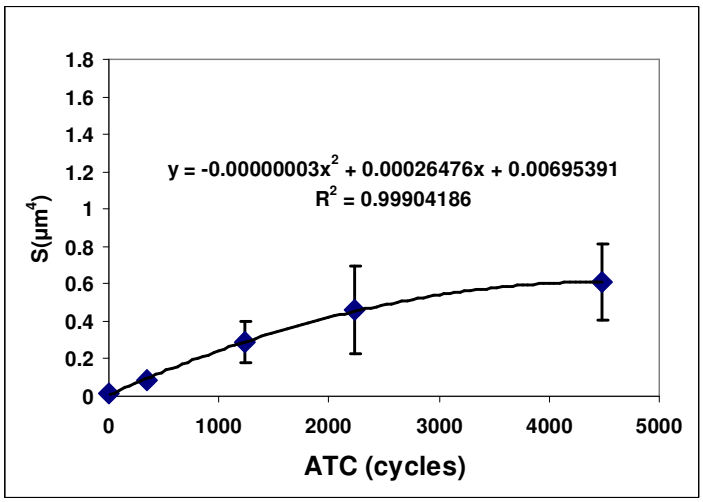

b

Figure 5.7. Evolution of the phase growth parameter during ATC for PBGA 676 package with SAC 305 alloy a) Linear fit b) Quadratic fit

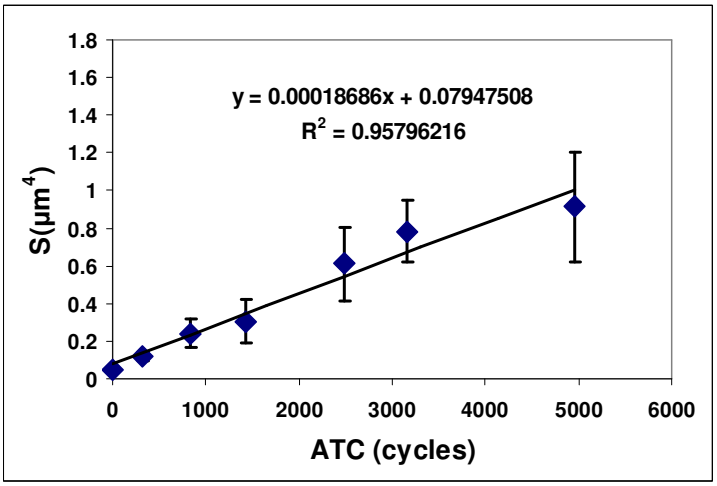

a

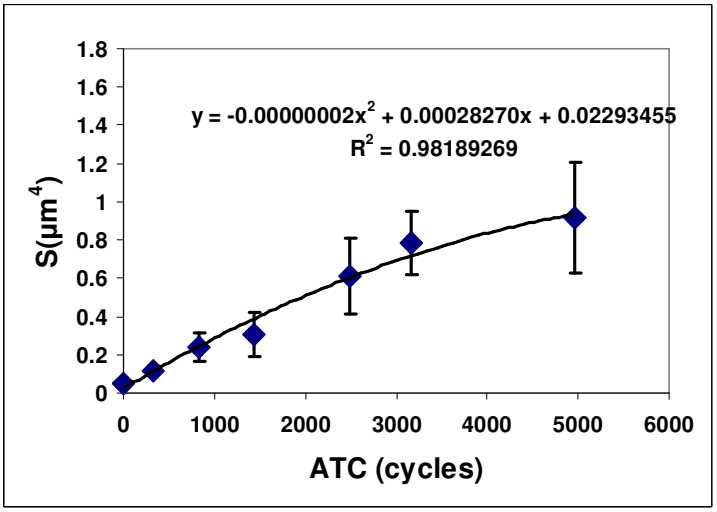

b

Figure 5.8. Evolution of the phase growth parameter during ATC for PBGA 160 package with SAC 405 alloy a) Linear fit b) Quadratic fit

The slope of the curve can be used as a metric to quantify the change in the phase growth parameter in the solder joint per cycle. The change in the phase growth parameter per ATC as estimated from both linear and quadratic equation fits for all three package types is shown in Table 5.1. For the quadratic fit, the damage was evaluated at the beginning of the thermal cycling. The linear evolution equation greatly underestimates

the change in the phase growth parameter done per ATC as shown in the last column of Table 5.1. The error in the estimation by using a linear fit is more for the PBGA 676 with SAC305 alloy because the rate of increase in the phase growth parameter starts to decrease at an earlier stage compared to the other two package configurations. PBGA 676 package with SAC405 coarsens at a higher rate when compared to the PBGA 676 package with SAC305 alloy due to its higher Ag content. PBGA 676 with SAC405 also coarsens at a higher rate when compared to the PBGA 160 package with SAC405 alloy due to larger package size giving rise to increased strains from CTE mismatch between the package and the board.

Table 5.1. Change in the phase growth parameter in the solder joint per cycle during ATC

Package Type	ΔS/cycle from linear fit ($x10^{-4}$ μm^4)	ΔS/cycle from quadratic fit ($x10^{-4}$ μm^4)	% difference
PBGA676 – SAC405	2.69	4.37	38.4%
PBGA676 – SAC305	1.34	2.65	49.4%
PBGA160 – SAC405	1.87	2.83	33.9%

The deviation in the phase growth parameter can be seen to increase with ATC for all three package configurations. As was mentioned before, tin is an anisotropic material with CTE varying between 15ppm/K to 30ppm/K depending on its orientation. The tin grain within the solder joint which is aligned favorably with respect to the copper pad, which has a CTE of 16ppm/K, will not coarsen as much when compared to a tin grain within the solder joint which is not aligned favorably. Since the orientation of the tin grain near the copper pad is random, the coarsening rates of different solder joints will also be random and different. With thermal cycling, this different rate of coarsening becomes very substantial and reflects as a large deviation in the measured phase growth parameter. The deviation is very substantial for the PBGA676 package with SAC405 alloy. SAC305 alloy which has a reduced Ag content coarsens at a slower rate as

explained before. The difference in the rate of coarsening of the randomly oriented grains is therefore not as substantial as it is for the package with SAC405 alloy. This reflects in lesser deviation in the phase growth parameter for SAC305 alloy with thermal cycling. The deviation in the measured phase growth parameter is less for the PBGA160 package. The smaller package size leads to lesser strains from CTE mismatch between the package and the substrate. This leads to decrease the phase growth rate and the deviation in the phase growth parameter for the PBGA160 package.

5.3. Acceleration Factor Estimation

Acceleration factor is an empirically determined number used commonly to qualify a package under field-use conditions. Field use conditions are typically very complicated and there is no simple equation that can be used to determine the acceleration factor easily. In addition to change in phase growth parameter per cycle (ΔS), acceleration factor can be dependent on temperature range (ΔT), loading frequency ($freq$), maximum temperature (T_{max}) and time of dwell (t_{dwell}) as shown in Equation 5.1 [54].

$$AF = \frac{N^{Field}}{N^{ATC}} = F(\Delta S, \Delta T, freq, T_{Max}, t_{dewell}) \qquad 5.1$$

For the present study, a single factor ΔS has been used for acceleration factor determination. The change in phase growth parameter per cycle during ATC and field-use thermal cycling can be used to determine the acceleration factor for each package type during ATC. The number of cycles for failure (N_i) is related to the change in phase growth parameter per cycle by a relation given in Equation 5.2 [36].

$$N_i = C_1(\Delta S)^{C_2} \qquad 5.2$$

where, C_1 and C_2 are constants. The acceleration factor was determined by taking a ratio of the number of cycles required for failure during field-use thermal cycling ($N_i^{Field\text{-}use}$) and the number of cycles required for failure during ATC (N_i^{ATC}). The relation is given in Equation 5.3.

$$Acceleration\ \ factor = \frac{N_i^{field-use}}{N_i^{ATC}} = \left(\frac{\Delta S_{field-use}}{\Delta S_{ATC}} \right)^{C_2} \qquad 5.3$$

where, ΔS_{ATC} represents the change in phase growth parameter per ATC, $\Delta S_{Field\text{-}use}$ represents the change in phase growth parameter per field-use thermal cycle and C_2 has a known constant value of -1.96 [36].

For samples subjected to ATC, ΔS_{ATC} from the initial slope of the quadratic curve, at time t = 0, as shown in Table 5.1 was used for acceleration factor calculation. The acceleration factor determined from Equation 5.3 can be used to estimate an equivalent number of accelerated thermal cycles for samples subjected to 90 days of field-use thermal cycling. The results are tabulated in Table 5.2. For both the packages with SAC405 alloy, the change in the phase growth parameter per cycle is about the same for ATC and field-use thermal cycling. As was shown in Figure 4.9, among these two packages, the solder alloy in the PBGA160 package had a slightly lower initial phase size. This led to a slight increase in initial change of phase growth parameter per field-use thermal cycle for this package, in accordance with Equation 2.4. The acceleration factor for PBGA160 package is therefore slightly less than the acceleration factor for PBGA676 package. For both these packages with SAC405 alloy, 270 cycles of field-use thermal cycling is equivalent to about same number of accelerated thermal cycles. This implies that one 8 hour field-use thermal cycling with a temperature difference of 65°C roughly

does the same damage to the solder joint as one 30 minutes ATC with a temperature difference of 180°C. The PBGA676 package with SAC305 alloy however had a significantly lower initial phase size as shown in Figure 4.9. In accordance with Equation 2.4, shown before, this results in slightly higher rate of initial coarsening rate during field-use than expected. As a consequence, the acceleration factor for this package was significantly less than the acceleration factor for the other two package types.

Table 5.2. Acceleration factor and equivalent ATCs estimation

Package type	ΔS_{ATC} /cycle ($x10^{-4}\mu m^4$)	$\Delta S_{Field-use}$ /cycle ($x10^{-4}\mu m^4$)	Acceleration Factor	Equivalent ATCs
PBGA676 – SAC405	4.37	4.37	1.00	270
PBGA676 – SAC305	2.65	3.38	0.62	438
PBGA160 – SAC405	2.83	2.89	0.96	283

5.4. Summary of Microstructure Evolution Study

An Ag_3Sn phase coarsening based microstructural evolution study was performed on two different PBGA packages using two different lead-free solder alloys. The packages were subjected to two different thermal cycling conditions – an accelerated thermal cycling between -55°C and 125°C and a benign field-use thermal cycling between room temperature and 90°C. A phase growth parameter was used to quantify microstructural evolution under both these thermal cycling conditions. The following conclusions can be drawn from the obtained results.

- The initial size of the Ag_3Sn precipitates was found to depend both on the solder volume and the Ag content in the solder alloy. An increase in solder volume and Ag content led to an increase in the initial size of the Ag_3Sn phase.
- The rate of increase in phase growth parameter increased with size of the package and with Ag content in the solder alloy. The rate of increase decreased with time for all packages when subjected to ATC. The decrease occurred earlier for solder

joints with lower Ag content. However, when subjected to field-use conditions, the rate of increase in was found to be fairly constant.

- With an increase in the number of cycles, increased deviation in the measured phase growth parameter was seen. The increased deviation can be attributed to random orientation of few anisotropic β-Sn grains in the solder joint. Reduced Ag content in the solder joint and a smaller sized package decreased this deviation.
- The change in the phase growth parameter was found to be of the same order for both ATC and field-use thermal cycling. The acceleration factor was found to be slightly dependent on the solder alloy used in the package. This difference can be attributed to difference in the initial Ag_3Sn phase sizes due to varying Ag content in the alloy.

CHAPTER 6

VIRTUAL RELIABILITY ASSESSMENT OF PBGA PACKAGES

The finite element analysis procedure for the PBGA packages will be outlined in this chapter. The geometrical construction, finite element model and material models used will be described first. This will be followed by the loading conditions used and results from the FEA procedure. The results from the FEA will be combined with experimental results, to be discussed in the next chapter, to develop a fatigue life prediction model that can be used to predict the package life of PBGA packages.

6.1. Geometrical Details of PBGA Packages

Three different PBGA packages from Amkor®, as shown in Table 6.1 were modeled for the analysis.

Table 6.1 Package configurations used for predictive model development

Package Type	I/O count	Solder Alloy
PBGA	160	SAC405
PBGA	676	SAC405
PBGA	356	SAC405

All packages had solder joints with SAC405 alloy. The package construction was similar for all the three package types. The package consisted of a face-up silicon chip attached to a BT substrate from below using a die-attach material. I/O pads on the silicon chip were wire bonded on the top side of the BT substrate. The chip and substrate were encapsulated using a mold compound for protection from shock, vibrations and outside environment. The I/O pads on the bottom of the substrate were solder bumped. The

packages were assembled on a 1.5mm thick FR4 board. Schematics of the cross-section of the assembled packages along with its footprint on the board are shown in the Figure 6.1 through Figure 6.3.

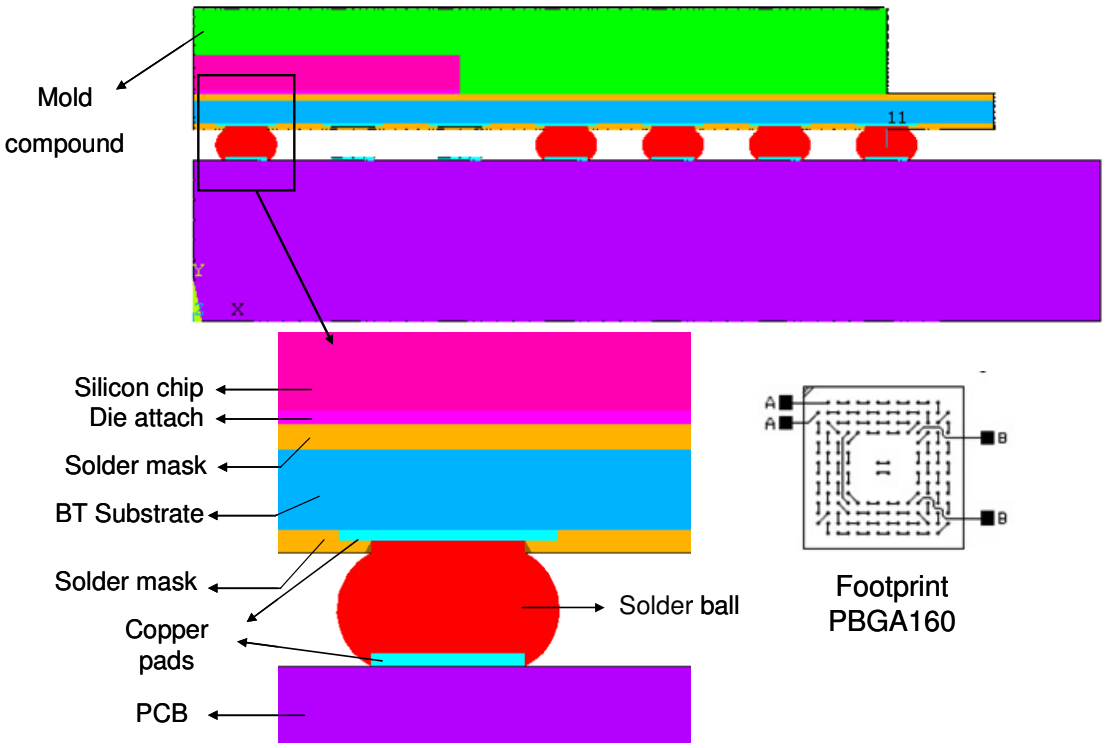

Figure 6.1. Cross-section along the centerline and footprint of the PBGA 160 package

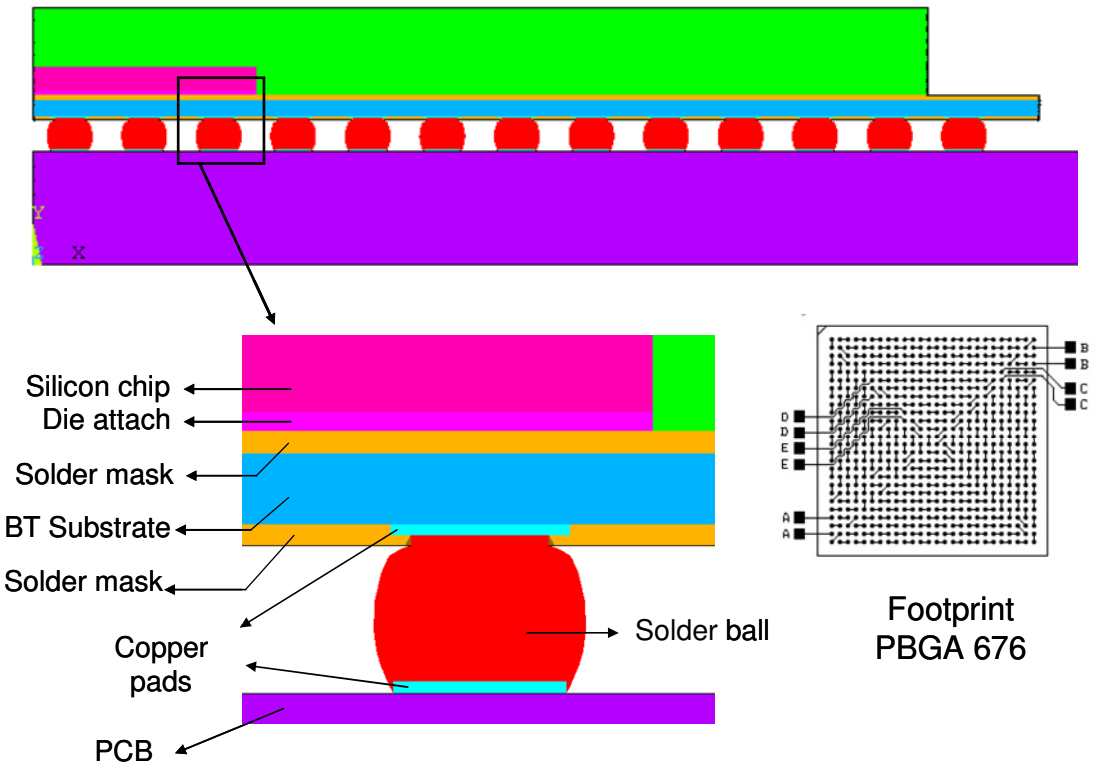

Figure 6.2. Cross-section along the centerline and footprint of the PBGA 676 package

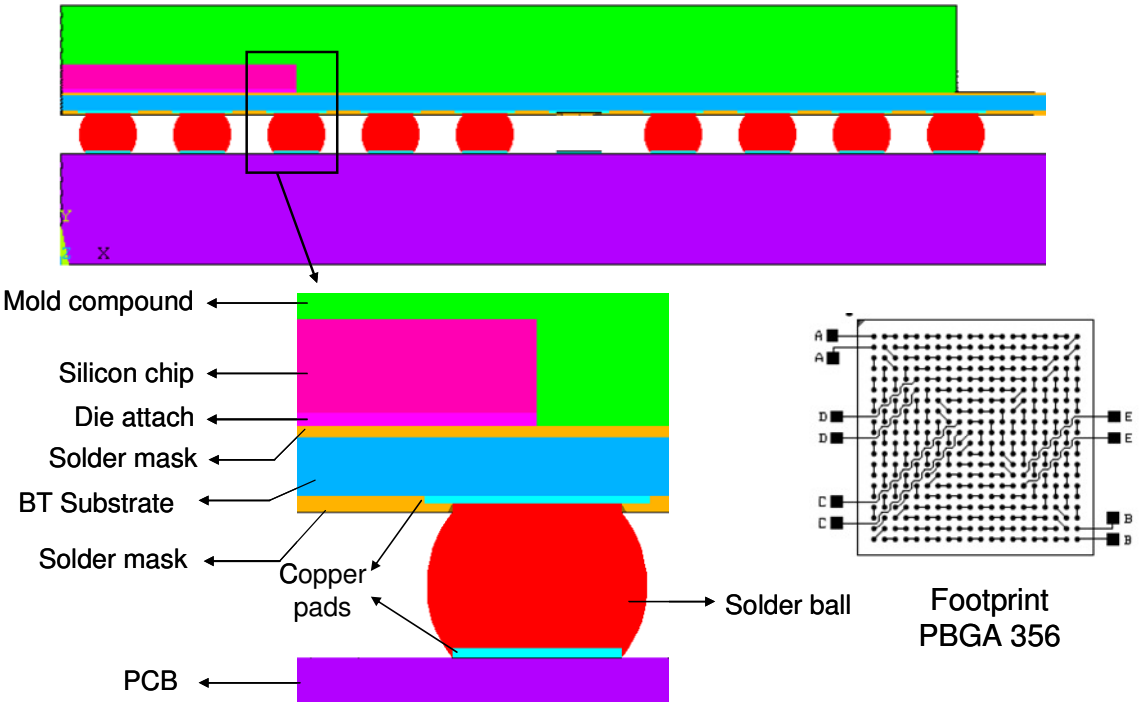

Figure 6.3. Cross-section along the centerline and footprint of the PBGA 356 package

The important geometrical dimensions of all the three package types are shown in Table 6.2. The dimensions were either obtained by the package vendor data sheets or by direct measurement using optical microscope.

Table 6.2. Geometrical dimensions of the PBGA packages

Dimension	PBGA160	PBGA676	PBGA356
Solder pitch	1 mm	1 mm	1.27 mm
Package substrate width	15 mm	27 mm	27 mm
Package substrate thickness	206 µm	206 µm	206 µm
Chip width	5 mm	6.3 mm	6.3 mm
Chip thickness	0.33 mm	0.33 mm	0.33 mm
Die attach width	5 mm	6.3 mm	6.3 mm
Die attach thickness	36 µm	54 µm	47 µm
Solder standoff height	0.30 mm	0.43 mm	0.52 mm
Solder width in the package side neck region	450 µm	450 µm	630 µm
Mold width	13 mm	24 mm	24 mm
Mold thickness	0.8 mm	1.17 mm	1.17 mm
Solder mask thickness – top of substrate	66 µm	68 µm	45 µm
Solder mask thickness – bottom of substrate	52 µm	64 µm	61 µm
Copper pad thickness	30 µm	30 µm	30 µm

6.2. 3D One Fourth Finite Element Model

3D models were created to model the PBGA packages. A full 3D model gives an accurate representation of the package geometry. If the package possesses symmetry, only part of the package needs to be modeled and the accuracy can still be retained. All the three packages used had one eighth symmetry. In a one eighth model, only half cross-section of the solder joints along the diagonal line is modeled. Symmetry boundary

conditions are applied on these half solder joints. Due to proximity of the solder joints along the diagonal to the applied boundary conditions, the simulation results for these solder joints could be erroneous. A one fourth model was therefore modeled as shown in Figure 6.4. The boundary conditions for the one fourth symmetry package involves constraining all the nodes on the x-y plane so as to have zero displacement in the z-direction and constraining all the nodes on the z-y plane so as to have zero displacement in the x-direction. In addition, a node at the origin is constrained so as to have zero displacement in all the three directions.

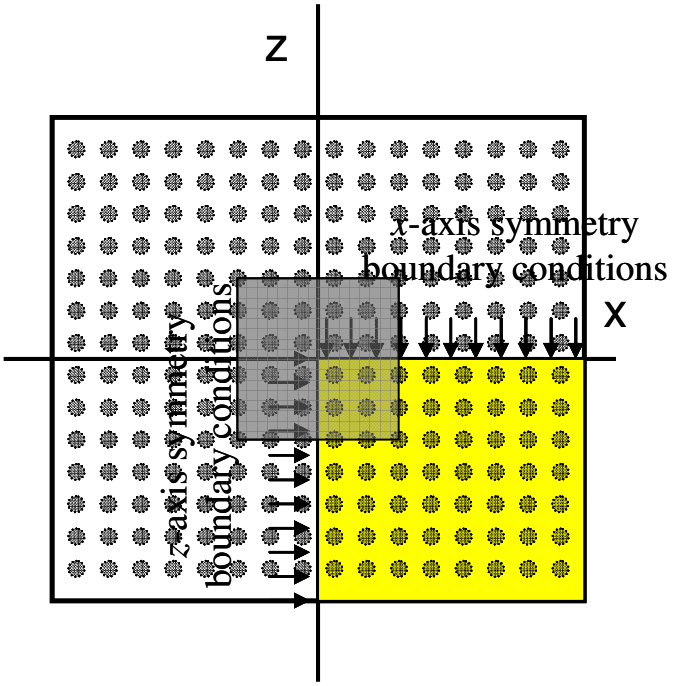

Figure 6.4. One fourth package symmetry shown from top view

A quarter package finite element model for the PBGA160 package is shown in Figure 6.5. The geometrical construction of other two packages was similar. ANSYS 11.0 was used for all the finite element analysis. The SOLID45 linear element was used for meshing all the materials in the package except for the solder joint. The VISCO107 linear

element, which allows using viscoplastic material property, was used to mesh the solder joint.

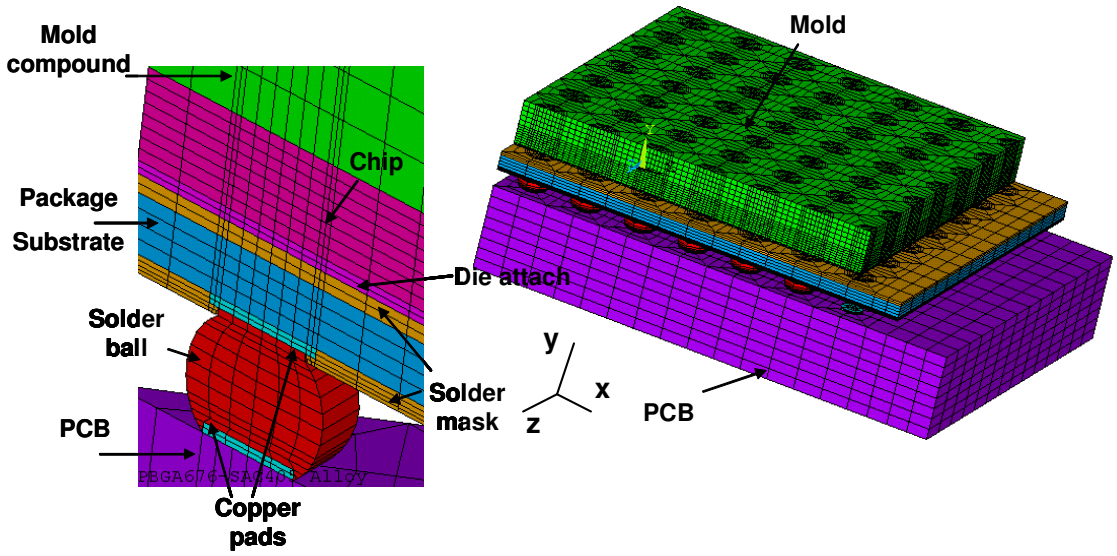

Figure 6.5. One fourth finite element model

6.2.2. Surface Evolver for Solder Joint Shape Evaluation

The shape and geometry of the solder ball can play an important role in solder joint life estimation. As the solder ball is axisymmetric, cross-sectioning the assembled PBGA package along the centerline is one way to find the shape of the solder ball. Inspection of the cross-sectioned package to ensure that the solder ball is cut exactly at the center can only to be done manually. The diameter and shape estimation are therefore prone to errors. The shape of the solder ball after reflow can be found easily using a Surface Evolver program developed at the University of Minnesota [55]. The program works by minimizing the surface energy of the solder joint given a set of geometrical constraints. Once the results from Surface Evolver are validated with experimental cross-sectioning, the Surface Evolver program can then later be used to determine the shape of

any solder joint with different set of geometrical constraints. The solder contour from Surface Evolver can easily be exported to ANSYS.

The energy of the surface is due to the surface tension and gravity. The surface of the solder joint is represented by a set of nodes, edges and facets. Geometrical constraints are then imposed on the surface. Geometrical constrains includes measured standoff height, copper pad diameters at the top and bottom of the solder joint and volume of the solder. During situations, where the standoff height is not available, the load on the solder ball due to the weight of the package can be used instead. After all the geometrical constraints are imposed, the shape of the solder is determined through an evolution process using mean curvature [56] as shown in Figure 6.6 until the surface energy of the solder joint is minimized.

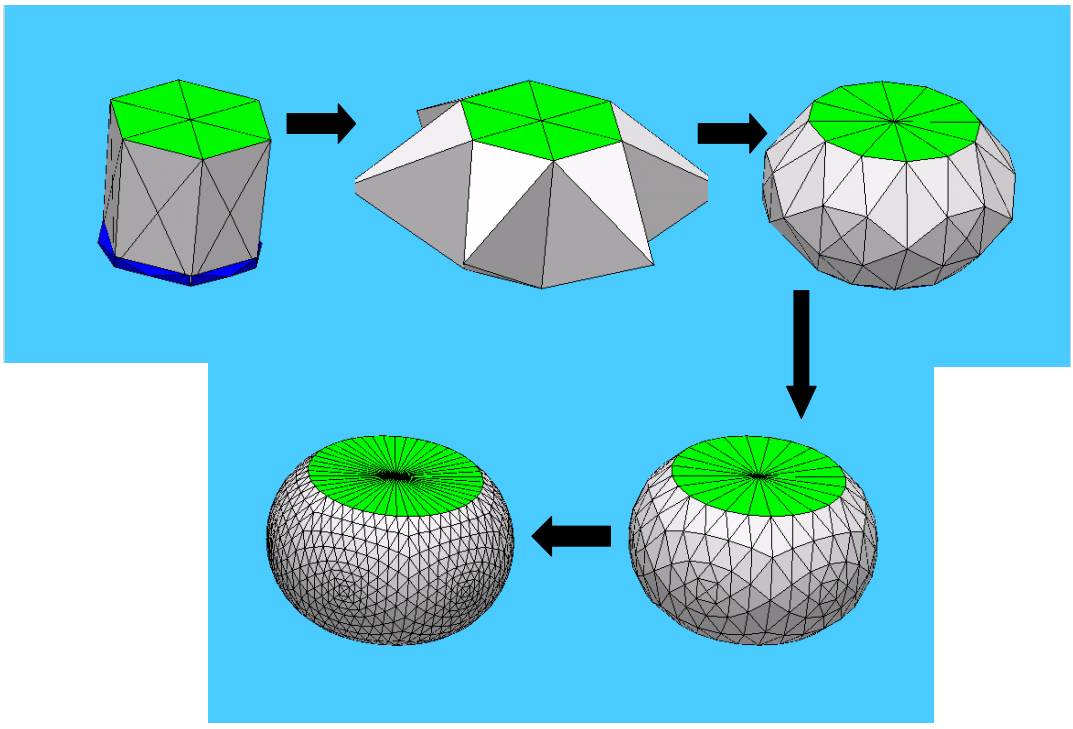

Figure 6.6. Evolution process of the solder ball geometry in Surface Evolver [57]

Validation of the shape as determined by Surface Evolver was performed by comparing the shape and the diameter of the solder ball at its centerline. A comparison between the simulated and cross-sectioned solder ball for all the three package types is shown in Figure 6.7 through Figure 6.9. The shape of the solder ball as predicted by the Surface Evolver matches very well with the shape of the solder ball as seen through experimental cross-sectioning for all the three package types.

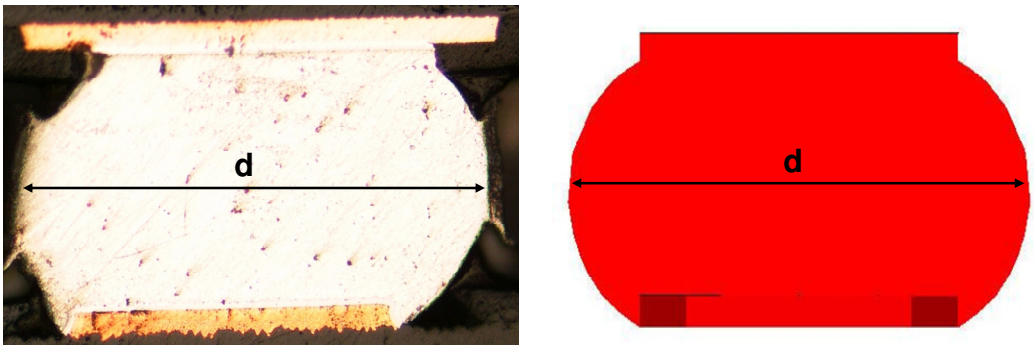

Figure 6.7. Shape comparison between cross-sectioning and Surface Evolver for PBGA 160

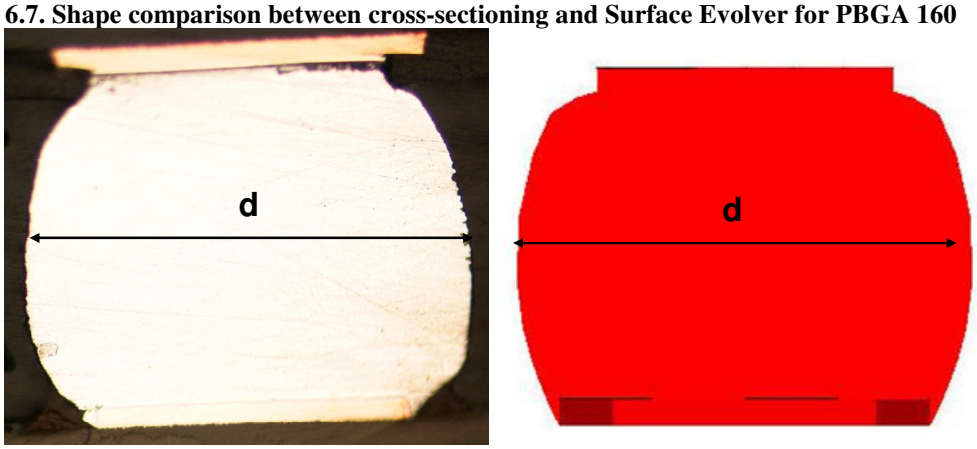

Figure 6.8. Shape comparison between cross-sectioning and Surface Evolver for PBGA 676

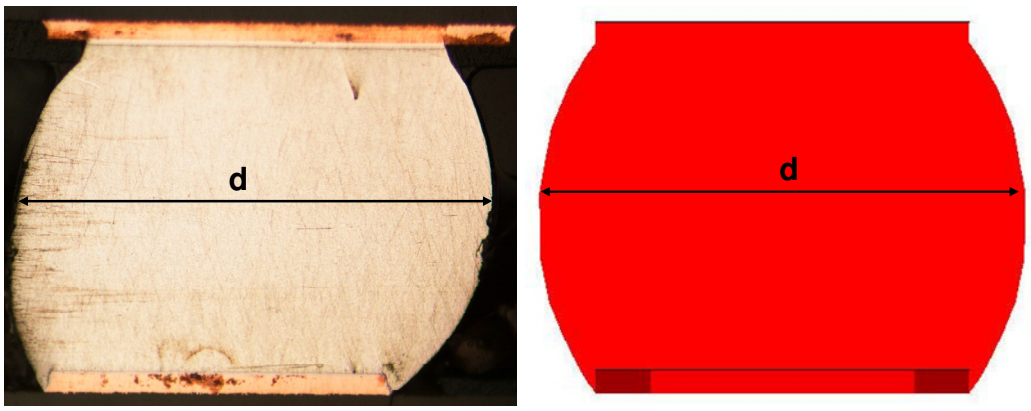

Figure 6.9. Shape comparison between cross-sectioning and Surface Evolver for PBGA 356

The mean diameter of the solder ball was determined by measuring the diameter for ten different cross-sectioned solder balls for a given package. The mean measured diameter was compared with the diameter as found from Surface Evolver. A comparison is shown in Table 6.3 and Figure 6.10. Good agreement can be seen between the simulated and experimental results. The error between them was under 5% as shown in Table 6.3.

Table 6.3. Comparison between the measured solder joint diameter and diameter from Surface Evolver

	Surface Evolver	Experiments - mean	% Error
PBGA 160	0.570	0.545	-4.498
PBGA 676	0.611	0.625	2.275
PBGA 356	0.782	0.762	-2.649

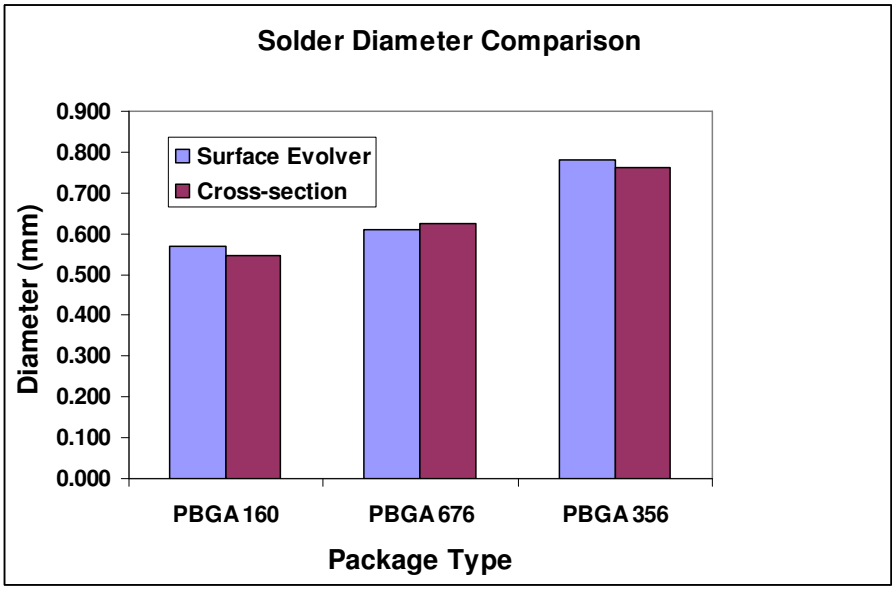

Figure 6.10. Comparison between the measured solder joint diameter and diameter from Surface Evolver

6.3. Material Models for the PBGA Package

The PBGA package is made up of different materials. A summary of the materials used for various parts of the PBGA package along with the material modeling method used is shown in Table 6.4.

Table 6.4. Material property details for the PBGA package

Name of part	Material	Material property	Temperature dependency
Copper pad	Copper	Elastic, Multilinear kinematic hardening	No
PCB	FR4	Elastic, orthotropic	No
Solder joint	SAC405	Elastic , viscoplastic	Yes
Package Substrate	BT (CCL-HL832)	Elastic, orthotropic	No
Chip	Silicon	Elastic	No
Mold	Nitto GE 100LFCS	Elastic	Yes
Solder Mask	Taiyo PSR 4000 – AUS303	Elastic	Yes
Die attach	Ablebond 2300	Elastic	Yes

All organic materials used in the package were modeled as linear elastic and temperature dependency was taken into consideration whenever the glass transition

temperature (T_g) was within the thermal cycling temperature range of -55°C to 125°C. The PCB and the package substrate material are fiber reinforced epoxies which makes the properties differ in out of plane direction. Orthotropic properties are therefore used for these two materials. The material properties were obtained from the vendor data sheets. The material property of an organic material is known to vary drastically around its glass transition temperature. The vendor data sheets provide only the material properties below and above T_g. The range within which the properties vary around the T_g is generally not provided. Modeling the material property with a step change in modulus or CTE at T_g could cause convergence issues in a FEA. Variation of modulus for a typical mold compound as determined by a Dynamic Mechanical Analyzer (DMA) is shown in Figure 6.11. It can be seen from the plot that the variation of modulus occur drastically within a ±20°C range centered at the T_g. For modeling purposes, it has therefore been assumed that the material properties vary within a ±20°C range centered at the T_g.

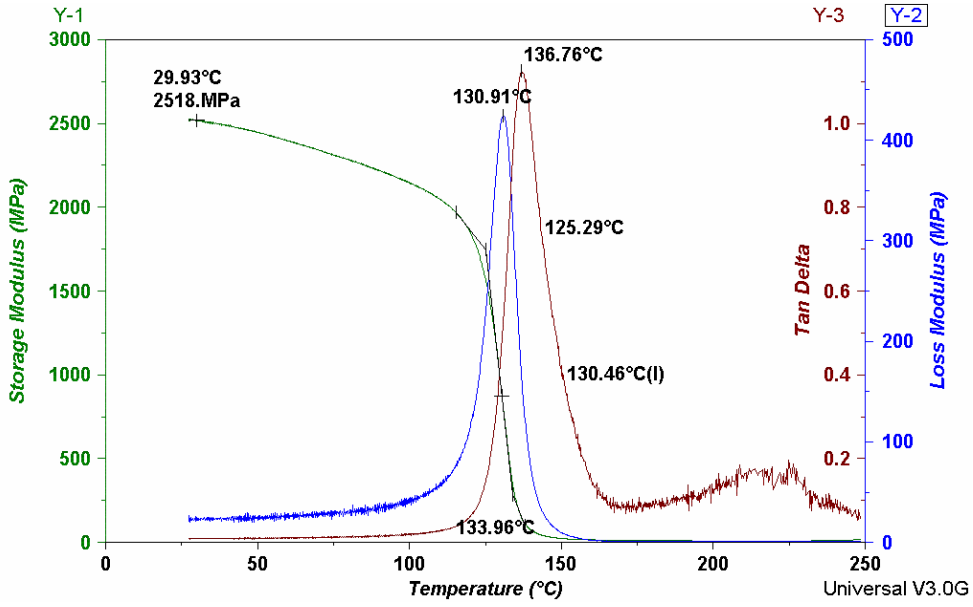

Figure 6.11. Typical DMA plot for a mold compound used in an electronic package

6.3.1. Package Substrate

Copper clad BT laminates were used as a substrate material in the PBGA package. The laminate material was CCL-HL832 [58]. The material had a T_g of 210°C as measured from the DMA and had a T_g of 180°C as measured from thermo mechanical analyzer (TMA). The material properties were obtained from vendor data sheets and are shown in Table 6.5. A vendor supplied Poisson's ratio was not available for the substrate. The Poisson's ratio for most materials varies between 0.25 and 0.35 [59]. Therefore, a value of 0.3 was assumed.

Table 6.5. Material properties for the package substrate

CCL-HL832	25°C
Modulus (GPa)	28.5
CTE-in plane	15
CTE-out of plane	55
Poisson's ratio	0.30

6.3.2. Mold Compound

The mold compound used was GE-100LFCS [58]. The material had a T_g of 145°C. This temperature is only slightly over the maximum temperature seen during thermal cycling. Temperature dependency was therefore taken into consideration. The CTE below and above T_g was 9 ppm/°C and 34 ppm/°C. The modulus values are provided at 25°C and 260°C and are respectively equal to 25GPa and 0.24GPa. The Poisson's ratio was not provided in the data sheets and is known to vary between 0.25 and 0.35 for most materials [59]. A Poisson's ratio of 0.3 was therefore assumed. The material properties used for the simulation is shown in Table 6.6.

Table 6.6. Material properties for the mold compound

GE-100LFCS	-55°C	135°C	155°C	250°C
Modulus (GPa)	25	25	0.24	0.24
CTE (ppm/°C)	9	9	34	34
Poisson's ratio	0.3			

6.3.3. PCB Material

The material used for the PCB was a high T_g FR406 [60] from Practical Components. The material had a T_g of 170°C. The vendor supplied material properties used for the finite element modeling is shown in Table 6.7.

Table 6.7. Material properties for the PCB material

FR406	
Modulus (GPa)	22.4
CTE-in plane	13
CTE-out of plane	65
Poisson's ratio	0.15

6.3.4. Die Attach Compound

The die attach compound used was Ablebond 2300 [58]. The material had a T_g of 0°C. The CTE below and above T_g was 60 ppm/°C and 129 ppm/°C. The modulus values were provided at 25°C and 250°C and were respectively equal to 1.8 GPa and 0.24 GPa. Since these two temperatures are above the T_g, the modulus variation between these two temperatures was assumed to vary linearly. The modulus value below T_g was not provided in the data sheet. The modulus below T_g was assumed to be the same as the modulus above T_g. The Poisson's ratio was not provided in the data sheet and was assumed to be 0.3 based on typical ranges of Poisson's ratio [59]. The material properties used for the simulation is shown in Table 6.8.

Table 6.8. Material properties for the die attach compound

Ablebond 2300	**-20°C**	**20°C**	**25°C**	**250°C**
Modulus (GPa)	1.8	1.8	1.8	0.24
CTE (ppm/°C)	60	129	129	129
Poisson's ratio	0.3			

6.3.5. Solder Mask

The solder mask material used was PSR4000 – AUS303 from Taiyo [61]. The material had a T_g of 101°C. The CTE before and after T_g was 60 ppm/°C and 130 ppm/°C respectively. The modulus value was provided only for temperatures before T_g. The same modulus has been assumed after T_g. The material properties for the solder mask are summarized in Table 6.9.

Table 6.9. Material properties for the solder mask compound

PSR4000 – AUS303	-55°C	81°C	121°C	225°C
Modulus (GPa)	2.4	2.4	2.4	2.4
CTE (ppm/°C)	60	60	130	130
Poisson's ratio	0.29			

6.3.6. Silicon chip

The silicon chip was modeled as a linear elastic material with temperature independent properties. The material properties were taken from Pang et al [62] and are shown in Table 6.10.

Table 6.10. Material properties for the silicon

Property	Value
Modulus (GPa)	131
CTE (ppm/°C)	2.8
Poisson's ratio	0.3

6.3.7. Copper Pads

Copper was modeled using temperature independent bilinear kinematic hardening model [63]. The electroplated copper in copper pads is known to exhibit kinematic hardening through Bauschinger effect [64]. The elastic and plastic material properties for the copper material is shown in Table 6.11 [65].

Table 6.11. Elastic and plastic material properties for copper

Material	Copper
Property	Value
E, MPa	$121x10^3$
ν	0.3
$\alpha_x = \alpha_y = \alpha_z$ (10^{-6}/°C)	17.3
Yield Strength (MPa)	172.38
Tangent Modulus (MPa)	1034.2

6.3.8. Solder Joint

The solder joint used for the analysis was SAC405 alloy. This alloy was modeled with linear elastic combined with viscoplastic material property. The modulus and CTE of the solder joint is temperature dependent as shown in Equations 6.1 and 6.2 . Agilent [66] has recommended constants for the elastic property of solder after combining the results from material testing performed at Sandia Labs [67, 68], Fraunhofer Institute and Dresden University [69]. The elastic property is valid within a wide temperature range from -55°C to 160°C. Agilent recommended solder has been used for the present research. The Poisson's ratio was 0.35.

$$E(GPa) = 49 - 0.07T(°C) \quad 6.1$$

$$\alpha(ppm/°C) = 21.301 + 0.017T(°C) \quad 6.2$$

Plasticity of the solder material was modeled using the viscoplastic material model formulation described by Anand [43]. Reinikainen [14] has fitted constants for this model for SAC405 alloy. The constants for his model are shown in Table 6.12 and have been used for modeling the solder joint.

Table 6.12. Anand's constants for the SAC405 solder

Constant	Constant Value
s_o, MPa	1.3 MPa
$Q/R, K$	9000 K
$A, \sec^{-1}$	500 $\sec^{-1}$
ξ	7.1
m	0.3
h_o, MPa	5900 MPa
$\hat{s}, MPa$	39.4 MPa
n	0.03
a	1.4

6.4. Thermomechanical Analysis

6.4.1. Stress Free Temperature

Before subjecting the package to thermal loading conditions as seen in ATC, the stress free temperatures of the various materials used in the package needs to be determined. Stress free temperature of a material corresponds to the temperature at which the material has either been cured or assembled. The silicon die was attached to the package substrate using a die attach and cured at 175°C. The silicon die was then encapsulated with a mold compound and cured at 175°C. The stress-free temperature of the whole package, excluding the copper pad, was therefore assumed to be 175°C. The package with the solder bumps was then reflowed in an oven to mount it on a PCB. During reflow, the solder melts and its stress goes to zero. The stresses in the copper pads on the package and the board side and the stresses in the PCB are also zero at the melting temperature of the solder. As the assembly cools down, stresses build up in the copper pads, solder joints and the PCB board. The stresses free temperature of these three materials was therefore assumed to be equal to the melting point of the solder, which is 217°C.

6.4.2. Accelerated Thermal Cycling Loading Condition

Once the stress free temperature of all the materials in the package is defined, the next step is to simulate the package with a thermal loading profile as seen during ATC. To accomplish this, the package was simulated with a loading profile which involves cooling down from the melting temperature to room temperature in one hour and then maintaining at room temperature for an hour. The package was then simulated to be subjected to a loading profile as seen during ATC. It should be pointed out that the simulated thermal profile should be similar to the thermal profile the package would experience in a thermal chamber. The thermal cycling equipment consisted of two chambers maintained at -55°C and 125°C. The packages were kept in a basket which moved between the high and low thermal chambers with 15 minutes dwell inside each chamber. The temperature on the package was monitored using a thermocouple. A comparison between the set temperature and the measured temperature on the package is shown in Figure 5.1. The package was simulated with a thermal cycling profile similar to the measured profile on the package during ATC. The simulated thermal profile is shown in Figure 6.12.

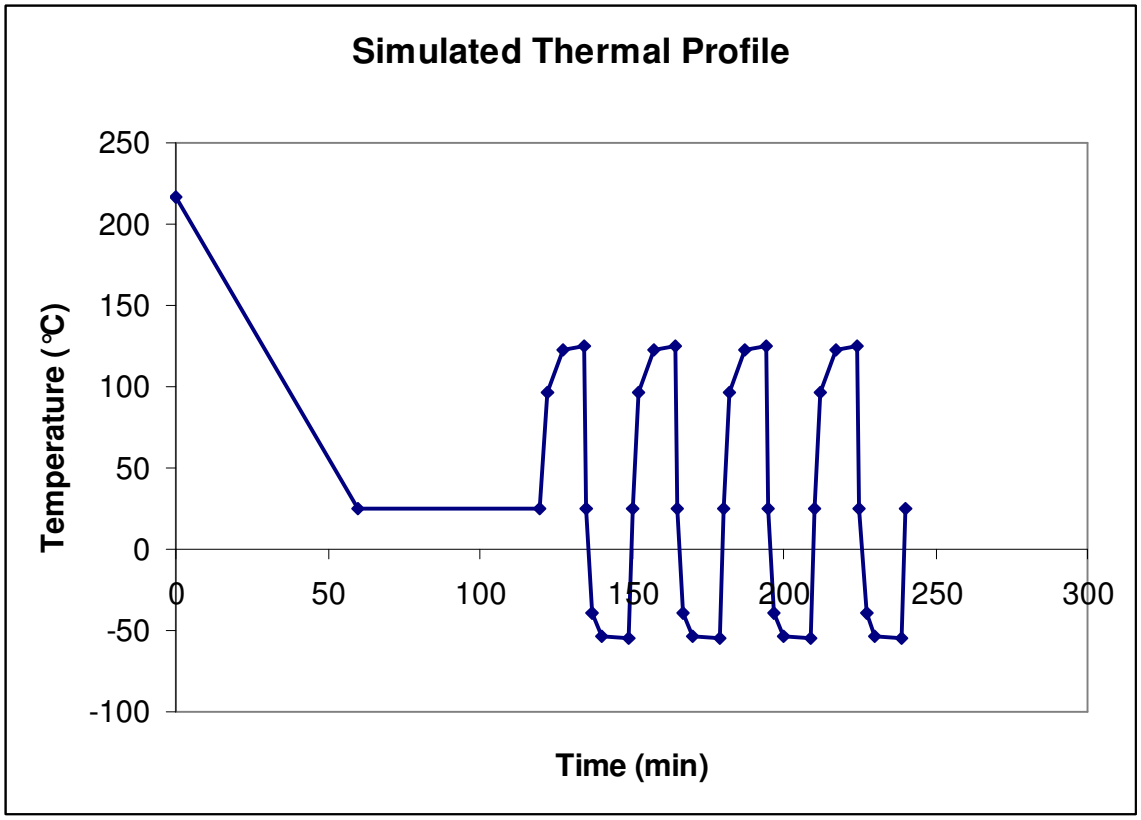

Figure 6.12. Simulated thermal profile during ATC

6.5. Results from Finite-Element Analysis

Developing a predictive model using results from finite element analysis involves extracting damage metrics for the relevant solder joints for one complete ATC profile. As was mentioned in Chapter 2, to prevent any mesh dependency from affecting the results, the damage metrics were volume averaged. Darveaux [18] has used a solid thin layer of elements near the package-solder interface for volume averaging purposes. Che et al [21] have shown that an annular thin layer of elements gives a better correlation with experimental results compared to a solid thin layer. An annular thin layer as shown in Figure 6.13 was therefore chosen for the study. Width of the annulus was 65μm and the thickness of the annular region was 60μm. The width and the thickness of the annular region were maintained at this constant value for all the three package types.

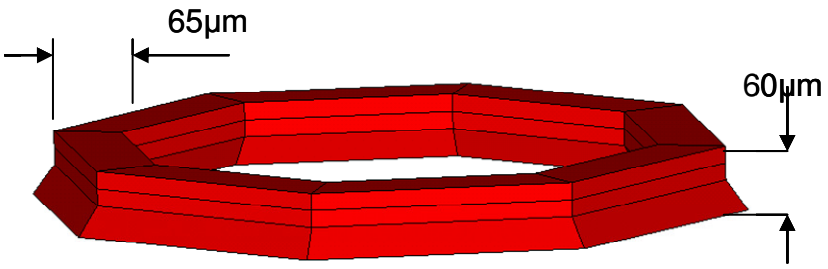

Figure 6.13. Annular layer of elements used for volume averaging

The damage metrics used for the predictive model development are, accumulated inelastic work (ΔW_{acc}), accumulated inelastic strain (ε_{acc}^{in}) and accumulated total strain (ε_{acc}^{tot}). The accumulated inelastic work for one thermal cycle for a given element is given by Equation 2.10. This inelastic work for an element can easily be extracted from ANSYS post processing using the NL, PLWK command. If *N* represents the number of load steps in one simulated ATC, the accumulated inelastic work in one cycle for a given element is given by Equation 6.3.

$$\Delta W_{acc} = W_N - W_1 \tag{6.3}$$

where, W_N is the inelastic work during the last load step of the cycle and W_1 is the inelastic work during the first load step of the cycle. The volume averaged inelastic work was found by using Equation 2.11. The accumulated inelastic strain for a given element is given by Equation 6.4,

$$\varepsilon_{acc}^{in} = \sum_{i=1}^{N-1} \frac{\sqrt{2}}{3} \left(\left(\Delta\varepsilon_{xx,i,i+1}^{in} - \Delta\varepsilon_{yy,i,i+1}^{in}\right)^2 + \left(\Delta\varepsilon_{yy,i,i+1}^{in} - \Delta\varepsilon_{zz,i,i+1}^{in}\right)^2 + \left(\Delta\varepsilon_{zz,i,i+1}^{in} - \Delta\varepsilon_{xx,i,i+1}^{in}\right)^2 + 6\left((\Delta\varepsilon_{xy,i,i+1}^{in})^2 + (\Delta\varepsilon_{yz,i,i+1}^{in})^2 + (\Delta\varepsilon_{zx,i,i+1}^{in})^2\right) \right) \tag{6.4}$$

where, $\Delta\varepsilon_{pq,i,i+1}^{in}$ is the difference of the *pq* component of the inelastic strain between the $(i+1)^{th}$ and the i^{th} load step as given by Equation 6.5.

$$\Delta\varepsilon^{in}_{pq,i,i+1} = \varepsilon^{in}_{pq,i+1} - \varepsilon^{in}_{pq,i} \quad 6.5$$

The accumulated total strain for a given element can be determined using Equations similar to 6.4 and 6.5. The inelastic accumulated strain and the total accumulated strain can then be volume averaged similar to the volume averaging technique used for accumulated inelastic work.

6.5.1. Damage Metric Determination

The damage metrics per cycle are known to vary with the number of cycles and tends to stabilize after few cycles. The results from the stabilized cycle should be used for all further analysis. To determine the stabilized cycle, four thermal cycles were simulated and the accumulated volume averaged inelastic work (ΔW_{acc}) was determined for all four cycles. As both stresses and strains are needed to evaluate ΔW_{acc}, it was considered a suitable metric to determine the number of cycles required for the damage metric to stabilize. For all the three packages a thin annular layer, as described in the previous section, for the solder joint under the die edge along the center line was chosen. A plot showing the variation of ΔW_{acc} with number of cycles for all the three package types is given in Figure 6.14. It can be seen from the plot that after three cycles, the ΔW_{acc} tends to stabilize. There is not much variation in the damage metric between the third and fourth cycle. The results from the fourth cycle were therefore used for all subsequent analysis.

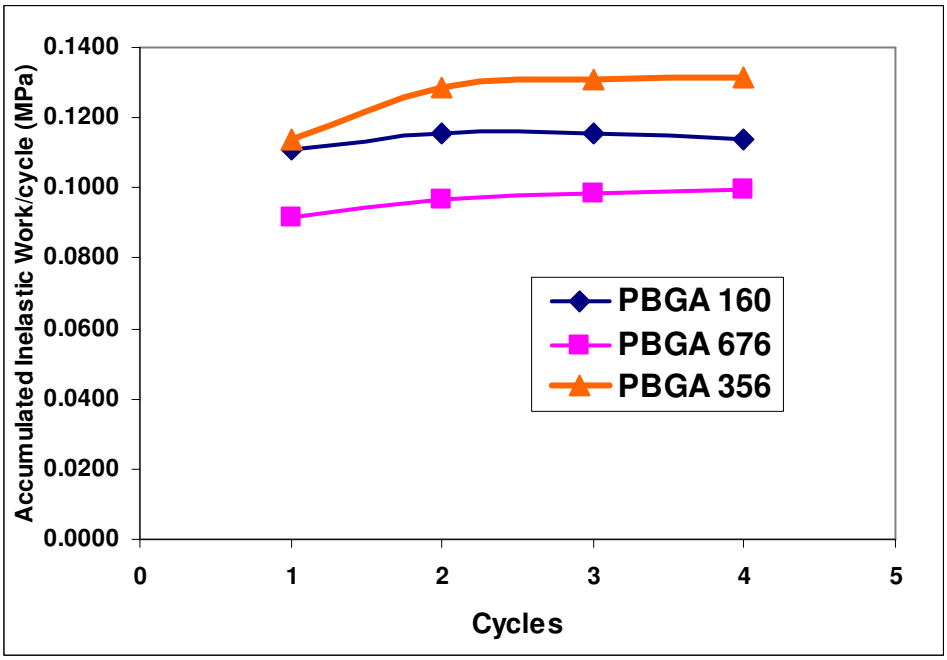

Figure 6.14. Accumulated inelastic work per cycles vs. Cycle count

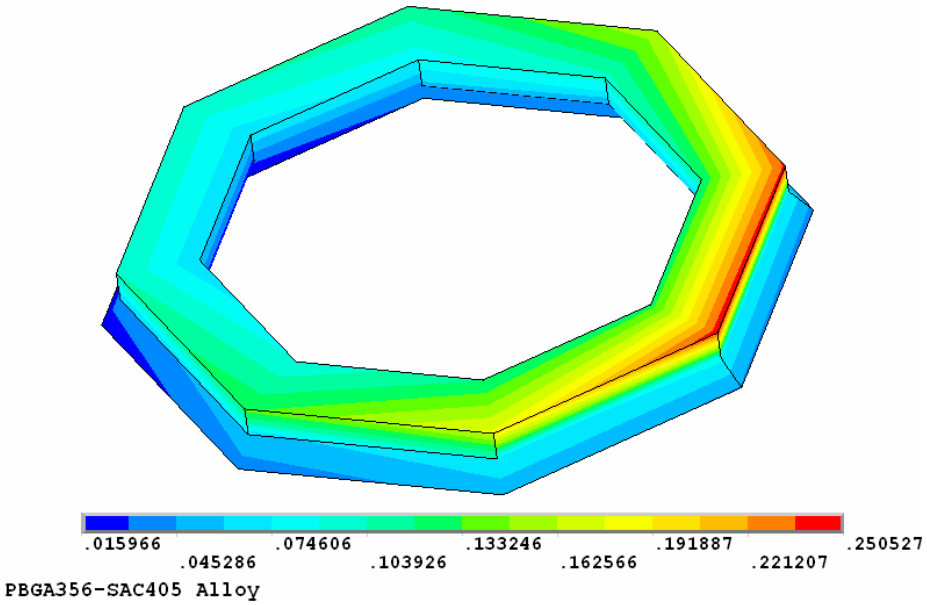

Figure 6.15. Contour plot of the accumulated inelastic work in one stabilized thermal cycle for solder ball under die edge PBGA 356 package

A contour plot showing the variation of the accumulated inelastic work in the annular region for one stabilized thermal cycle for a solder ball under the die edge along the center line of the PBGA 356 package is given in Figure 6.15. It can be seen from the plot that the maximum inelastic work accumulation occurs along a wide angular region along the circumference of the solder joint. Cracks due to thermal fatigue are therefore expected to occur and propagate along a wide angular region along the circumference. This has been verified by other researchers [22] using a dye-n-pry technique.

The volume averaged damage metrics for all the solder joints along the center line of the package were determined. Plots showing the variation of these damage metrics for all the solder joints along the centerline of the package are shown in Figure 6.16, Figure 6.17 and Figure 6.18. Because symmetry was used for modeling the package, only half the number of solder joints along the centerline is shown in the plots. The first solder joint in the plot correspond to the solder joint closest to the centerline of the package and the last solder joint corresponds to the solder joints at the package edge. The location of the die edge for each package is indicated by a vertical line on each of the plots.

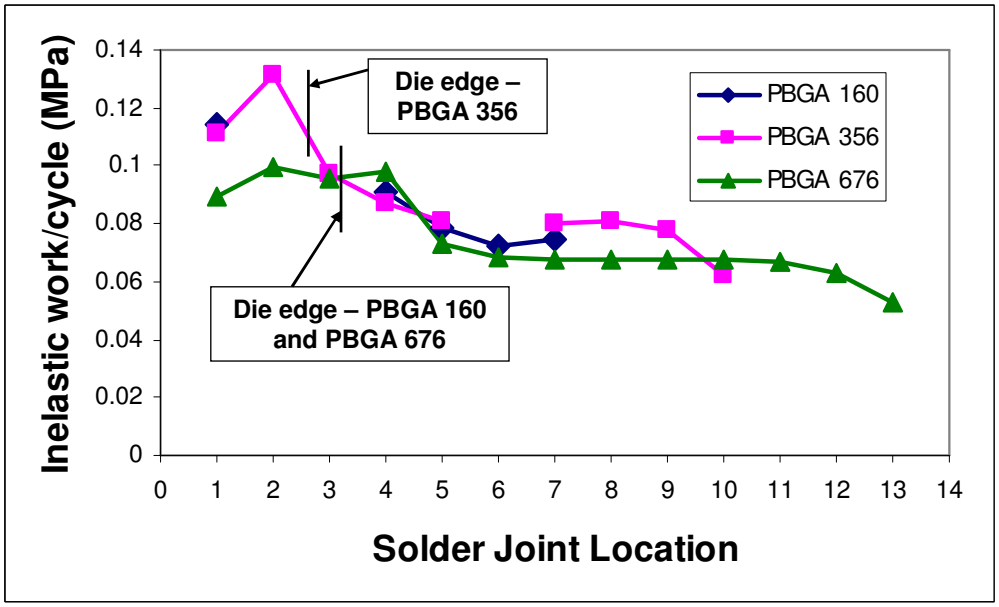

Figure 6.16. Volume averaged accumulated inelastic work for solder joints along the centerline of the package

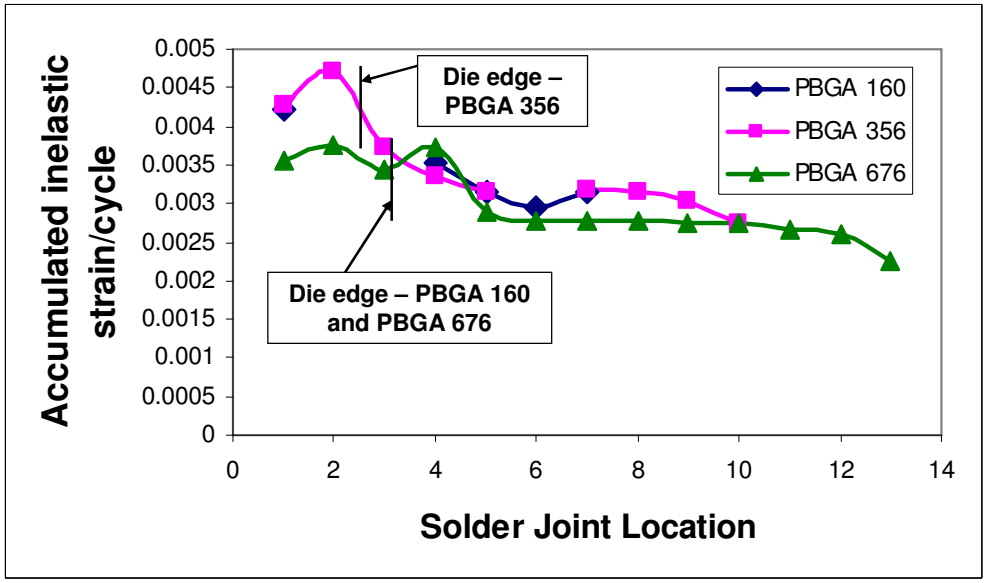

Figure 6.17. Volume averaged accumulated inelastic strain for solder joints along the centerline of the package

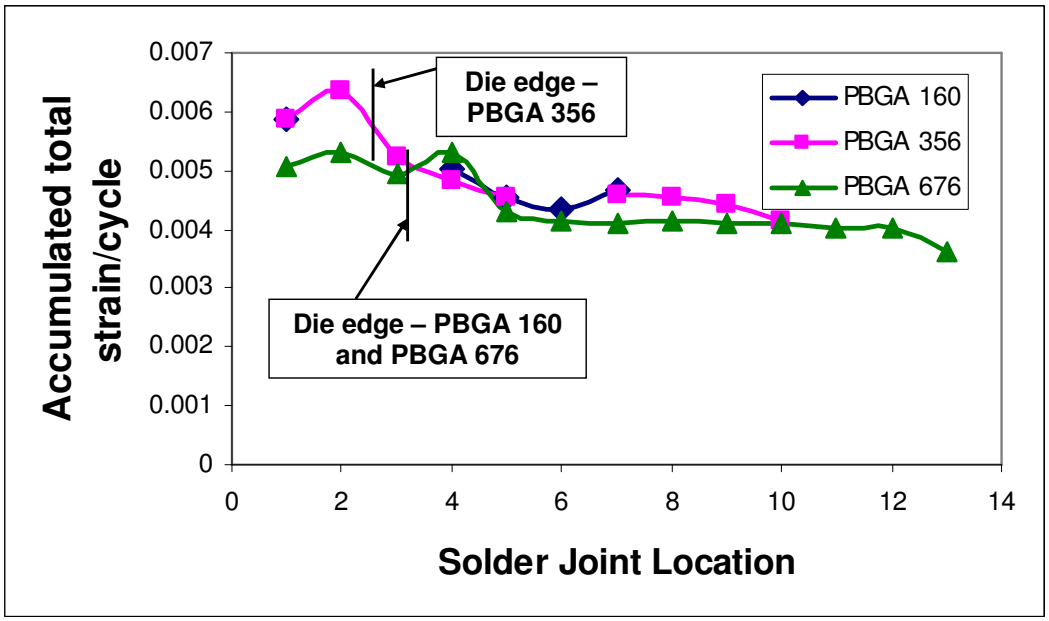

Figure 6.18. Volume averaged accumulated total stain for solder joints along the centerline of the package

Similar trends can be seen in all the three damage metrics for all the three package types. As we move away from the center of the package, the damage metrics in the solder joints increase and reach a maximum for the solder joints located just below the die edge. It then decreases gradually as we move towards the package edge. Increased shear deformation due to CTE mismatch between the silicon chip and the package is the cause for the observed variation. There is very minimal difference between the CTE mismatches between the package substrate and the PCB. The CTE difference between the silicon chip and the PCB therefore has more of an effect in determining this variation.

The variation of all the three damage metrics for PBGA 356 package for solder joints along the centerline is shown in Figure 6.19. All the three damage metrics show similar variation for these solder joints. Any of the above three damage metrics can therefore be used for fatigue life prediction. A solder joint with an increased amount of

any of the three damage metrics has an increased chance of failure due to crack initiation and crack propagation.

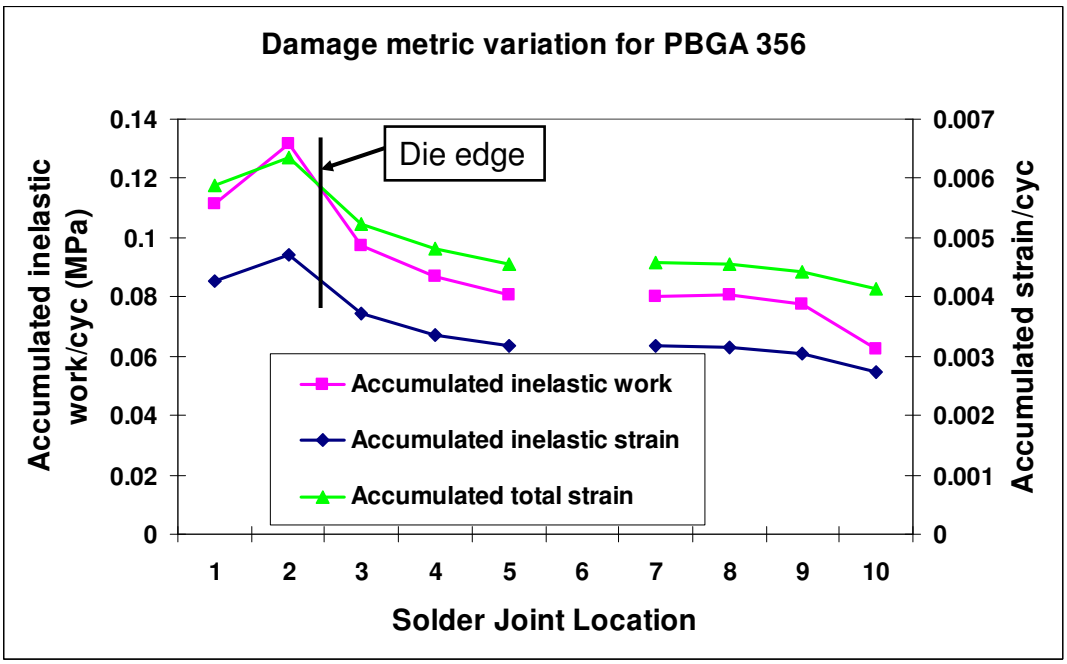

Figure 6.19. Variation of damage metrics for solder joints along the center line of the package for PBGA 356

6.5.2. Normal Strain Determination

Damage metric is just one of the factors determining failure. A solder joint which experiences compressive normal strains, ε_{yy}, in the out-of-plane direction during thermal cycling can be expected to survive for a longer duration in spite of the increased value of any of the three mentioned damage metrics. Compressive strains have an effect of decreasing the rate of crack propagation in the solder joint thereby increasing its fatigue life. The normal strains in the out-of-plane direction should therefore be factored into along with any of the three damage metrics mentioned above in formulating a fatigue life predictive model. None of the existing fatigue prediction models in literature have taken the normal strains in the solder joints into consideration.

The normal strain in the solder joint is a function of temperature. As the whole assembly is cooled down from the reflow temperature, the PCB which has a higher CTE than the package tends to contract more. This makes the whole package-board assembly warp down and leads to the development of compressive stresses and strains in the solder joints near the center of the package. As the temperature is decreased further, this compressive stresses and strains tend to increase. During thermal cycling the package experiences temperatures ranging from -55°C to 125°C. The average of the normal strains at these two temperatures was used as a metric for this study. The variation of the volume averaged normal strains for the solder joints along the centerline of the package is shown in Figure 6.20. The normal strain shown in Figure 6.20 corresponds to the total mechanical strain in the package after subtracting any thermal strains.

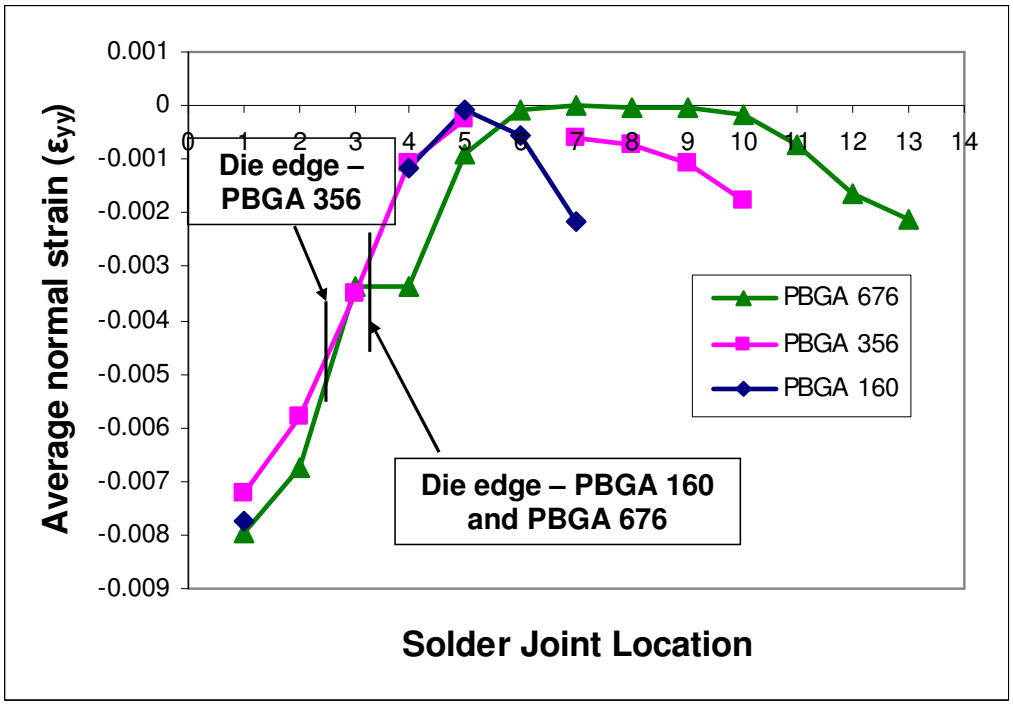

Figure 6.20. Volume averaged normal strain variation for solder joints along the centerline of the package

For all the three package types, the normal strain in the out-of-plane direction is compressive for the solder joint close to the center of the package. The compressive strains tend to decrease as we move away from the center, goes close to zero and then decreases further for solder joints near the package edge. As was discussed in the previous section, the damage metrics tend to be high for solder joints under the silicon die. Increased normal compressive strains in this region imply that the crack propagation will be hindered. This will be observed to be so in the next chapter where crack growth rate will be determined from experiments for solder joints under the silicon die and near the package edge.

CHAPTER 7

CRACK GROWTH ANALYSIS AND PREDICTIVE MODEL FOR SOLDER JOINT FATIGUE LIFE

In this chapter results from the experimental ATC and crack growth study of PBGA packages will be discussed. Based on the experimental results and modeling results from the Chapter 6, predictive equations to predict the solder joint fatigue life will be formulated and fitted. The last section will discuss modifications that need to be introduced to the developed predictive equations to take into account the number of solder joints in a package. A comparison of the fatigue life of the package as estimated from the modified predictive equation and as determined by the experimental ATC will be made.

7.1. ATC and Crack Growth Study

The three different PBGA packages that were studied in the previous chapter were subjected to experimental ATC between -55°C and 125°C. The packages were kept in a basket and the basket was moved between two thermal chambers maintained at -55°C and 125°C. The dwell time at each thermal chamber was 15 minutes and the total cycle time was 30 minutes. The packages were daisy chained and the electrical resistance of the daisy chain was monitored during every 50 cycle intervals. An electrical open as determined from the measured resistance was considered as a failure in the package. The

Weibull plots showing the cumulative failure percentile with number of thermal cycles are shown in Figure 7.1, Figure 7.2 and Figure 7.3.

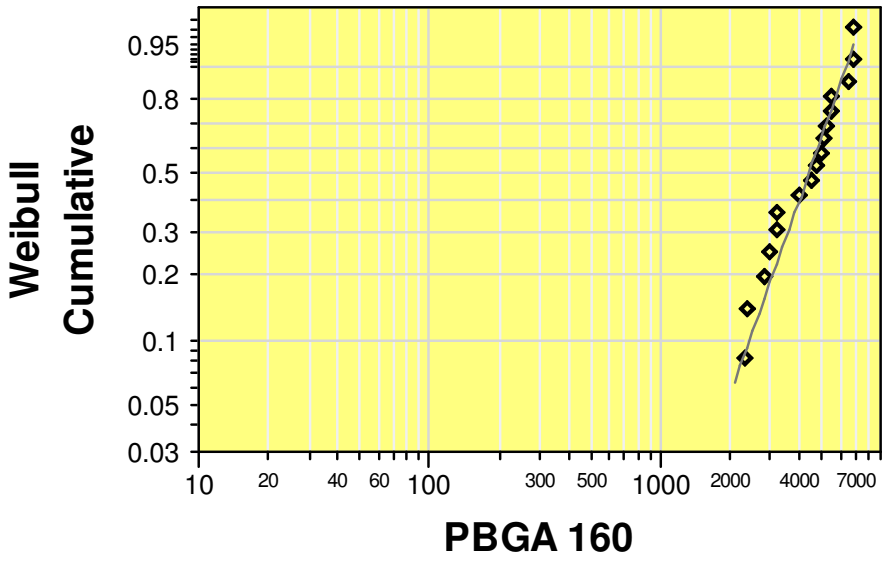

Figure 7.1. Weibull plot for PBGA 160 package

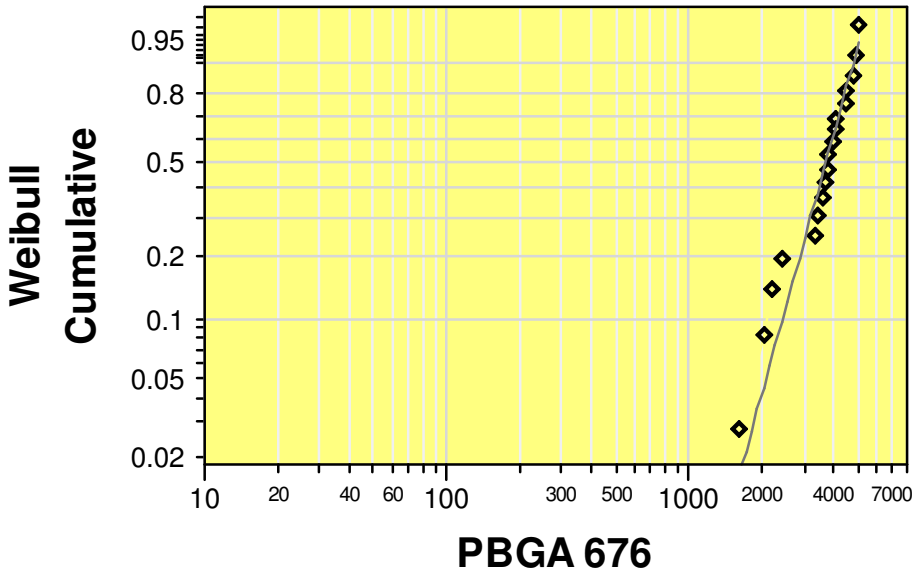

Figure 7.2. Weibull plot for PBGA 676 package

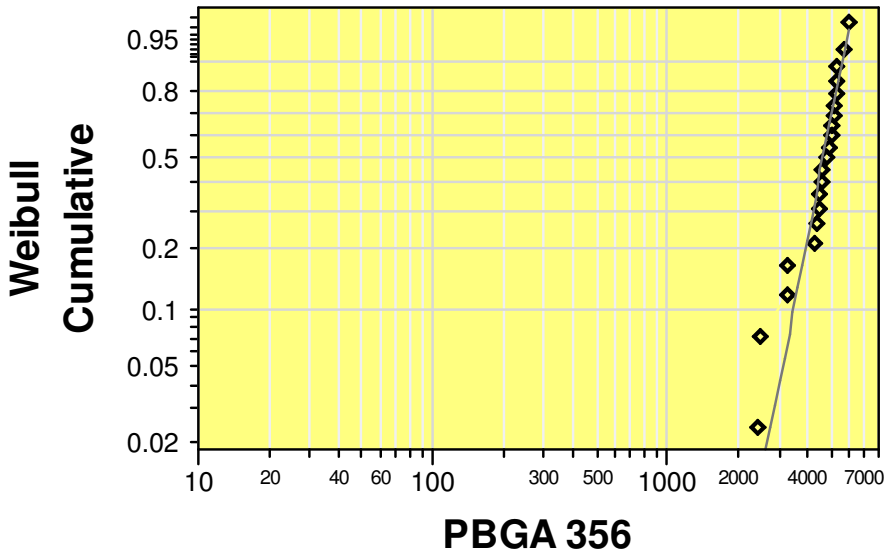

Figure 7.3. Weibull plot for PBGA 356 package

A three-parameter Weibull distribution has been found to be suitable for predicting the failure of PBGA packages [70]. The governing equations for the three-parameter Weibull distribution is given in Equation 7.1. F is the cumulative failure percentile for the package, N_{ff} is the failure-free life of the package, α is the characteristic life of the package and β is the shape factor for the Weibull distribution.

$$F = 0 \qquad for \quad N < N_{ff}$$
$$F = 1 - \exp\left[-\left(\frac{N - N_{ff}}{\alpha - N_{ff}}\right)^{\beta}\right] \qquad for \ N > N_{ff} \qquad 7.1$$

JMP® software was used to find the characteristic life and the shape factor for the Weibull failure plots. The number of PBGA packages used, the mean life, the characteristic life, failure-free life and the shape factor for the Weibull plots are shown in

Table 7.1. The failure-free life was obtained by finding the number of cycles for first failure for a given package type. The ratio of the failure-free life to the characteristic life for all three package types lies between 0.42 to 0.49. This agrees very well with the large database of thermal cycling results from Clech et al [70], where an average value of 0.46 was reported. The mean life was obtained from Equation Table 7.1 by setting the value of *F* to 0.5. PBGA 160 has a higher fatigue life compared to PBGA 676 package due to its smaller size. PBGA 356 package has a higher fatigue life compared to PBGA 676 package due to its higher standoff height. However, the differences between the fatigue lives are not very substantial as the differences between the shape factors for the three package types.

Table 7.1. Weibull plots parameters for PBGA packages

Package Type	Total number of packages	Mean Life ($N_{50\%}$)	Characteristic life ($N_{63.2\%}$)	Failure-free life (N_{ff})	$N_{ff}/N_{63.2\%}$	Shape factor - β
PBGA160 – SAC405	18	4649	4916	2100	0.427	3.19
PBGA676 – SAC405	18	3750	4006	1650	0.412	4.57
PBGA356 – SAC405	21	4639	4912	2400	0.488	6.51

7.2. Shape Factor and Number of Solder Grains

Even though there is not much variation seen in the characteristic life to package failure, there is significant variation in the shape factor between all the three package types. Shape factor is an indication of the rapidity of package failure. Package types which fail rapidly will have a high slope in the Weibull plot. Historically, the shape factor has been known to be associated with process variations, assembly variations, different package types, different board types and finishes, different lots from different suppliers, different assembly processes, different solder compositions, different paste compositions,

different fluxes, etc. However, for the present study, the PBGA packages were obtained from the same vendor; PCB boards, solder fluxes and assembly process were also similar. Therefore, other factors play into the variation of the shape factor between different package types. One difference among the different packages is the different solder volume and therefore, different number of solder grains per solder joint. Grains near the copper pads influence the local CTE mismatch; lesser grains at the interface will indicate more variations in CTE mismatch and thus lesser shape factor.

Table 7.2. Variation of shape factor with solder volume

Package Type	Shape factor - β	Average grains per solder cross-section (50 joints)	Solder Volume
PBGA160 – SAC405	3.19	1.54±0.787	0.067mm^3
PBGA676 – SAC405	4.57	2.60±1.80	0.119mm^3
PBGA356 – SAC405	6.51	3.19±2.39	0.208mm^3

The average grains per solder cross section and the volume of the solder joints for all the three package types is shown in Table 7.2. The average grains were determined from a sample size consisting of 50 solder joints. The wide variation in the shape factor between the packages can be explained as being due to small number of tin grains in the solder joint leading to anisotropy. Copper pad has a CTE of about 17ppm/°C. Tin has a CTE varying from 15ppm/°C to 30ppm/°C depending on its orientation. A solder joint having a tin grain with a CTE of 15ppm/°C in contact with the copper pad is oriented favorably and is going to have a lower crack growth rate compared to a solder joint having a tin with CTE of 30 ppm/°C in contact with the copper pad. The grains in the solder joints are oriented randomly and the orientation cannot be predicted. A package having solder joints with fewer grains is therefore likely to exhibit wide variation in the crack growth rate and this reflects as wide variation in the package life. A wide variation

in the package life means a smaller shape factor. It can be seen in Table 7.2 that PBGA 160 has on an average fewer grains as observed in a solder joint cross-section compared to the other two packages. PBGA 160 therefore has a small shape factor compared to the other two packages.

The average number of grains in a solder depends on the volume of the solder joint with the number increasing with the volume of the solder. This is because a higher solder volume implies more potential sites for the grain nucleation to take place during cool down from the reflow process[31]. If the solder volume increases, the influence of the anisotripic microstructure increases. This reflects as more statistical scatter in lives of the packages and therefore lower value of shape factor. A plot showing the variation of the shape factor with the solder joint volume is given in Figure 7.4. The variation can be seen to be almost linear within the solder joint volume range considered.

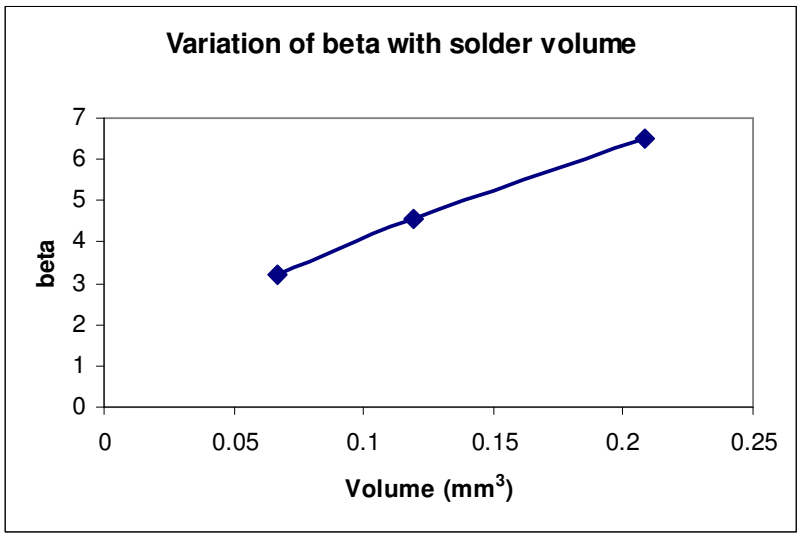

Figure 7.4. Variation of shape factor with solder volume

7.3. Experimental Crack Initiation and Propagation Analysis

As a next step towards obtaining data for predictive model development, the crack growth rate in the solder joint needs to be measured experimentally. Two of the three PBGA packages, PBGA 676 and PBGA 356, were chosen for the crack growth measurement study. The third package, PBGA 160 was chosen for verification of the developed predictive model which will be discussed in a later section.

Several packages belonging to PBGA 356 and PBGA 676 package types were placed in a thermal chamber and subjected to ATC between -55°C and 125°C. Three of these packages were taken out at various intervals of time ranging from 0 ATC to about 8000 ATCs. The packages were cross-sectioned along the center line to observe the cracked solder joint cross-section. The ball array matrix for PBGA 676 and PBGA 356 packages are shown in Figure 7.5 and Figure 7.6 respectively. Both the packages had even number of rows of solder joints. Two cross-sections per package, along AA and along BB, were therefore taken to observe the cracked solder joints along the center line the package. As the packages had symmetry, two cross-sections provide four data points for crack growth measurement of a solder joint at a given location. Since three packages were taken out after completing a number of ATCs, twelve data points per solder joint were obtained for crack growth measurement. Recent research study [22, 71] has shown that for PBGA packages, solder joint failures typically occur either below the die shadow region or below the edge of the package. The FEA discussed in the previous chapter has also shown that wide variation of damage metrics and normal strains are observed for the solder joints under the die and for the solder joints near the package edge - Figure 6.16 through Figure 6.20. Crack growth measurements were therefore made for only these

solder joints. The solder joints chosen for crack growth measurements have been shaded in Figure 7.5 and Figure 7.6.

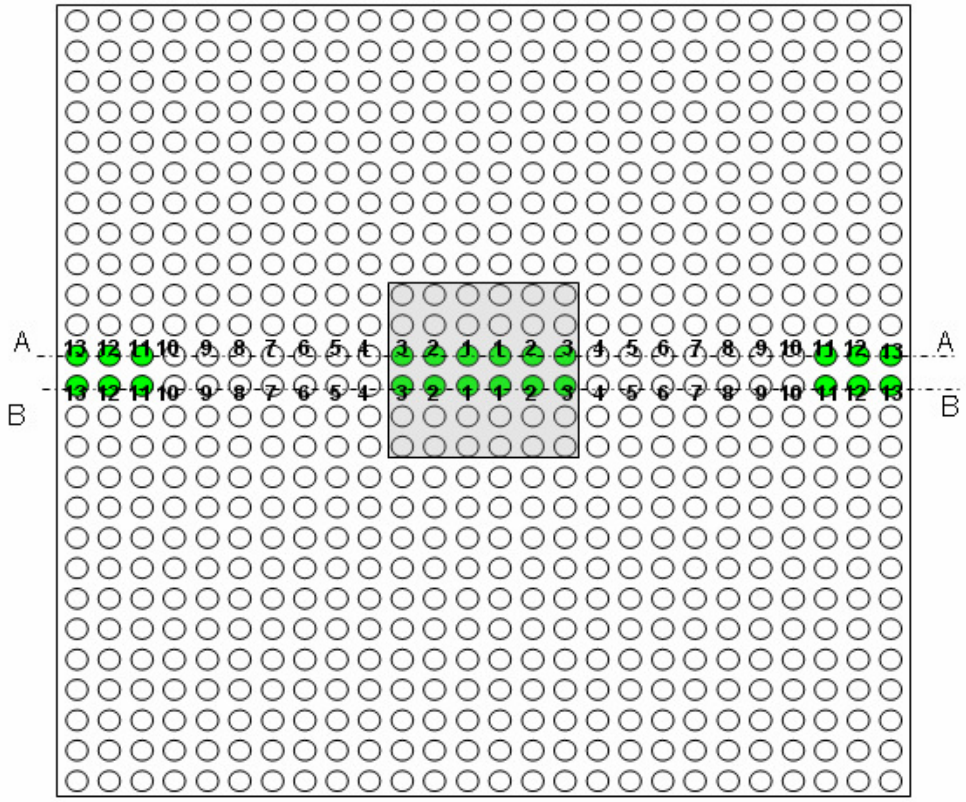

Figure 7.5. Ball array matrix for PBGA 676

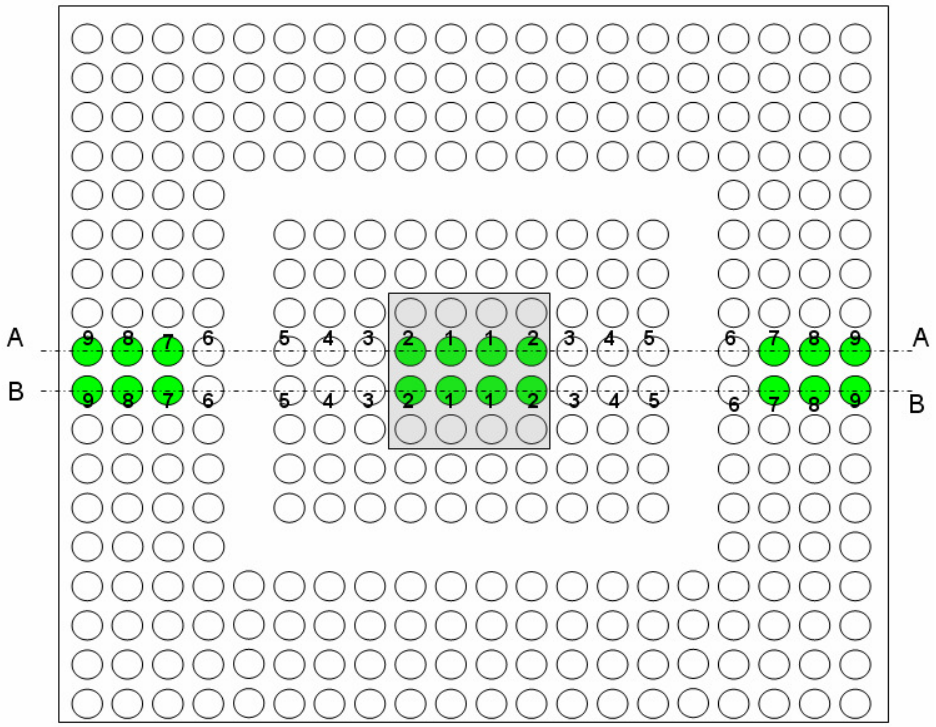

Figure 7.6. Ball array matrix for PBGA 356

Solder joint cracking was observed mostly at the package side copper pad and the solder joint interface. Solder joint cracking was observed at the board side of the solder joint only after several thousand cycles. Also, Its length was significantly less than the length of the cracks seen on the package substrate side of the solder. All measurements were therefore made at the solder joint and copper pad interface at the package side. As was mentioned in the previous Chapter, the solder cracks typically occur and propagate along the circumference. However, when the solder joint is cross-sectioned, only horizontal linear cracks in the cross-sectioned area can be seen. The variation of crack length with number of cycles for a solder joint under the die edge (solder joint #3) and for a solder joint under the package edge (solder joint #12), in PBGA 676 package is shown in Figure 7.7 and Figure 7.8. The images were captured using an optical microscope. Crack was observed to occur at both sides of the solder joint fillet in a horizontal

direction. The sum of the crack lengths at these two corners was used to measure the total crack length. If the crack length was inclined, the horizontal projection of crack was used to find the total crack length.

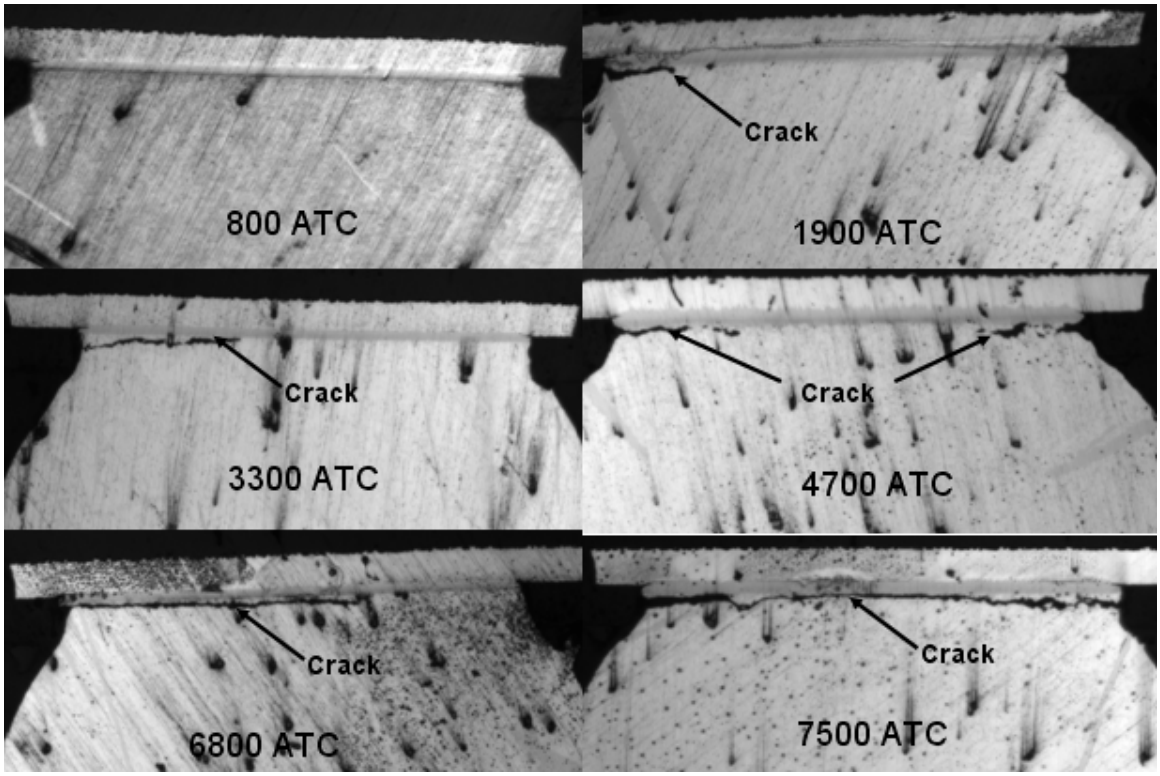

Figure 7.7. Crack growth seen in the solder joint underneath the die edge (joint #3) in a PBGA 676 package

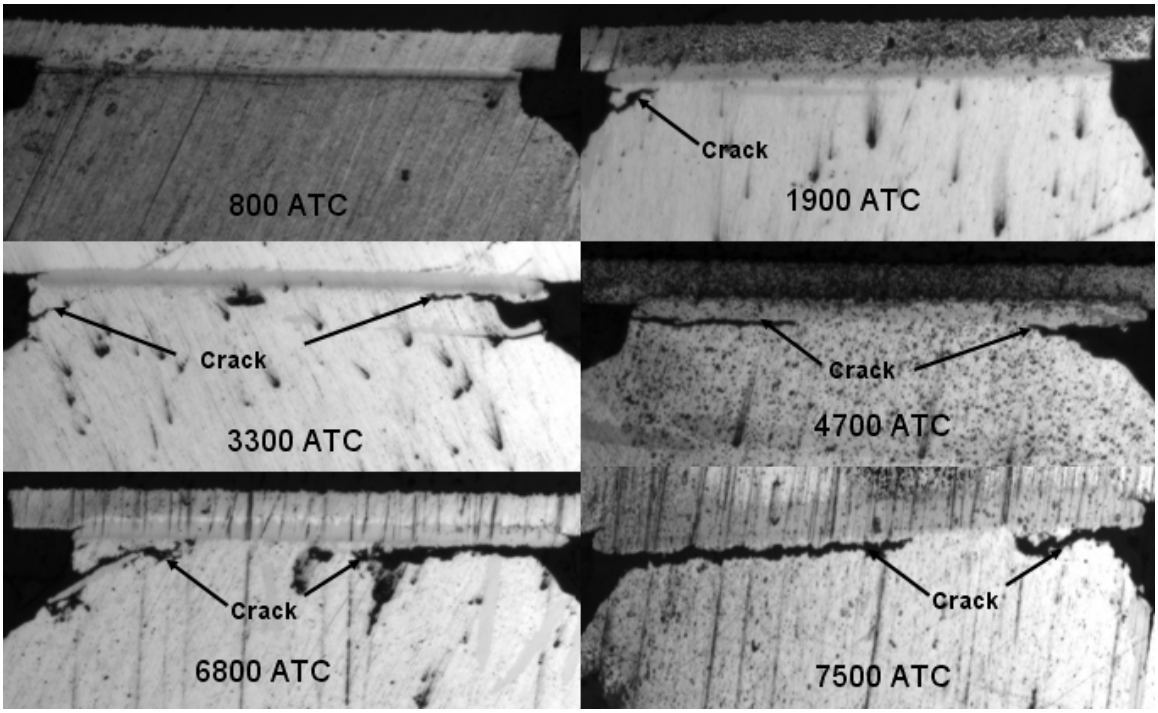

Figure 7.8. Crack growth seen in the solder joint underneath the die edge (joint #12) in a PBGA 676 package

Crack lengths as a function of number of cycles were measured for PBGA 676 package for all six symmetric shaded solder joints shown in Figure 7.5. The mean and the standard deviation in the measured crack length were computed for all twelve data points for a given solder joint. The variation of the measured crack length with number of cycles for solder joint numbers 3 and 12 is shown in Figure 7.9 and Figure 7.10 respectively. Any outliers were taken out before charting the plots. The outliers were defined as any point with standardized residual greater than three [72].

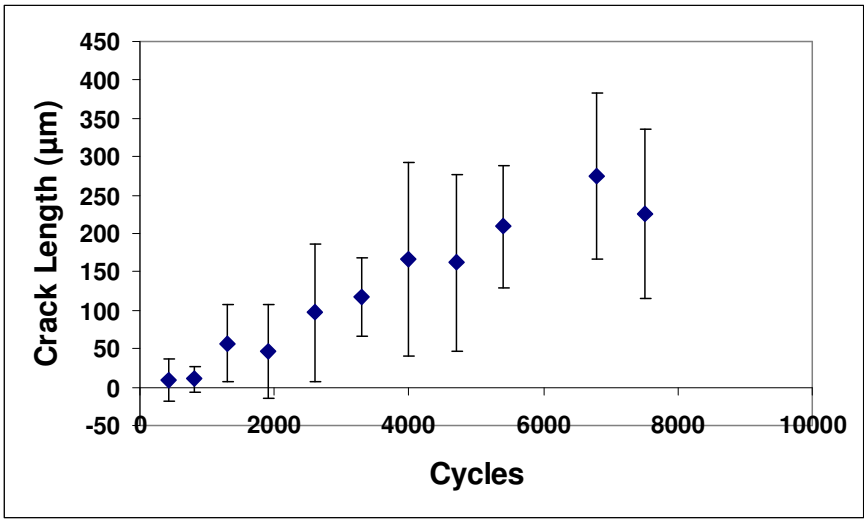

Figure 7.9. Fatigue crack growth for a solder joint #3 in PBGA 676 package

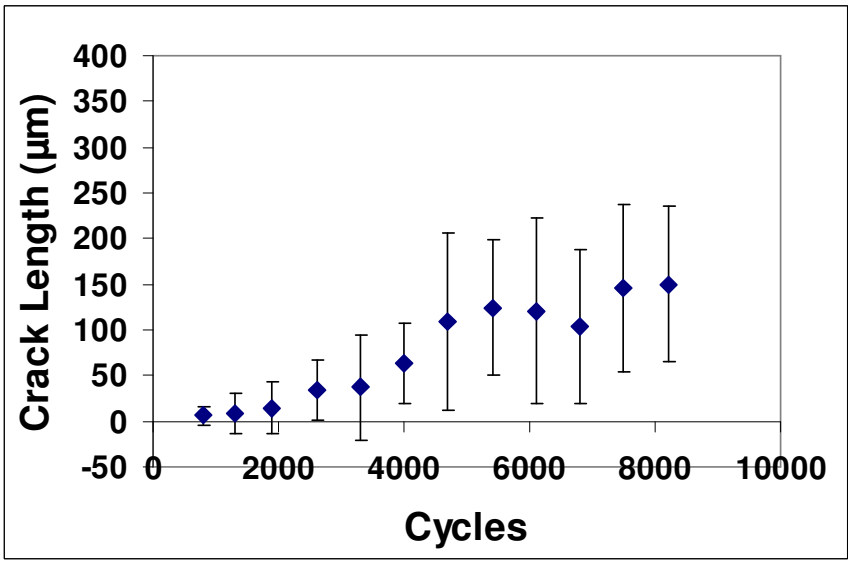

Figure 7.10. Fatigue crack growth for a solder joint #12 in PBGA 676 package

The crack growth for solder joints in the PBGA 356 package as a function of number of cycles was also determined. The crack growth for a solder joint underneath the die edge (solder joint #2) and for a solder joint underneath the package edge (solder joint #8) as a function of number of cycles is shown in Figure 7.11. As was seen for the solder

joint in the PBGA 676 package, the crack in the solder joint in the PBGA 356 package was also seen to propagate horizontally. Since crack was seen to propagate from both sides of the solder joint fillet, the sum of the crack lengths was used to find the total length of the crack.

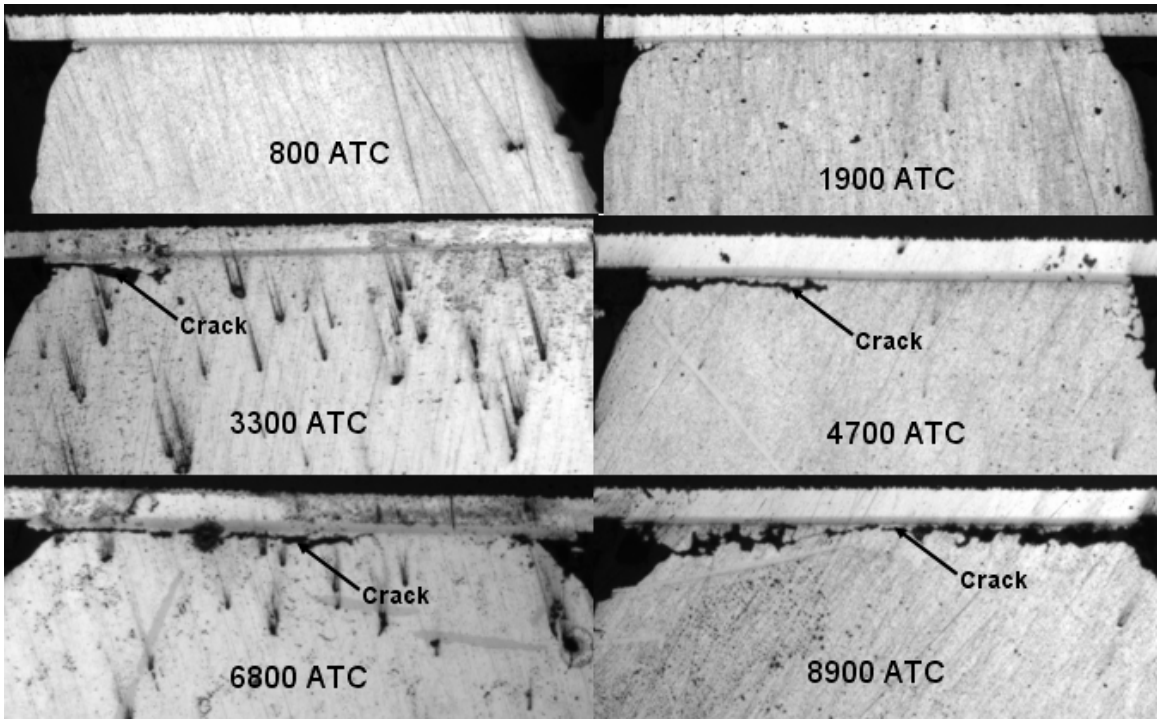

Figure 7.11. Crack growth seen in the solder joint underneath the die edge (joint #2) in a PBGA 356 package

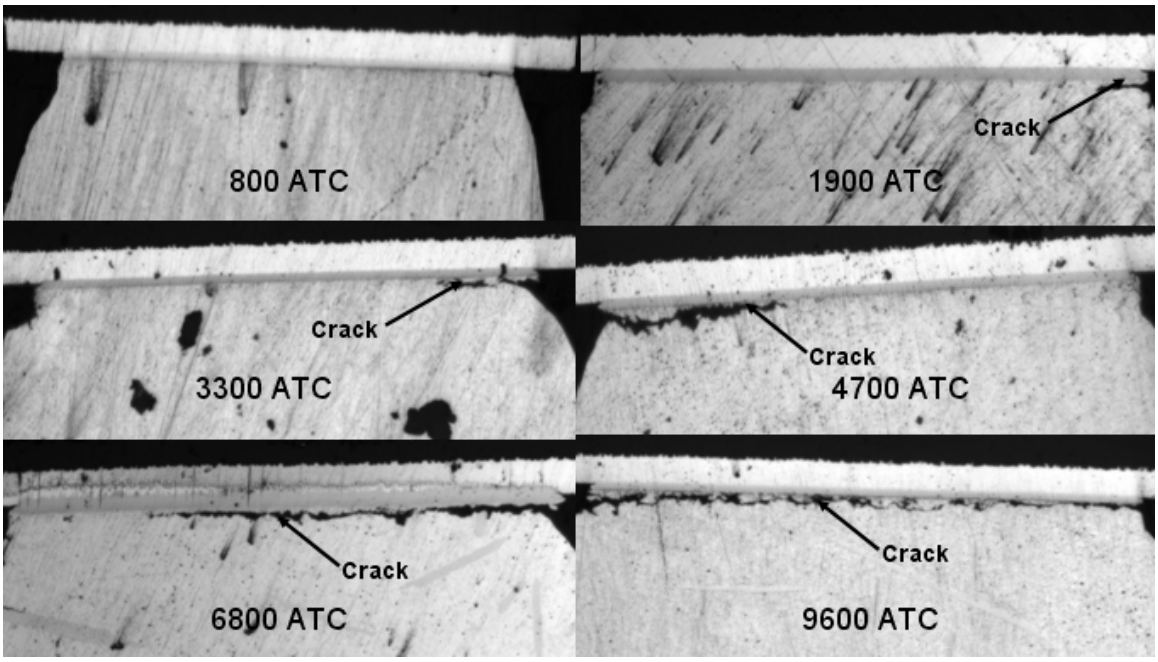

Figure 7.12. Crack growth seen in the solder joint underneath the package edge (joint #8) in a PBGA 356 package

The lengths of the cracks were measured for all the five symmetric shaded solder joints shown in Figure 7.6. Similar to what was done for PBGA 676 package, the mean and the deviation in the crack length was computed based on the measured lengths from twelve data points per solder joint. A plot showing the variation of the measured crack length with number of cycles is shown in Figure 7.13 and Figure 7.14.

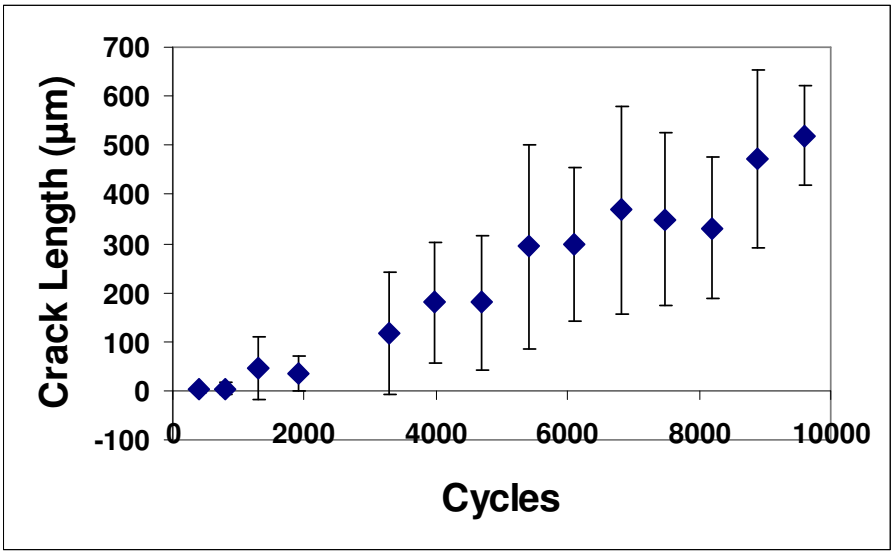

Figure 7.13. Fatigue crack growth for a solder joint #2 in PBGA 356 package

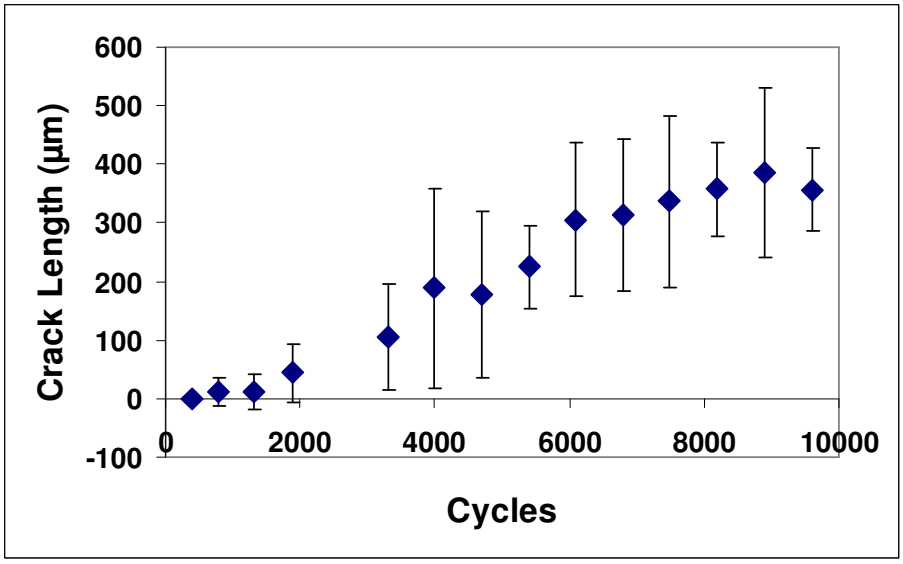

Figure 7.14. Fatigue crack growth for a solder joint #8 in PBGA 356 package

7.4. Crack Initiation Analysis

Fatigue model development also requires finding the number of cycles for crack initiation in addition to the determining the crack growth rate. The number of cycles for crack initiation is known to be a small fraction of the total life of the solder joints. Darveaux [18] has found the number of cycles for crack initiation by finding the intercept of the crack growth plot, similar to the one shown in Figure 7.9, with the horizontal axis. This is however not a recommended method for PBGA packages where cracks can grow for 8000 cycles or more. Data points at the ends of the fitted crack growth line are known to highly influence the number of cycles for crack initiation. Any small error in the crack measurement near the ends of the fitted line will lead to huge error in the intercept value [72]. Number of cycles for crack initiation was therefore found by measuring the length of the crack in 400 to 500 cycle intervals starting from 0 ATC to 2000 ATCs. If the measured crack length was found to be greater than 2% of the solder ball diameter at the copper pad-solder interface, crack was considered to have been initiated. The number of cycles for crack initiation as determined from both the methods described above for the solder joints considered are shown in Table 7.3 and Table 7.4. As can be seen from both the tables, there is significant error in the N_o value found from the intercept method. The interval method was therefore used for all further analysis. It should be pointed that if the intervals chosen were smaller, i.e. of the order of 50 to 100 cycles, a more accurate estimate of N_o could have been achieved. This would have required about ten times more sample size chosen. However, considering that N_o accounts for only about 10% of the life of the solder joint, a 400 to 500 cycle intervals was deemed sufficient.

Table 7.3. Measured number of cycles for crack initiation for solder balls in PBGA 676 package

PBGA 676 – Solder Joint Number	PBGA 676 – N_o (cycles) by interval method	PBGA 676 – N_o (cycles) by intercept method
1	1900	422
2	1900	98
3	810	104
11	810	653
12	810	978
13	1300	1320

Table 7.4. Measured number of cycles for crack initiation for solder balls in PBGA 356 package

PBGA 356 – Solder Joint Number	PBGA 356 – N_o (cycles) by interval method	PBGA 676 – N_o (cycles) by intercept method
1	1300	42
2	800	460
7	800	505
8	800	698
9	800	1363

7.5. Crack Propagation Analysis

The crack growth as a function of number of thermal cycles is seen to be close to linear. However, huge deviation can be seen in the measured crack length. This deviation can be explained due to anisotropy of tin grains which are present in small numbers in a solder joint. For both the packages, the deviation is seen to be low initially and tends to increase after 2000 cycles. The crack growth rate was obtained by liner curve fitting the crack growth plots for PBGA 676 and PBGA 356 package. The measured crack growth rates along with the R^2 value obtained from the fit for all the solder joints in the two packages under the die and near the package edge are shown in Table 7.5 and Table 7.6 and plotted in Figure 7.15.

Table 7.5. Measured values of crack growth rates for PBGA packages

PBGA 676 – Solder Joint Number	PBGA 676 – da/dN (µm/cycle)	R^2 value from fit
1	0.0235	0.9532
2	0.0267	0.9486
3	0.0385	0.9432
11	0.0412	0.9400
12	0.0352	0.7957
13	0.0280	0.8932

Table 7.6. Measured values of crack growth rates for PBGA packages

PBGA 356 – Solder Joint Number	PBGA 356 – da/dN (µm/cycle)	R^2 value from fit
1	0.0405	0.9514
2	0.0517	0.9757
7	0.0507	0.9697
8	0.0467	0.9818
9	0.0403	0.9627

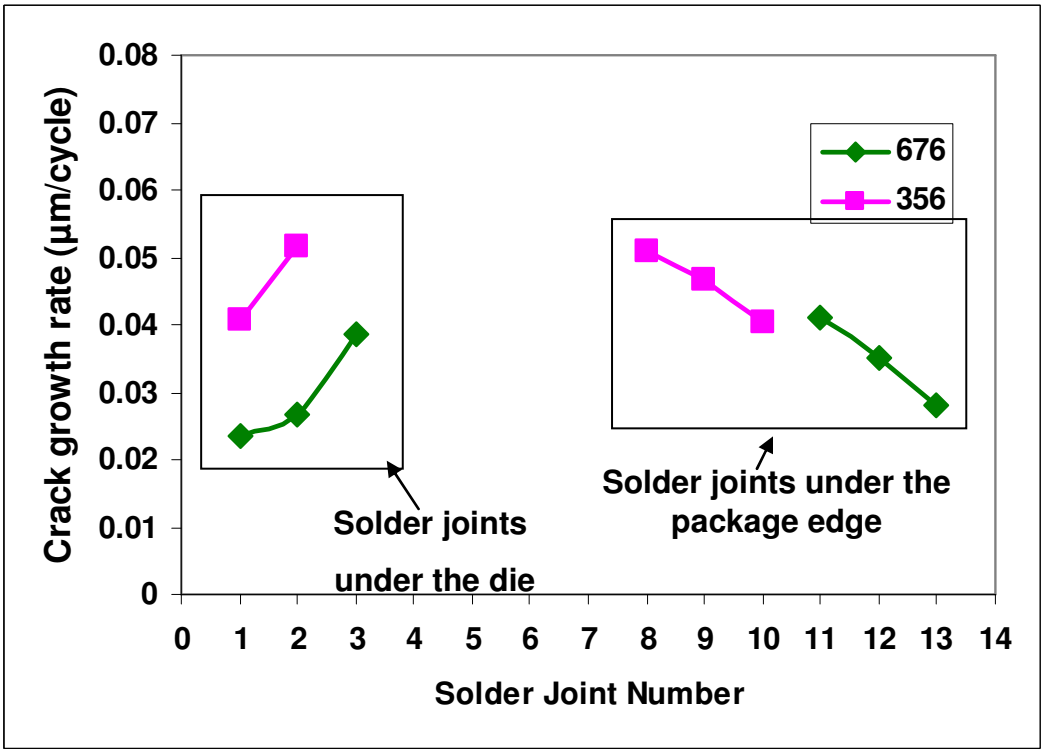

Figure 7.15. Plot of measured values of crack growth rate

For both the package types, under the die, the crack propagation rate continues to increase as we move towards the die edge. The crack propagation rate is roughly the same for a solder joint near the die edge as well as for a joint three rows inside from the package edge. This is due to the presence of increased compressive normal strains, as shown in Figure 6.16 through Figure 6.18, for the solder joints underneath the silicon die. Between the two packages, the PBGA 356 package has a higher crack growth rate compared to PBGA 676 package.

7.6. Failure-free Life and Crack Length

The crack growth rate described in the previous section was obtained by fitting a linear curve to the mean crack length at each data point. This mean crack growth rate can be used to estimate the mean fatigue life of the solder joint. It is possible that the maximum crack length in a given sample after a certain number of thermal cycles can propagate through out the width of the solder joint and cause failure much earlier. If the maximum crack length is used to estimate the fatigue life of the solder joint, the failure-free life of the solder joint can be obtained. A plot of maximum crack length versus mean crack length after combining data from all the solder joints in PBGA 676 and PBGA 356 package is shown in Figure 7.16. The average ratio of the maximum to mean crack length was estimated by fitting a linear curve to the data and by setting the intercept to zero. An average ratio of 1.8 was obtained from the curve fit. Based on experimental crack growth measurements performed by Darveaux [73, 74] on a number of solder joints used in a BGA packages, the maximum crack length in the solder joint was found to be approximately twice the characteristic length. The obtained value is therefore very close

to the value reported in literature. The maximum crack growth rate can be obtained by multiplying the mean crack growth rate with 1.8. The maximum crack growth rate can then be used to estimate the failure-free life of the package.

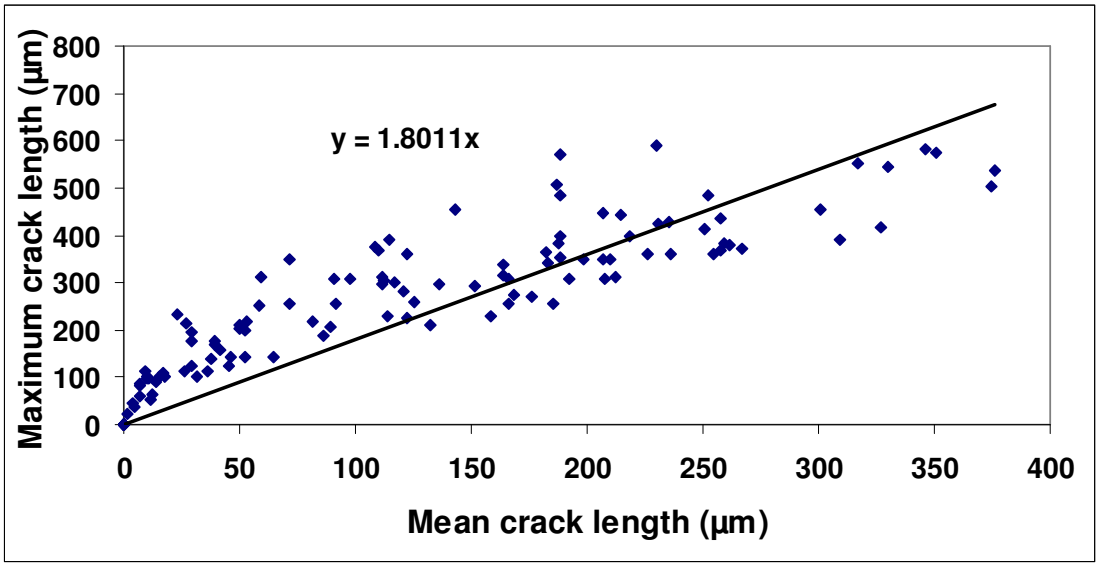

Figure 7.16. Plot of maximum crack length vs. mean crack length

7.7. Fatigue Model Development

Developing a fatigue life predictive model involves finding the number of cycles for crack initiation and the crack growth rate for a solder joint by correlating the results from simulation and results from the crack growth study. A Coffin-Manson type fatigue life equation has been used by many researchers [17, 21, 75] to determine the fatigue life of solder joints by relating the damage metric to number of cycles to failure. For the present study, the non-linear equation similar to Coffin-Manson has been used and has been modified to include the effect of normal strains in the solder joint. A non-linear dependency of normal strains with number of cycles for crack initiation and crack propagation has been assumed and the normal strain has been normalized with the damage metric. The formulation for all the three damage metrics is shown in Equations

7.2 through 7.7. N_o is the number of cycles for crack initiation, ΔW_{acc} is the accumulated inelastic work per thermal cycle, $\Delta\varepsilon^{in}_{acc}$ is the accumulated inelastic strain per thermal cycle, $\Delta\varepsilon^{tot}_{acc}$ is the accumulated total strain per thermal cycle, ε_n is the normal strain in the solder joint, *da/dN* is the crack growth rate in the solder joint and C_1 through C_8 are constants which needs to be found by fitting the modeling results with experimental results. In Equations 7.2 and 7.3, $\Delta\varepsilon^{in}_{acc}$ has been used to normalize the normal strains even though the damage metric used was ΔW_{acc}. This was done to ensure that the constants C_2 and C_6 are non-dimensional.

$$N_o = C_1\left(1 + C_2\frac{\varepsilon_n}{\Delta\varepsilon^{in}_{acc}}\right)^{C_3}\left(\Delta W_{acc}\right)^{C_4} \tag{7.2}$$

$$da/dN = C_5\left(1 + C_6\frac{\varepsilon_n}{\Delta\varepsilon^{in}_{acc}}\right)^{C_7}\left(\Delta W_{acc}\right)^{C_8} \tag{7.3}$$

$$N_o = C_1\left(1 + C_2\frac{\varepsilon_n}{\Delta\varepsilon^{in}_{acc}}\right)^{C_3}\left(\Delta\varepsilon^{in}_{acc}\right)^{C_4} \tag{7.4}$$

$$da/dN = C_5\left(1 + C_6\frac{\varepsilon_n}{\Delta\varepsilon^{in}_{acc}}\right)^{C_7}\left(\Delta\varepsilon^{in}_{acc}\right)^{C_8} \tag{7.5}$$

$$N_o = C_1\left(1 + C_2\frac{\varepsilon_n}{\Delta\varepsilon^{tot}_{acc}}\right)^{C_3}\left(\Delta\varepsilon^{tot}_{acc}\right)^{C_4} \tag{7.6}$$

$$da/dN = C_5\left(1 + C_6\frac{\varepsilon_n}{\Delta\varepsilon^{tot}_{acc}}\right)^{C_7}\left(\Delta\varepsilon^{tot}_{acc}\right)^{C_8} \tag{7.7}$$

Non-linear regression was used to fit the crack growth rate, given in Table 7.5, and number of cycles for crack initiation, given in Table 7.3, to the damage metrics and normal strains in the solder joints found from simulations. Fitting constants using non-linear regression requires providing initial estimates for the constants. The constants are varied starting from the initial guesses until a local minimum for the objective function (either N_o or da/dN) is obtained. Depending on the initial guesses given for the constants, various possible local minima and hence various possible fitted constants are possible. To prevent this from happening, the constants C_4 was varied from -1.5 to -1.6 and C_8 was varied from 0.95 to 1.25 until a low root mean square error (RMSE) was obtained. The fitted constants are given in Table 7.7 and Table 7.8. The RMSE which is a measure of goodness of a non-linear fit is also indicated in the two Tables.

Table 7.7. Fitted constants for number of cycles for crack initiation

Damage metric	C_1	C_2	C_3	C_4	RMSE
ΔW_{acc}	5.52	-0.834	2.1	-1.55	325.99
$\Delta \varepsilon_{acc}^{in}$	0.0448	-0.736	2.05	-1.55	272.02
$\Delta \varepsilon_{acc}^{tot}$	0.101	-0.871	2	-1.55	197.24

Table 7.8. Fitted constants for the crack growth rate in a solder joint

Damage metric	C_5	C_6	C_7	C_8	RMSE
ΔW_{acc}	0.667	0.116	3.5	0.98	0.00377
$\Delta \varepsilon_{acc}^{in}$	57.59	0.096	4.43	1.2	0.00258
$\Delta \varepsilon_{acc}^{tot}$	36.9	0.233	2.05	1.2	0.00322

The RMSE for crack growth rate is almost an order of magnitude lower than the typical crack growth rate shown in Table 7.5. This indicates that there is a good correlation between modeling results and experiments for crack growth rate. The RMSE for the number of cycles for crack initiation is about one fourth the typical numbers of cycles for crack initiation shown in Table 7.3. This high RMSE could possibly be due to weak dependency of crack initiation with compressive normal strains in the solder joint. It could also be because crack initiation was measured at 400-500 cycle intervals. Once the number of cycles for crack initiation and mean crack growth rate is found for the solder joint, the total number of cycles to failure, N_t can be determined from Equation 7.8.

$$N_t = N_o + \frac{2R}{da/dN} \qquad 7.8$$

where, R is the radius of the solder joint at the neck region. The failure-free life, N_{ff}, of the package can be determined by using the maximum crack growth rate, as determined from Figure 7.16, instead of the mean crack growth rate as shown in Equation 7.9.

$$N_{ff} = N_o + \frac{2R}{1.8(da/dN)} \qquad 7.9$$

7.8. Model Validation Based on Critical Solder Joint

PBGA 160 package was used to verify the developed predictive model with experimental results from ATC. The fatigue life for all the solder joints in the PBGA 160 package was estimated using all the three damage metrics. A contour plot of the accumulated inelastic work during one thermal cycle is shown in Figure 7.17. The damage metric is seen to be highest in the solder joint underneath the die.

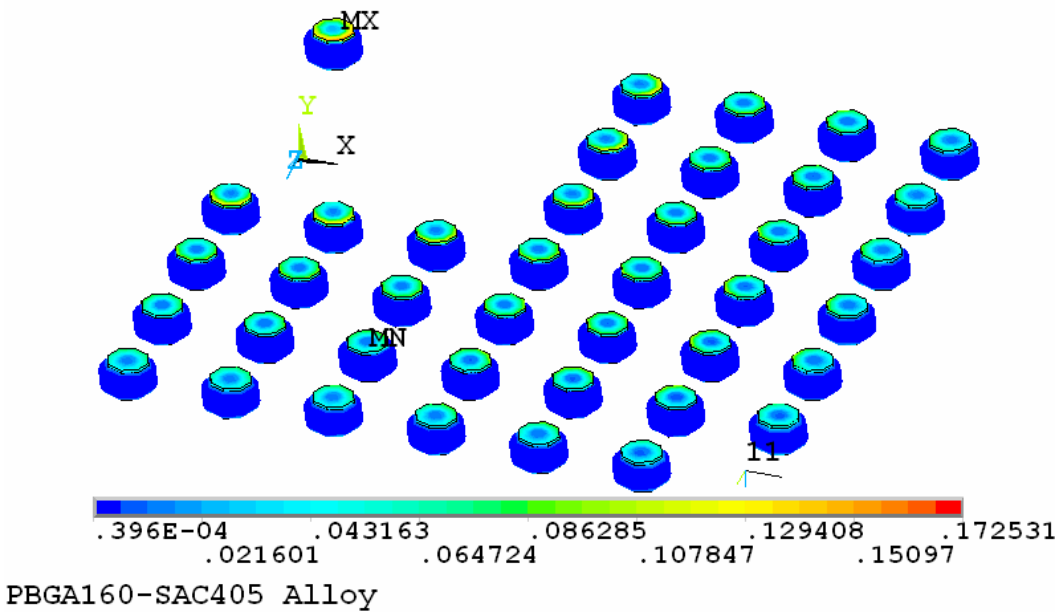

Figure 7.17. Contour plot of accumulated inelastic work during one ATC

The fatigue lives estimated from the developed models are shown in Figure 7.19, Figure 7.20 and Figure 7.21. Each cell represents a solder joint as shown in the shaded region of Figure 7.18. The fatigue lives were estimated using Equations 7.2 through 7.7. The value in the top left corner represents the solder joint close to the center of the package. The solder joint with the least number of cycles to failure is shaded. Slight asymmetry can be seen in the predicted life due the board extending to different lengths in both the perpendicular directions.

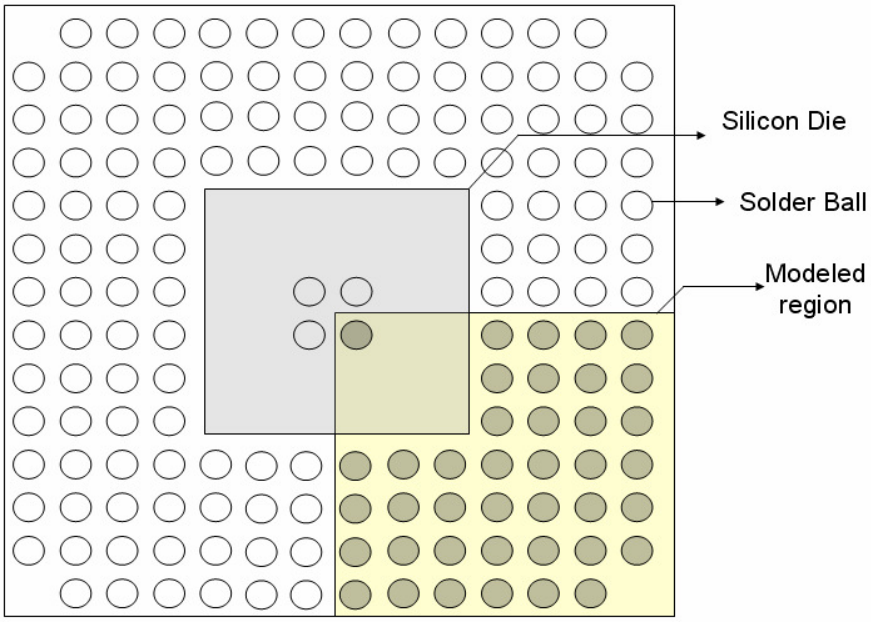

Figure 7.18. Ball array matrix for PBGA 160 with showing the modeled part

5983			7100	8294	9217	9080
			7207	8311	9193	9072
			7614	8321	9103	9059
7347	7402	7711	8115	8247	8914	9093
8401	8400	8371	8248	8148	8884	9444
9143	9101	8979	8777	8792	9842	9437
8948	8909	8842	8837	9187	8334	

Figure 7.19. Fatigue life estimation using accumulated inelastic work

12964			7644	7884	9309	10313
			7411	7732	9244	10300
			7236	7537	9144	10299
7895	7588	7304	7230	7453	9124	10453
7902	7741	7530	7434	7736	9609	11302
9164	9090	8976	8954	9482	12211	12392
10143	10101	10052	10184	11084	10924	

Figure 7.20. Fatigue life estimation using accumulated inelastic strain

12413			7756	8029	9114	9633
			7568	7909	9059	9616
			7447	7758	8976	9603
7963	7716	7506	7491	7698	8958	9700
8052	7924	7757	7685	7933	9309	10274
9005	8942	8848	8828	9214	10992	10949
9504	9465	9418	9500	10107	9989	

Figure 7.21. Fatigue life estimation using accumulated total strain

A comparison of the mean life to failure of the package and the mean life to failure of the critical solder joint as determined above using the three damage metrics is shown in Table 7.9. As can be seen from the Table, using the critical solder joint alone to predict the life of the entire package leads to large over prediction of the fatigue life. This is because the life of the package from experiments is obtained by measuring the daisy chain resistances of all the solder balls together. Failure of the package is said to occur whenever the daisy chain resistance goes to infinity. The effect of taking multiple solder joints into account to estimate the fatigue life will be discussed in the following section.

Table 7.9. Comparison between mean life to package failure from experiments and mean life to failure of critical solder joint

N_{joint} (50%)	Cycles
Experiment (package life)	4649
Model (ΔW_{acc})	5983
Model ($\Delta \varepsilon_{acc}^{in}$)	7230
Model ($\Delta \varepsilon_{acc}^{tot}$)	7447

7.9. Model Validation from Probability of Failure for All Solder Joints

Recent studies by Modi et al [22] have shown that for a PBGA package with lead free solder, the critical solder joint might not always be first solder joint to fail. They have shown using experimental analysis using dye-n-pry technique that any solder joint in the whole of the package could fail first and the solder joints which often fail first are the ones located near the neighborhood of the critical solder joint. From this study we can conclude that the damage metrics found from modeling can be used only to obtain the probability of failure of a solder joint. Solder joints close to the critical solder joint tend to have a high value of damage metric and therefore tend to fail first.

Each solder joint can be described to have its own Weibull failure plot similar to the one for whole package as shown in Figure 7.1. The failure of the package is determined by measuring the daisy chain resistance of all the solder balls connected together. The reliability of the package should therefore be estimated by taking the reliability of all the solder joints into consideration. If n is the number of solder joints in the package, R_j the reliability of the solder joint, the reliability of the package, R_c, is given by Equation 7.10 [18, 70].

$$R_c = \prod_{i=1}^{n} R_j \qquad 7.10$$

If N_{ff} is the failure free life of the package, β is the shape factor of the Weibull distribution for the package, α is the characteristic life of the package, the reliability of the solder joint R_j after the package has gone through N thermal cycles is given by Equation 7.11[73].

$$R_j = 1 \quad for\ N < N_{ff}$$
$$R_j = \exp\left[-\left(\frac{N - N_{ff}}{\alpha - N_{ff}} \right)^{\beta} \right] \quad for\ N > N_{ff} \qquad 7.11$$

A three parameter Weibull distribution has been assumed as this was found to be better in fitting a large database of failure statistics compared to two parameter Weibull or lognormal distribution [70, 76]. The failure free life can be computed using Equation 7.9.

A plot of the reliability of the critical solder joint as determined from Equation 7.11 and the reliability of the whole package as determined from Equation 7.10 as a

function of number of thermal cycles is shown in Figure 7.22. The reliability function for the plot was determined by using accumulated inelastic work as damage metric.

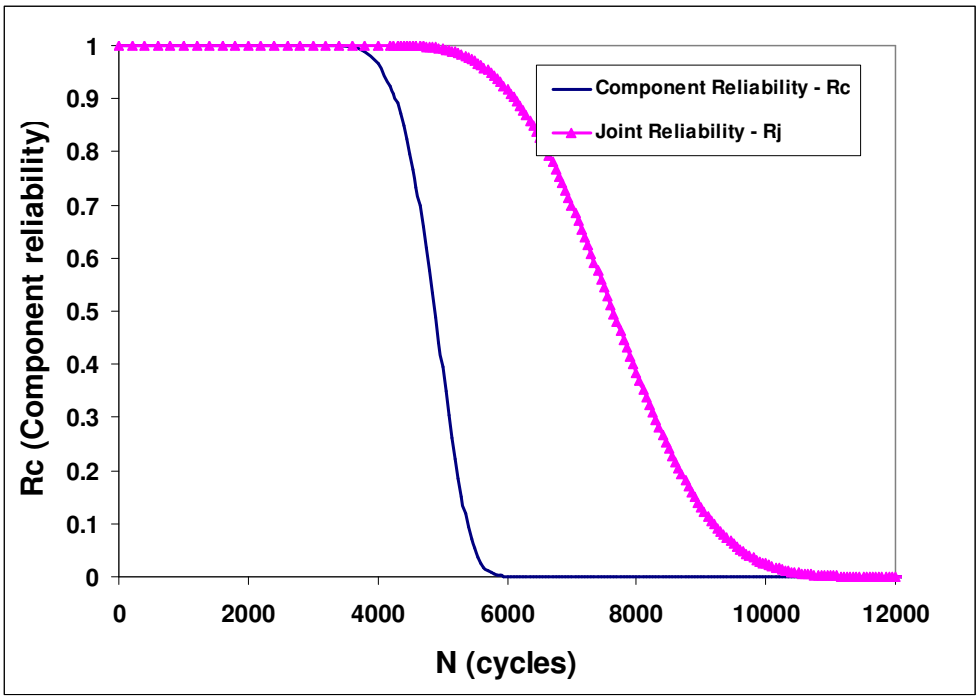

Figure 7.22. Reliability of the critical solder joint vs. reliability of the whole package

The component reliability is seen to be much lower when compared to the reliability of the critical solder joint and is therefore expected to fail much earlier than the critical solder joint. The mean life to package failure can be determined by setting the component reliability value to 0.5. This corresponds to a mean life of 4887 cycles. The mean life of the package can similarly be predicted using other two damage metrics. A comparison between the mean life to package failure as seen during experimental ATC and as predicted by fatigue life equation is shown in Table 7.10. There is very good agreement between the mean lives to package failure as estimated from the developed predictive model and as seen in during ATC. Accumulated inelastic work and

accumulated inelastic strain give very close estimates compared to accumulated total strain. This is probably because, low cycle fatigue failure is known to be caused from plasticity and creep deformation and accumulated inelastic work and accumulated inelastic strain take plasticity and creep into account better than accumulated total strain.

Table 7.10. Comparison between mean life to package failure from experiments and from simulation

N_c(50%)	Cycles
Experiment (package life)	4649
Model (ΔW_{acc})	4887
Model ($\Delta \varepsilon^{in}_{acc}$)	5101
Model ($\Delta \varepsilon^{tot}_{acc}$)	5232

7.10. Summary on Predictive Model Development

A predictive model to estimate the fatigue life of solder joints in a PBGA package was developed. The model was developed by measuring the crack growth rate of solder joints under the die edge and under the package edge for two different PBGA packages and correlating the measured crack growth rate with results from finite element analysis. The normal strain in the solder joints in the out-of-plane direction and the number of solder joints in the package was also taken into consideration to estimate the fatigue life of a test PBGA package. The following conclusions were drawn from the study.

- The crack growth rate in the solder joints does not only depend on the commonly used damage metrics such as, accumulated strain or accumulated work, but also depends on the normal strain in the out-of-plane direction. A Compressive out-of-plane strain has an effect of decreasing the rate of crack growth in the package.

- The failure life of the critical solder joint was found to be significantly higher than the failure life of the whole package as determined from experimental ATC. Equating the fatigue life of the whole package to the fatigue life of the single critical solder joint, as has been traditionally done, could be misleading.
- The reliability of each and every solder joint in a package as a function of number of cycles was found by assuming the failure follows a Weibull reliability function. The reliability and the mean life of the whole package were determined from the reliability function of each solder joints. Good agreement was observed between the predicted fatigue life of the package and the fatigue life as determined by experimental ATC.

CHAPTER 8

FATIGUE LIFE PREDICTION USING LASER MOIRE INTERFEROMETRY

In the foregoing chapters, microstructure evolution, accelerated thermal cycling, field-use thermal excursions, and physics-based modeling of various PBGA packages with lead-free SAC alloys have been discussed. Performing either ATC or long term thermal excursion experiments is time consuming and could last for several months. If microstructure evolution study is performed in addition, it would take even more time to qualify BGA packages. Both thermal excursion experiments and microstructure evolution study can be performed only for one temperature regime. To extend it to multiple temperature regimes, the entire experimental suite should be repeated. Numerical simulations can assist in estimating the reliability for multiple temperature regimes in a short duration. However, numerical simulation results depend on the model geometry and the material models used. Laser moiré interferometry is an experimental technique and therefore does not make any material property assumptions. The reliability of the solder joint can be estimated in a matter of few days and the methodology can be easily extended to multiple temperature regimes.

In this chapter, a new methodology to estimate the fatigue life of solder joints using laser moiré interferometry will be discussed. The sample preparation and experimental setup used for the study will be described first. This will be followed by the

results from the in plane strain measurements made at various temperatures. The strains will be used to estimate the fatigue life of the solder joints. A comparison will be made between the fatigue lives as determined from laser moiré experiments and as seen during experimental ATC. The results from the in plane strain measurements at various temperatures will then be used to estimate the fatigue lives at multiple temperature regimes.

8.1. Sample Preparation

The PBGA 356 package with lead-free SAC405 alloy solder interconnects was used for the laser interferometry studies. The package construction has been outlined in Chapter 6. The footprint of PBGA 356 package is shown in Figure 7.6. The solder interconnects had a pitch of 1.27 mm. The average standoff height of the solder interconnects was 0.52 mm. The PBGA package was assembled on a 1.5 mm thick FR4 board. The package assembly had eighteen rows of solder balls. The assembly was cut at the center line of the package along a direction parallel to one of the sides of the square package so as to expose the ninth row of solder joints. The cut assembly was ground and polished on a 1200 grit silicon carbide grinding sheet to make sure that the cross-section is along the centerline of the ninth row. Solder joints exhibit hysteresis behavior when subjected to thermal cycling. To ensure that the results obtained from the laser moiré studies correspond to the stabilized response, the cut package was thermal cycled for ten cycles in a thermal chamber between -55°C and 125°C at 5°C/s ramp rate and 15 minutes dwell at both temperature extremes. Grating, with 1200 lines/mm was then applied on the ground sample at room temperature. A grating with line spacing of 1200 lines/mm gives a sensitivity of 417 nm/fringe order. An epoxy material was used to adhere the

grating to the sample. The drag method described by Post [49] was used to ensure that a thin layer of epoxy was spread on the grating surface. The cut sample was then placed on the epoxy and the epoxy material was allowed to cure for 48 hours to ensure that the grating adheres well to the polished sample. The cross-section of the cut sample before and after applying the grating is shown in Figure 8.1a and Figure 8.1b respectively. Two such packages were used for the analysis. Since the PBGA 356 package had symmetry, two packages provided two pairs of similar solder joints for deformation and strain measurements.

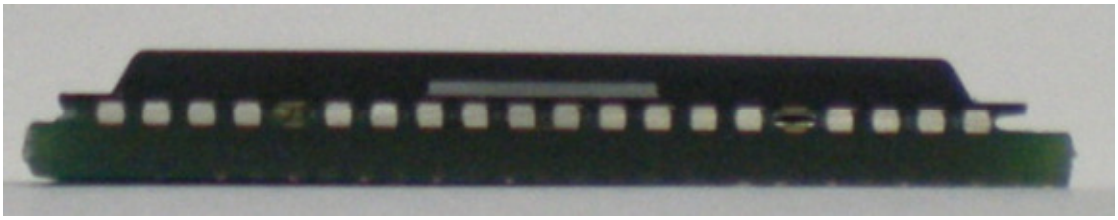

(a)

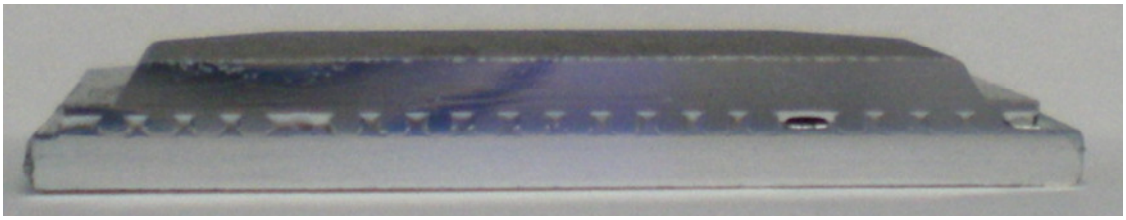

(b)

Figure 8.1. a)Cross-sectioned sample before grating application b)Cross-sectioned sample after grating application

8.2. Experimental Setup

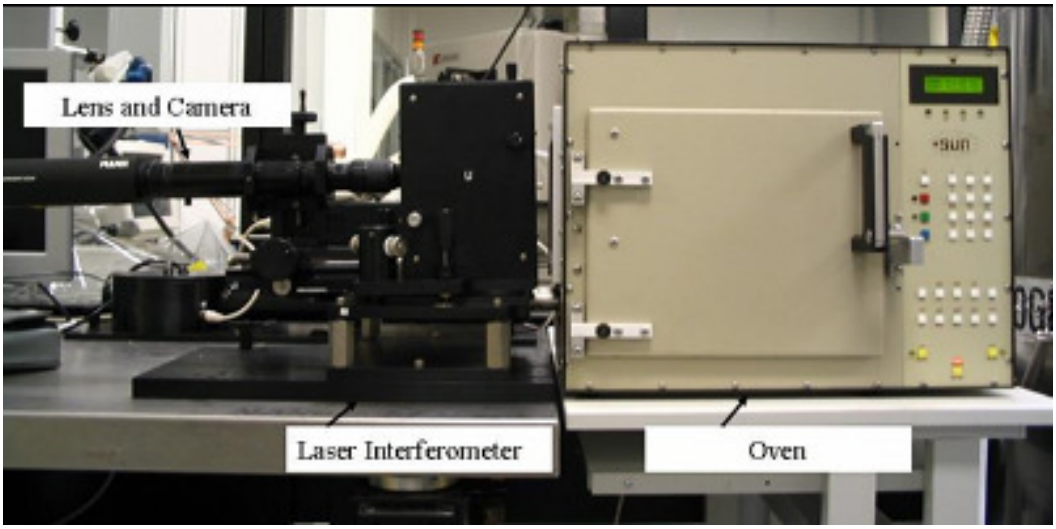

Figure 8.2. Moiré interferometry experimental setup

The laser moiré equipment from Photomechanics® was used for this study. The experimental setup is shown in Figure 8.2. The specimen with the moiré grating is placed on a holder that is attached directly to the moiré interferometer through a connecting rod. This arrangement ensures that the specimen moves along with the interferometer and thus ensuring that there is no relative movement of the specimen with respect to the interferometer. The specimen and the holder are then placed inside the thermal chamber maintained at atmospheric pressure. Before performing the experiment, the equipment needs to be calibrated for null fringes. This involves adjusting the incident angle α of the laser source for both the U and V field laser sources so that the reflected light is of -1 order i.e. it is perfectly normal to the surface. After calibration, the number of observed fringes is close to zero. The chamber has built-in heating coils which can be used to heat the chamber at a user specified heating rate to a temperature of up to 150°C. The chamber also has inlet valves through which liquid nitrogen can be passed to cool the chamber to

as low as -60°C. The deformation fringes on the grating observed due to temperature excursion can be captured in-situ using a lens and a CCD camera.

8.2.1. Temperature Loading Condition

The moiré grating was applied at room temperature. This makes the room temperature the stress-free temperature for the analysis. The temperature loading therefore starts at room temperature. The loading profile used for the study is shown in Figure 8.3. The chamber was cooled from room temperature to 0°C and then cooled down further to -55°C. The chamber was then heated to 65°C, 100°C and 125°C in that order. The cooling and heating rate was maintained at 5°C/min. Thermocouples were used to monitor the temperature of the sample. A 15 minutes dwell at each temperature was found to be sufficient for the sample to reach within 1°C of the set chamber temperature. At each temperature, the chamber was therefore held for 15 minutes.

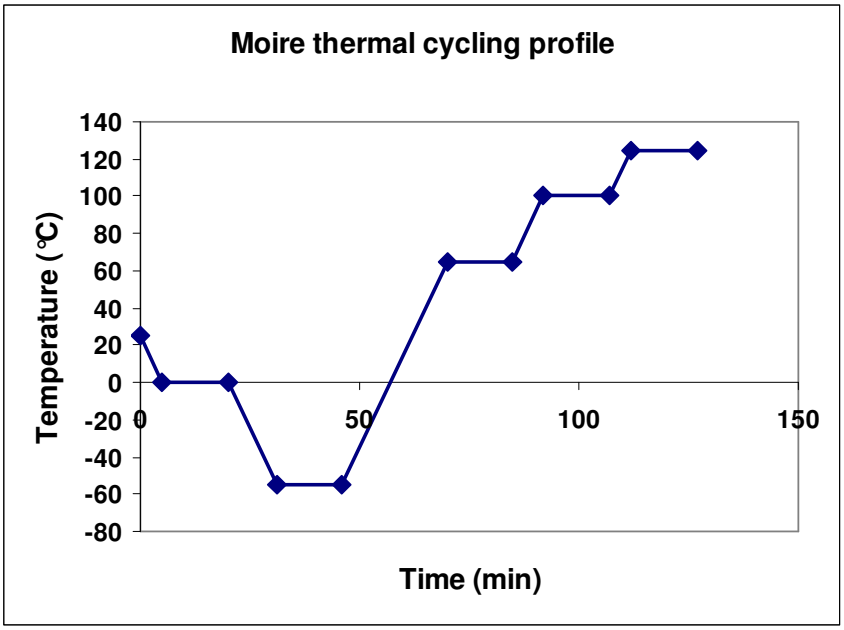

Figure 8.3. Loading profile used for the study

8.3. Variation of In-plane Strain Components with Temperature

The null field fringe pattern after calibration at room temperature was captured before the start of the thermal cycling. The *U* and *V* field null field fringe pattern is shown in Figure 8.4. The number of fringes in the *U* and *V* field is seen to be close to zero. This indicates successful grating application and calibration. After capturing the null field fringes, the *U* and *V* field deformation fringes were captured at the end of the 15 minutes dwell at each temperature level. The captured images are shown in Figure 8.5 through Figure 8.9. As the package possessed symmetry, only the right half of the package has been shown in the images. The solder joints underneath the die edge are shown in a magnified image beside for clarity.

U field – Null fringes

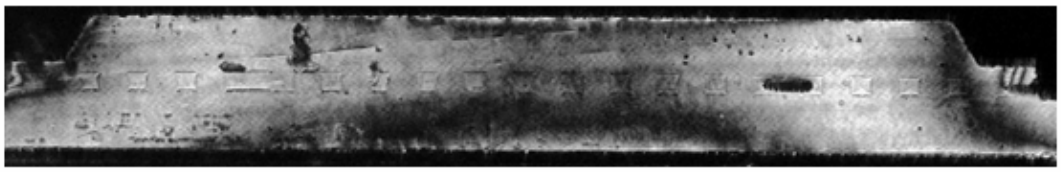

V field - Null fringes

Figure 8.4. *U* and *V* field null fringe pattern at room temperature

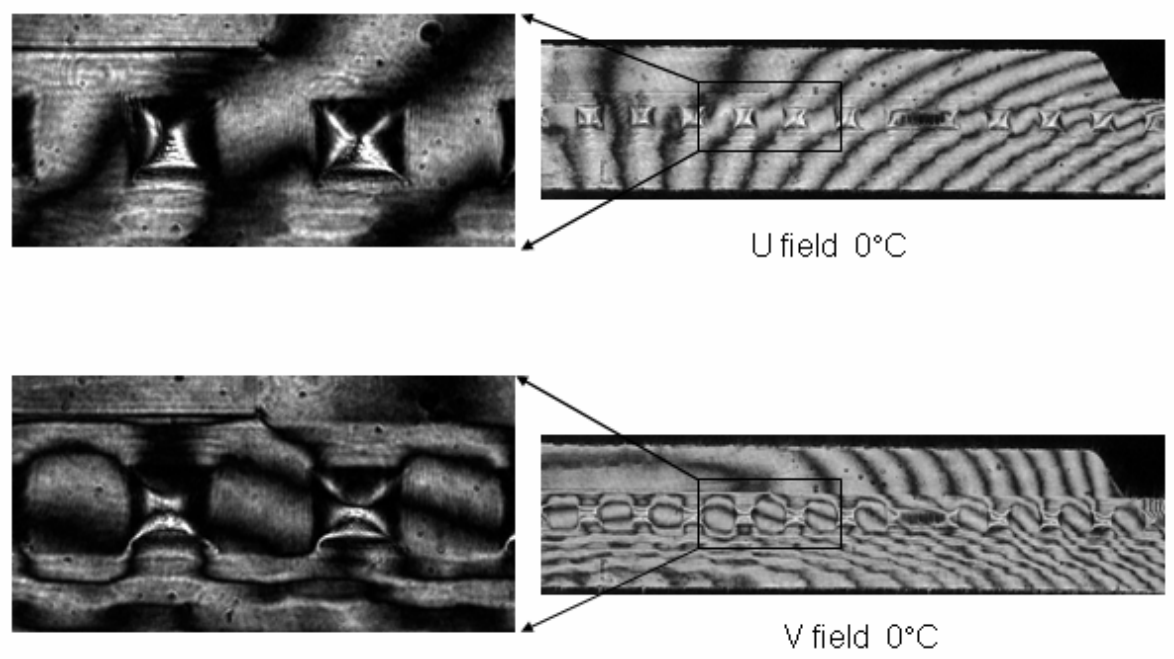

Figure 8.5. *U* and *V* field deformation fringe pattern at 0°C

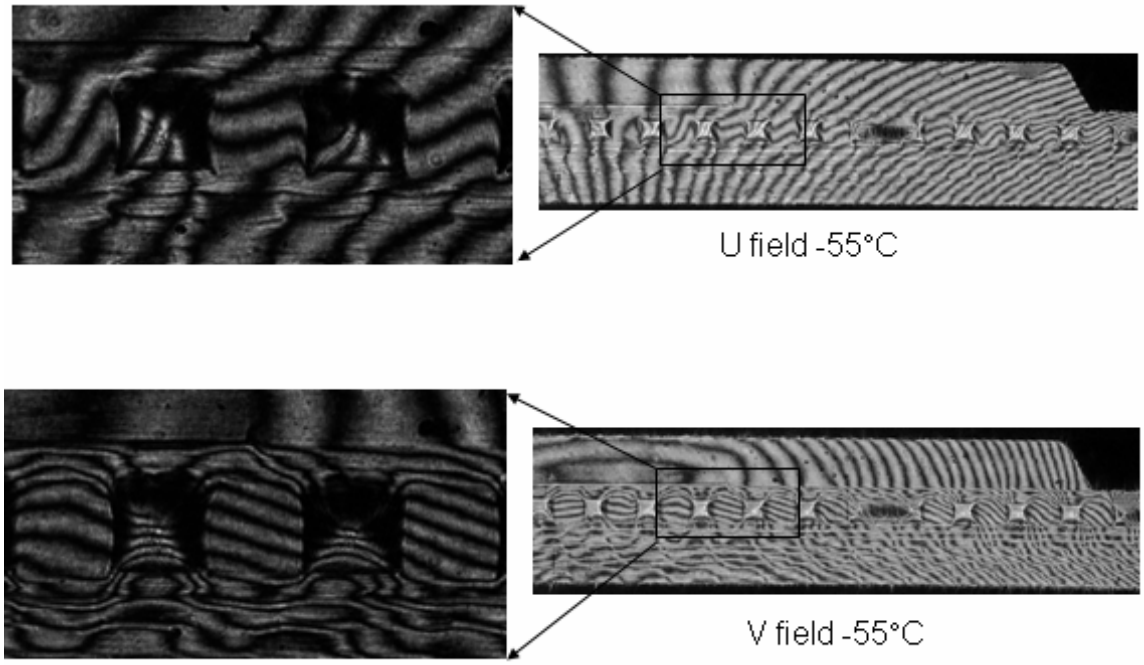

Figure 8.6. *U* and *V* field deformation fringe pattern at -55°C

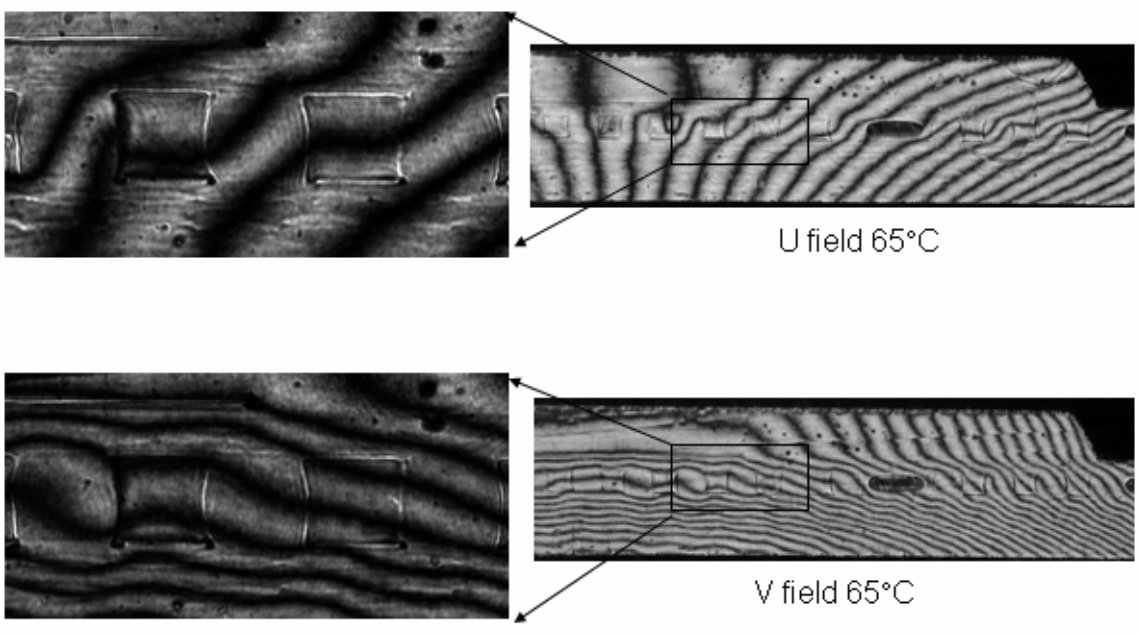

Figure 8.7. *U* and *V* field deformation fringe pattern at 65°C

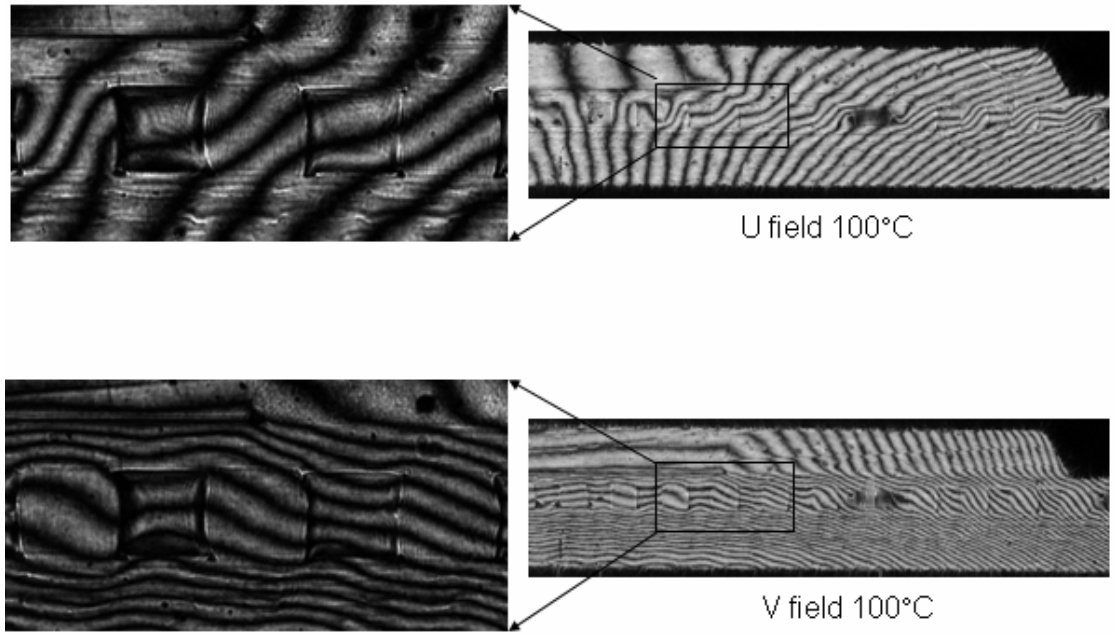

Figure 8.8. *U* and *V* field deformation fringe pattern at 100°C

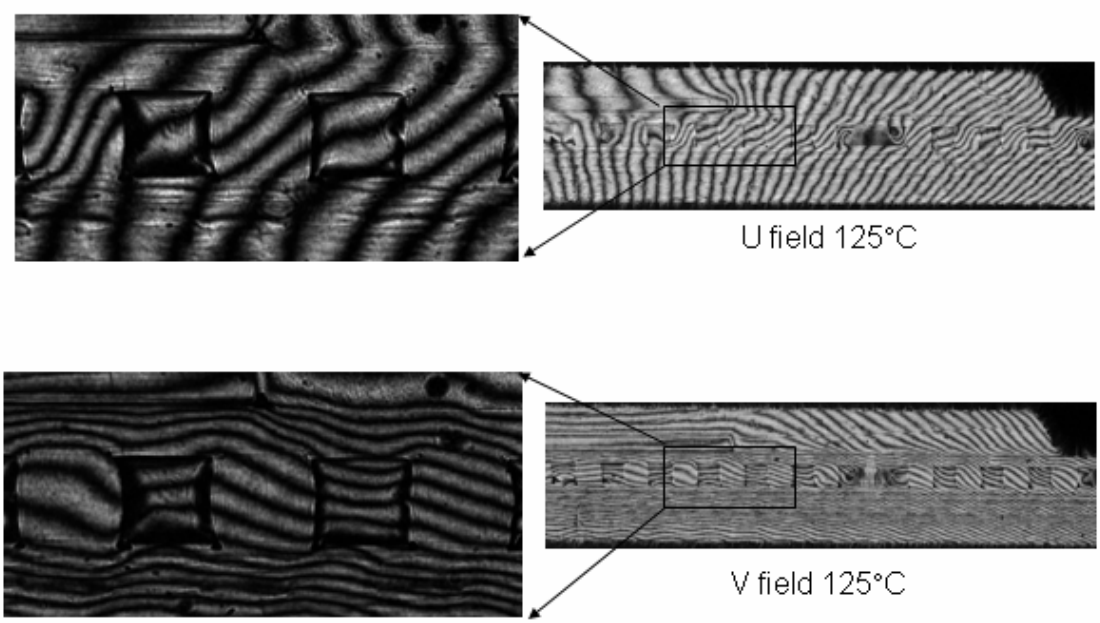

Figure 8.9. *U* and *V* field deformation fringe pattern at 125°C

Before proceeding with determining the strains in the solder joint, the critical solder joint needs to be determined. A solder joint which experiences highest shear strain can be expected to fail first and hence is likely to be the critical solder joint. The average shear strain in the whole solder ball was used as a metric to determine the critical solder ball. The *U*-field and *V*-field deformation patterns, for solder joints close to the die edge, at 125°C are shown in Figure 8.10 and Figure 8.11. The average shear strain for the three solder balls were computed using Equation 2.22 and are given in Table 8.1. The stand off height and the width of the solder joints were 0.52mm. The ΔN_x for the *V*-field was measured at the package-solder interface and the ΔN_y for the *U*-field was measured for the entire stand-off height of the solder joint. As can be seen from Table 8.1, the solder joint under the die has the highest shear strain and was therefore chosen for strain computation and fatigue life estimation.

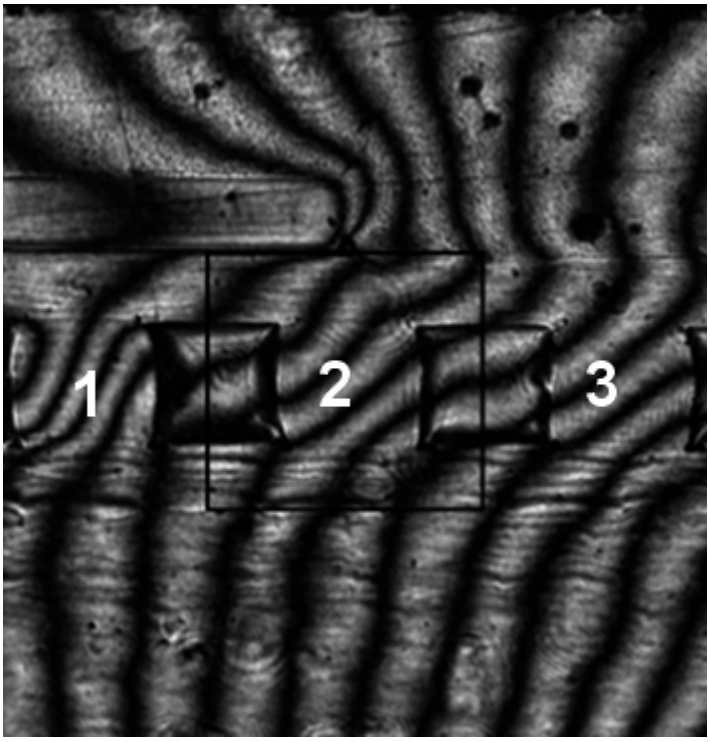

Figure 8.10. *U* field deformation fringe pattern at 125°C

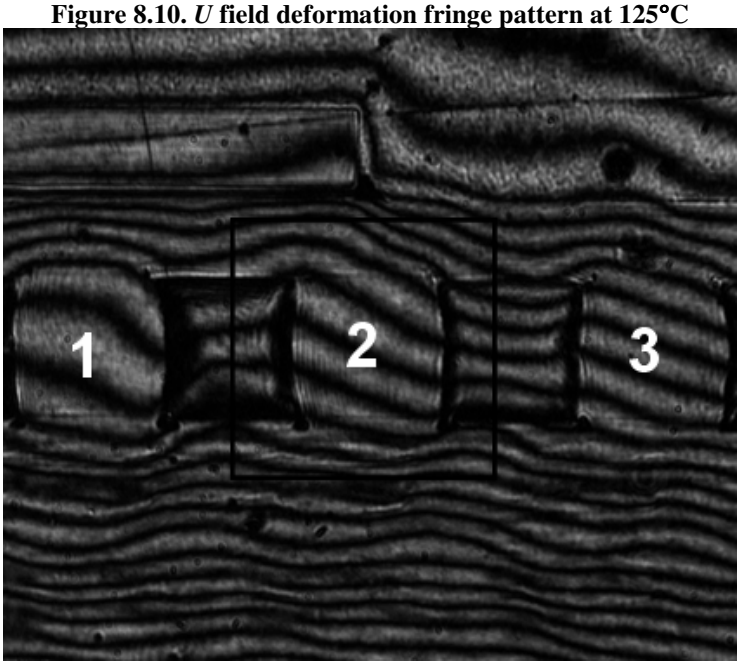

Figure 8.11. *V* field deformation fringe pattern at 125°C

Table 8.1. Average shear strain in the solder joints underneath the die at 125°C

Solder Joint Number	ΔN_x(V-field)	ΔN_y(U-field)	Average Shear Strain
1	1	2	0.001203
2	1.5	2.5	0.001604
3	1	2.5	0.001403

Solder joint cracking from thermal cycling was seen to occur mostly at the package side of the solder joint. Fatigue life should therefore be computed by computing the average strains from as small a region as possible near the package side of the solder joint. The density of fringes from Figure 8.10 is sparse and is not sufficient to make an accurate strain computation in a small region near the package-solder interface. Phase shifting method, as explained in Chapter 2, was therefore used to increase the density of fringes by a factor of four to 104 nm per fringe order. The four phase shifted fringe pattern images for the *U* field fringes at 125°C are shown in Figure 8.12.

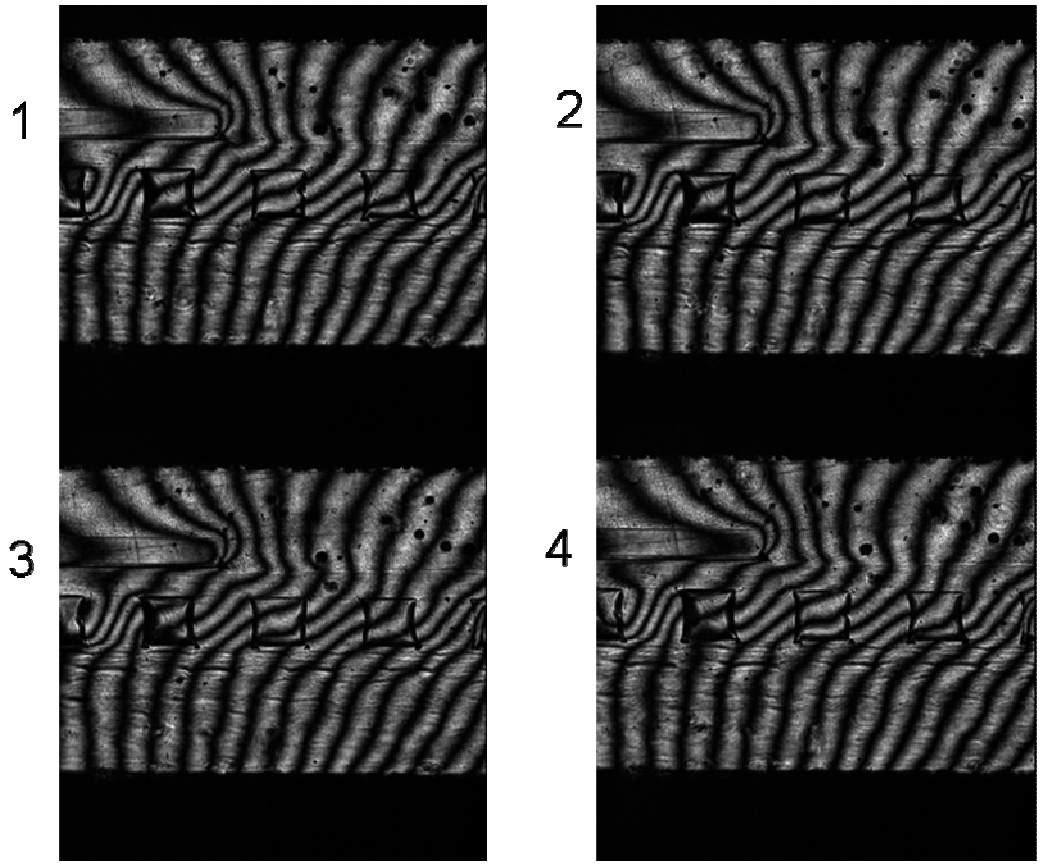

Figure 8.12. Phase shifted U field fringes at 125°C

The O/DFM method described in Chapter 2 was used to increase the fringe counting accuracy by fourfold. The algorithm used to increase the fringe counting accuracy is given in Appendix A. The resulting fringe pattern after implementing the phase shifting method is shown Figure 8.13. Average strains in a 150μm x 125 μm (width x height) region near the package side corners can be conveniently measured. The O/DFM technique was implemented for both the *U* and *V* field images at all the temperatures.

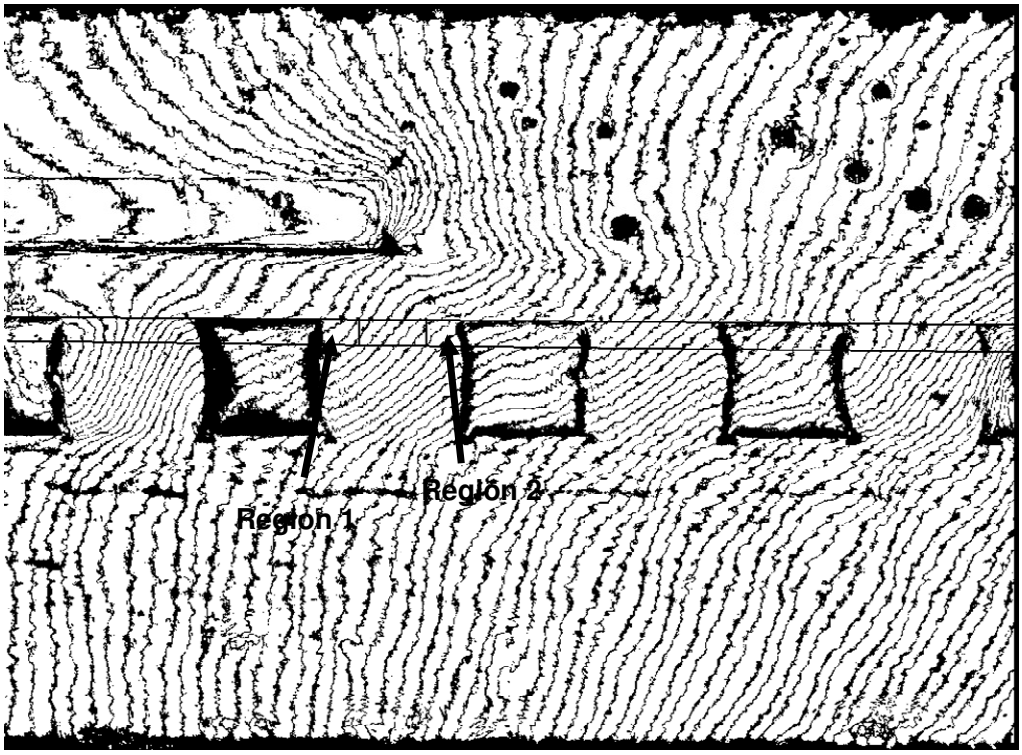

Figure 8.13. Fringe pattern for the U field fringes at 125°C after implementing O/DFM method

8.4. Computation of In-plane Strains from Laser Moiré Contours

The strains computed from the deformation fringes obtained by moiré interferometry at a given temperature consists of both thermal strains and mechanical strains [77] as shown in Equation 8.1 through Equation 8.3. Thermal strains are induced by normal expansion or contraction of the solder material and mechanical strains are induced due to CTE mismatch between the package and the board material. It should be noted that the thermal strains change only the normal strain component and not the shear strain component.

$$\varepsilon_{xx} = \varepsilon_{xx}^{mech} + \varepsilon_{th} \qquad 8.1$$

$$\varepsilon_{yy} = \varepsilon_{yy}^{mech} + \varepsilon_{th} \tag{8.2}$$

$$\varepsilon_{xy} = \varepsilon_{xy}^{mech} \tag{8.3}$$

where ε_{th} is the thermal strain at the temperature at which strain measurements were made. It is therefore necessary to subtract the thermal strains from the measured strains to obtain the mechanical strains. The mechanical strains can then be used for fatigue life estimation. For a given temperature differential, ΔT, the above equations can be rearranged as follows:

$$\Delta\varepsilon_{xx}^{mech} = \Delta\varepsilon_{xx} - \Delta\varepsilon_{th} \tag{8.4}$$

$$\Delta\varepsilon_{yy}^{mech} = \Delta\varepsilon_{yy} - \Delta\varepsilon_{th} \tag{8.5}$$

$$\Delta\varepsilon_{xy}^{mech} = \Delta\varepsilon_{xy} \tag{8.6}$$

The thermal strain range in the x and y direction can be computed from Equation 8.7.

$$\Delta\varepsilon_{th} = \alpha_{th}\Delta T \tag{8.7}$$

where α_{th} is the CTE of the solder material and ΔT is the temperature change experienced by the package. An average CTE of 24 ppm/°C was used for computing the thermal strain in the solder joint.

The in-plane strains were computed by manually counting the fringes at both the corners of the solder joint under the die edge. Equations 2.20 through 2.22 were used to compute the total strains and Equations 8.1 through 8.3 were used to evaluate the

mechanical strains from the computed total strains. Measurements were made for both the symmetrical solder joints in both the packages. Each measurement at a given temperature therefore corresponds to eight data points. Since the grating was applied at room temperature, the in-plane strains at room temperature are zero. The in-plane mechanical strains along with the standard deviation as a function of temperature is listed in Table 8.2 and plotted through Figure 8.14 through Figure 8.16. As we move away from room temperature, as expected, the strains are seen to increase.

Table 8.2. In-plane mechanical strains in the solder joint under the die as function of temperature

Temperature (°C)	Mean ε_{xx}	Std dev ε_{xx}	Mean ε_{yy}	Std dev ε_{yy}	Mean ε_{xy}	Std dev ε_{xy}
-55	0.001587	0.000307	-0.001155	0.000495	0.001371	0.000430
0	0.000372	0.000152	-0.000495	0.000289	0.000426	0.000261
25	0	0	0	0	0	0
65	-0.000482	0.000207	0.000172	0.000203	-0.000562	0.000378
100	-0.001278	0.000570	0.000225	0.000287	-0.001082	0.000645
125	-0.001736	0.000428	0.000340	0.000407	-0.001177	0.000528

A plot showing the variation of normal mechanical strain in the horizontal direction (ε_{xx}) with temperature is given in Figure 8.14. Solder joint material has a CTE higher than the CTE of the package substrate. At temperatures lower than room temperature, the solder joint material has a tendency to contract more than the substrate. This leads to the development of tensile strain in the solder joint from the package substrate trying to expand the solder joint. The opposite trend occurs at temperatures higher than the room temperature and leads to the development of compressive strains in the solder joint. As discussed before, tin is an anisotropic material. Depending on the orientation of the tin grain at the package-solder interface, substantial differences in the CTE between the solder joint and the package substrate can be seen. The difference in the

CTE between the solder joint and the package substrate results in deviation in the measured strain which increases with temperature difference from room temperature.

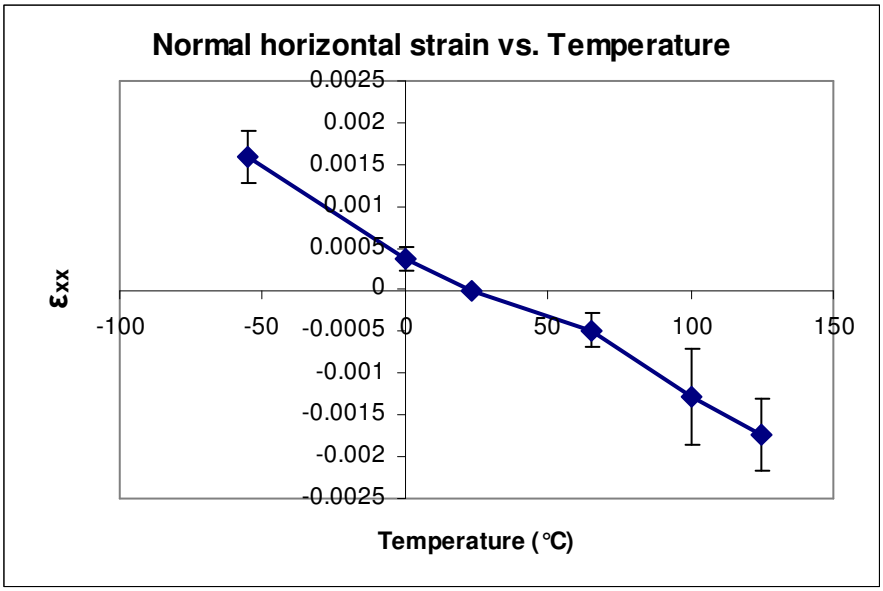

Figure 8.14. Variation of normal strain in the horizontal direction with temperature

The variation of the normal mechanical strain in the vertical direction (ε_{yy}) with temperature is shown in Figure 8.15. The PCB has a higher CTE when compared to the average CTE of the package. At lower temperatures, therefore, the PCB contracts more than the package making the whole assembly warp downwards. This leads to compressive strains in the solder ball under the die edge. Similarly, at temperatures higher than the room temperature, the whole assembly warps upwards making the strains in the solder joints tensile in nature.

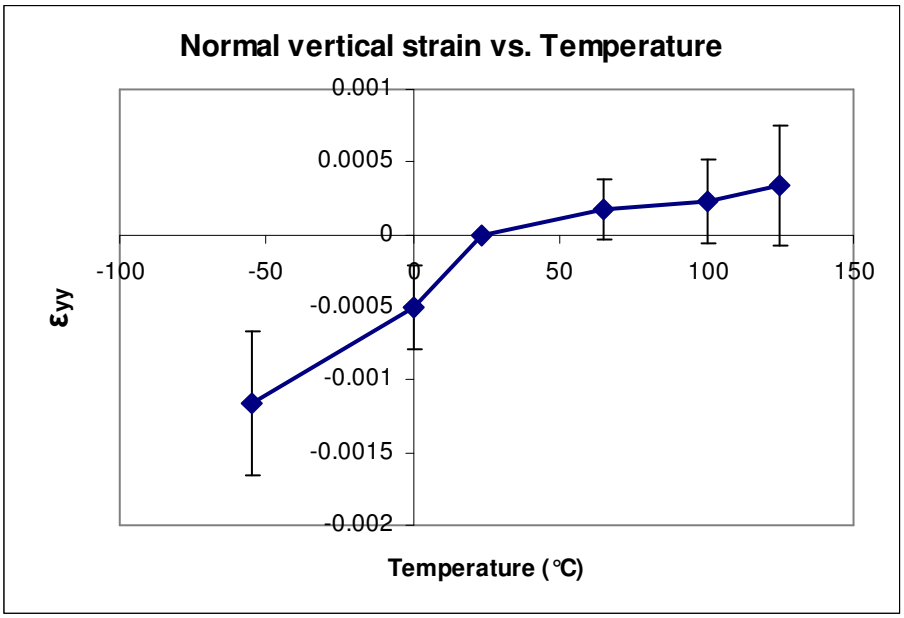

Figure 8.15. Variation of normal strain in the vertical direction with temperature

It can be seen from Figure 8.15 that the rate of increase of normal strains is higher for temperatures lower than room temperature. At higher temperatures, the solder, the package and the board material tends to soften. Decreased modulus of the solder material implies less coupling between the package and the PCB which leads to lower rate of change of warpage and hence lower rate of change of normal strain in the vertical direction.

The variation of in-plane shear strain (ε_{xy}) with temperature is shown in Figure 8.16. The sign of the shear strain was chosen arbitrarily. The sign of the shear strain will have no effect on the strain range and the fatigue life evaluation to be made in the following section. The variation of the shear strain with temperature is almost linear.

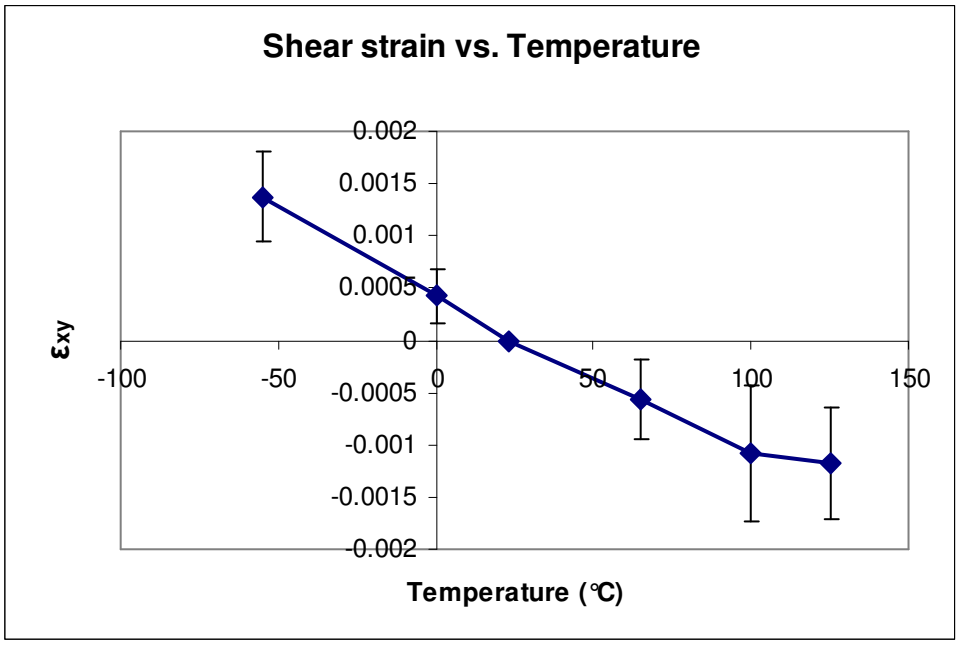

Figure 8.16. Variation of shear strain with temperature

8.5. Fatigue Life Estimation

The solder joint experiences complex multi-axial loading. To estimate the fatigue life, the strain accumulated in one thermal cycle and the mean normal strain in the vertical direction needs to be determined. These quantities can be used with the developed Equations 7.6 through 7.8 to estimate the mean life to package failure. For the present study, a complete thermal cycling loading profile was not used. The accumulated strain was determined for only one half of the cycle between -55°C and 125°C. The total accumulated strain per cycle was obtained by multiplying this value by a factor of two. If $\Delta\varepsilon_{xy}^{mech}$, $\Delta\varepsilon_{xx}^{mech}$ and $\Delta\varepsilon_{yy}^{mech}$ are the algebraic differences in the strain components between any two successive temperatures, the accumulated strain between those two temperatures, $\Delta\varepsilon_{acc,}$ is obtained from the component strain differences as shown in Equation 8.8. The accumulated strain for one half of the thermal cycle was found by adding the

accumulated strains between -55°C and 65°C, between 65°C and 100°C and between 100°C and 125°C.

$$\Delta\varepsilon_{acc} = \frac{\sqrt{2}}{3}\left[(\Delta\varepsilon_{xx}^{mech} - \Delta\varepsilon_{yy}^{mech})^2 + \Delta\varepsilon_{xx}^{mech\,2} + \Delta\varepsilon_{yy}^{mech\,2} + 6\Delta\varepsilon_{xy}^{mech\,2}\right]^{1/2} \qquad 8.8$$

The mean normal strain in the vertical direction was evaluated by measuring the normal strains between -55°C and 125°C and taking the average of the two. The measured accumulated strain for one thermal cycle, the mean normal strain in the solder joint and the fatigue life are given in Table 8.3. The standard deviations for the values are also shown in the table.

Table 8.3. Fatigue life parameters for a solder joint from laser moiré interferometry

	Mean	**Standard deviation**
Accumulated strain per cycle	0.009396	0.001140
Mean normal strain	-0.000448	0.000318
Fatigue life of solder joint	5024 cycles	1290 cycles

The fatigue life of the PBGA 356 package was also found from experimental ATC as shown in Figure 7.3. The mean life to failure ($N_{50\%}$) of the package was 4777 cycles. The mean life of the solder joint as computed from laser moiré interferometry needs to be translated in some way to the mean life of the whole package to compare it with the results from experimental ATC. Unlike finite element method, laser moiré interferometry does not allow evaluation of reliability for all the solder joints in a package. Computing the reliability of the package by multiplying the reliability of all the solder joints, as was done in Chapter 6, therefore cannot be performed. An alternate method has been proposed by Darveaux [18] where the failure of all the equally stressed critical joints are assumed to follow a Weibull distribution. The failure of package occurs when any one of the *q* critical solder joints fail. Based on this assumption, a de-rating

factor *f* can be evaluated as shown in Equation 8.9. The mean life of the whole package can then be estimated by multiplying the mean life of the solder joint with the de-rating factor.

$$f = \frac{1}{2}\left[1 + \left[-\ln\left(1 - \left(\frac{0.7}{q + 0.4}\right)\right)\right]^{\frac{1}{\beta_w}}\right] \qquad 8.9$$

A PBGA 356 package has eight symmetrical critical solder joints. Using this number, the de-rating factor and hence the mean life to fatigue failure of the package was evaluated. A comparison between the mean life of the package as determined from laser moiré interferometry and experimental ATC is shown in Table 8.4.

Table 8.4. Mean life comparison between moiré interferometry and experimental ATC

	Moire interferometry	**Experimental ATC**
Mean life	4379	4639
Standard deviation	1136	-

Laser moiré under predicts the mean fatigue life of the package. Significant deviation in the measured fatigue life of the package can also be seen. The under prediction of the mean life occurs from different averaging technique used to develop the predictive model for the solder joint. As was described in Chapter 6, the predictive model was developed by volume averaging the damage metrics along a circular annular region at the package side solder interface. The strains from laser moiré interferometry, however, were averaged in an area located at the solder joint fillet region where stress and strain concentrations are bound to be present. A cut-model for PBGA 356 package was therefore simulated. Similar to the laser moiré sample, the cut-model had only half of the ninth row of solder balls modeled. A contour plot of accumulated inelastic work in one cycle for the solder joint under the die edge is shown in Figure 8.17. It can be seen that

the maximum accumulated work is higher than what was observed for the uncut specimen as shown in Figure 6.15. This is due the presence of stress and strain concentration. The stress and strain concentration is located on the free surface where the measurement is made. This leads to higher strain measurement and consequently leads to lower fatigue life prediction using laser moiré interferometry.

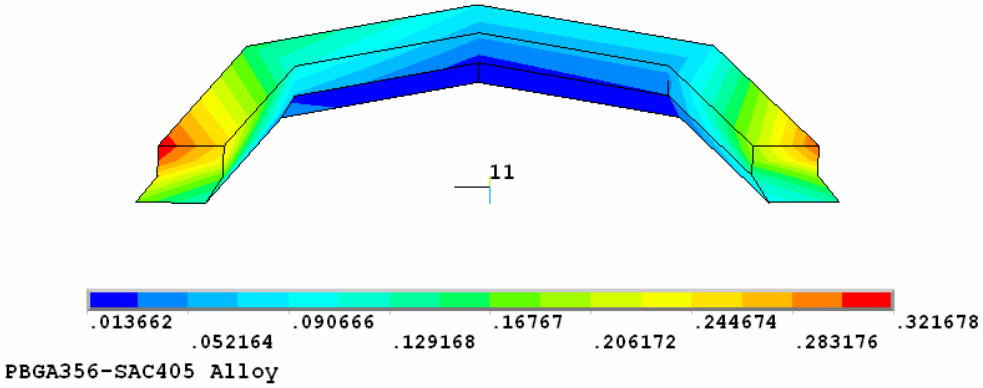

Figure 8.17. Variation of shear strain with temperature

8.6. Fatigue Life Estimation for Multiple Thermal Regimes

Laser moiré interferometry offers the flexibility to measure the strains at various temperatures. This allows evaluating the strain ranges and hence the fatigue life of the package when subjected to different thermal cycling loading conditions. Nine different thermal regimes were investigated for the study. The accumulated strains between these thermal regimes were computed using Equation 8.8. The accumulated strains per cycle, fatigue life of the solder joint and the fatigue life of the package for all nine thermal cycle regimes along with the standard deviation is shown in Table 8.5 and Table 8.6. The temperature regimes have been divided into two sets based on the harshness or mildness of the temperature cycling range.

Table 8.5. Fatigue life parameters for multiple thermal regimes – Harsh conditions

Range #	Temperature Range	Mean accumulated strain	Std deviation of accumulated strain	Mean solder joint fatigue life	Std deviation of solder joint fatigue life	Mean package fatigue life	Std deviation of package fatigue life
1	-55°C to 125°C	0.00938	0.00228	5191	1346	4379	1136
2	-55°C to 100°C	0.00782	0.00208	6670	2159	5627	1821
3	-55°C to 65°C	0.00612	0.00158	9082	2948	7662	2487
4	0°C to 125°C	0.00686	0.00224	8273	4316	6980	3641
5	0°C to 100°C	0.00462	0.00156	13433	7092	11332	5983

Ranges 1 to 5 have very high difference between high and low temperatures, exceeding 100°C, and can therefore be regarded as belonging to harsh thermal cycling conditions. Range #1 corresponds to JEDEC 22A104C-condition B [78] thermal cycling range and can be used to qualify packages used in military applications where the

temperature ranges seen are typically very high. Range #2 is a slightly milder version of Range #1 where the maximum temperature range is reduced from 125°C to 100°C. This condition is suitable for qualifying products used in automotive under hood applications. In Range #3, the maximum temperature is reduced even further to 65°C. This condition can be used in cases where the product does not experience high temperatures during field use and spends most of time at low temperatures. Ranges #4 and #5, which corresponds respectively to JEDEC 22A104C-condition J and K [78], can be used for qualifying products used in high power server or high performance desktop gaming applications. Products used in these systems are typically kept at room temperature. Including sub-zero temperatures in the thermal cycling range is therefore not necessary.

Table 8.6. Fatigue life parameters for multiple thermal regimes – Mild conditions

Range #	Temperature Range	Mean accumulated strain	Std deviation of accumulated strain	Mean solder joint fatigue life	Std deviation of solder joint fatigue life	Mean package fatigue life	Std deviation of package fatigue life
6	0°C to 65°C	0.00308	0.00114	22359	10479	18863	8840
7	25°C to 125°C	0.00382	0.00128	15952	6994	13457	5900
8	25°C to 100°C	0.00326	0.00128	24396	23543	20581	19861
9	25°C to 65°C	0.00172	0.00068	45901	28767	38723	24269

The temperature difference in the thermal cycling ranges 6 to 9 is 100°C or lower. These cycling ranges can therefore be regarded as mild. The ranges 7 and 8 are suitable for medium power computing applications or desktop applications. Ranges 6 and 9 are suitable for packages used in medical implant devices where the temperatures are required to be close to the body temperatures.

The comparison between the fatigue lives of the package for all combinations of low and high temperatures is also shown in a bar plot in Figure 8.18. As the temperature

difference between the high and low temperatures decreases, the mean life to fatigue failure is seen to increase drastically.

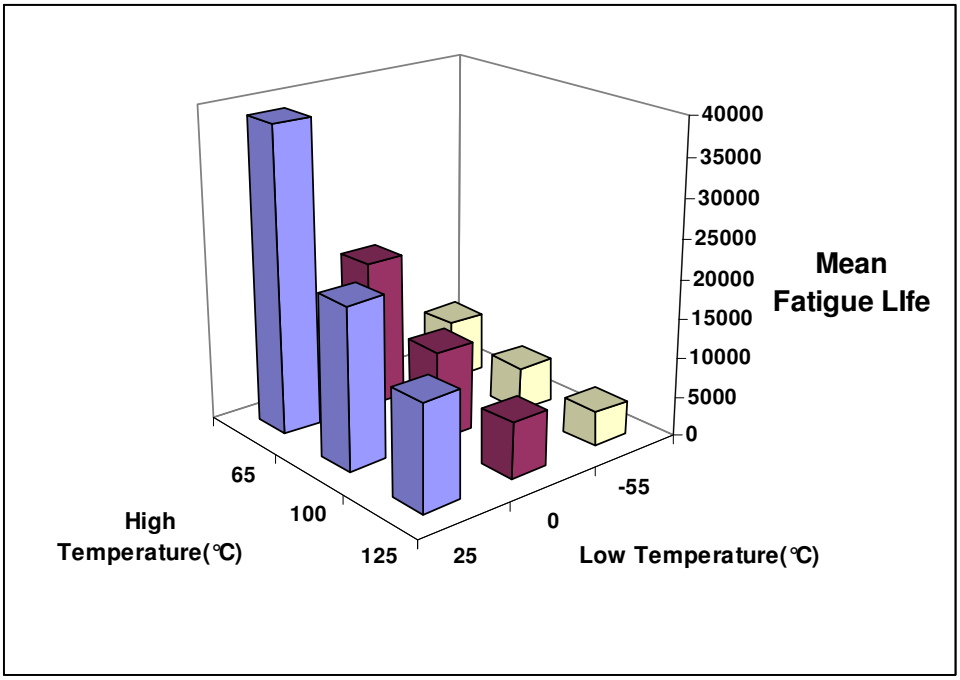

Figure 8.18. Package fatigue life for all combinations of low and high temperatures

Sn-Ag-Cu solders are known to exhibit very low deformation at low temperatures [15]. At low temperatures, the solder joint also tends to lose its ductility and becomes more brittle. The failure of the solder joint by low cycle fatigue is therefore reduced somewhat at lower temperatures. The variation in the mean life to failure of the package as a function of the high temperature seen during thermal cycling at various levels of low temperatures is shown in Figure 8.19. The mean life is seen to drop down more when the lower temperature is decreased from 25°C to 0°C than when the lower temperature is decreased from 0°C to -55°C. As seen from the graph, this difference is more evident at a high temperature of 125°C.

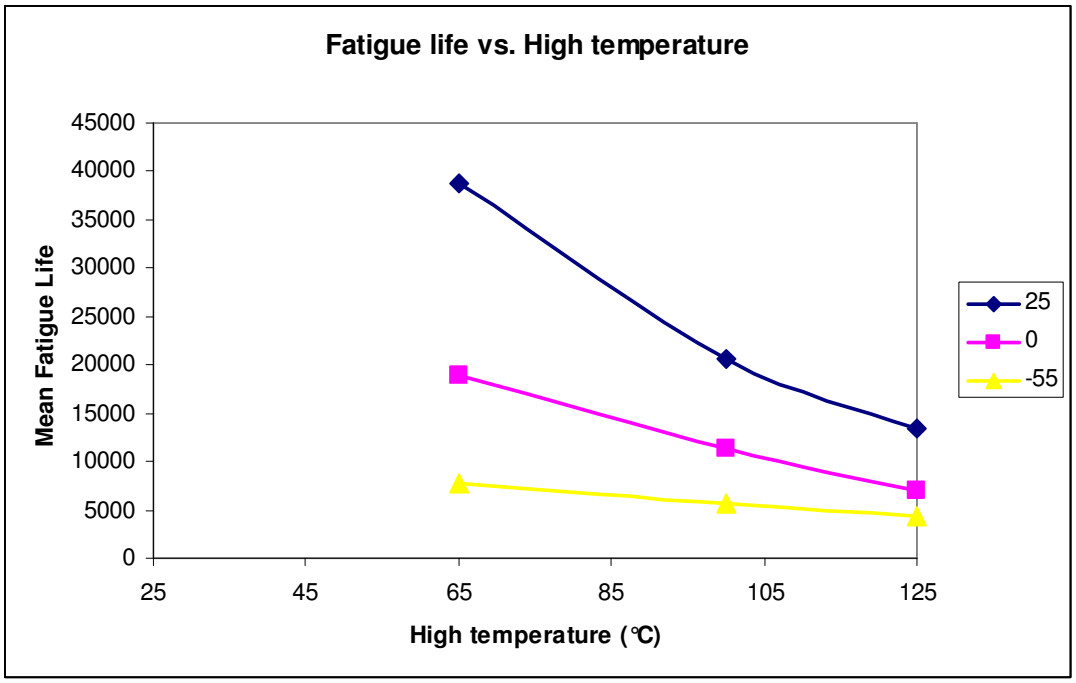

Figure 8.19. Effect of high temperature on fatigue life at various levels of low temperatures

8.7. Summary of Fatigue Life Prediction using Laser Moire Interferometry

In-plane strain measurements were made on cut PBGA 356 samples using laser moiré interferometry. Phase shifting combined with O/DFM method was used to increase the fringe counting accuracy to 104 nm per fringe order. The predictive model developed from finite element analysis and measured crack growth rate was used to estimate the fatigue life of the solder joints. A de-rating factor based on number of critical solder joints was used to translate the solder joint fatigue life to package fatigue life. The predicted life from laser moiré interferometry was compared with the fatigue life determined from experimental ATC. Laser moiré interferometry under predicted the life of the package. The under prediction was caused by the presence of strain concentration in the solder joint fillet regions and is unavoidable. The moiré interferometry study was

also extended so as to include multiple temperature regimes and fatigue life of the package was estimated for eight additional temperature ranges. The fatigue life was found to increase dramatically with a decrease in thermal cycling temperature range. It was also found that lower temperatures have less of an effect on the fatigue life of the solder joint than higher temperatures.

CHAPTER 9

CONTRIBUTIONS AND FUTURE WORK

9.1. Contributions

This research studied the reliability of Sn-Ag-Cu solder joints in PBGA packages using microstructure evolution, finite element method and laser moiré interferometry. The following are the unique contributions from this research.

- This is the first time a microstructure evolution based research has been conducted on lead free PBGA packages when subjected to extended periods of thermal excursions.
- The microstructure evolution based on particle coarsening was used to determine an acceleration factor between ATC and long term field-use conditions. The acceleration factor and hence the thermo-mechanical reliability of lead free packages for both ATC and field-use conditions can be determined in about the same time duration.
- A new predictive model to predict the fatigue life of SAC405 solder joints in PBGA packages has been developed. The predictive model was developed by taking the results from both experimental ATC and finite element analysis. In addition to the conventional damage metrics such as accumulated strain and accumulated work, the predictive model takes into consideration the state of

normal strain in the solder joint to determine the number of cycles for crack initiation and crack growth rate.

- Traditionally the life of the package has been determined by equating it to the life of the critical solder joint in a package. This assumption might not be applicable for PBGA packages. In this work, the effect of reliability of all the solder joints in a package was taken into consideration to determine the life of the package.

- A new method using laser moiré interferometry has been developed to estimate the fatigue life of solder joints in a matter of few days. The traditional way to determine the reliability was to use ATC which takes months to complete. The laser moiré interferometry technique can potentially be extended to include many temperature ranges in one experimental setup and can be used to determine the fatigue behavior of the solder joint as a function of thermal cycling temperature range.

9.2. Future Work

The following are the recommendations for possible future work in this area.

- Electron back scattered diffraction (EBSD) is another technique which can be used to characterize the microstructure evolution of Sn-Ag-Cu solder by measuring the change in the orientation of tin crystals at the solder-package interface. This method would be more fundamental as fatigue cracks develop in the tin material at the solder-package interface. Currently, there are not any known methods to suitably quantify, compare and develop an acceleration factor based on the change in tin crystal orientation with thermal cycling. It is also not

known if the change in tin crystal orientation is appreciable enough during field-use conditions to be able to quantify it adequately.

- The predictive model developed for this study was based only on PBGA packages. Including other types of packages, such as CBGA packages, CSPs and flip chip packages would increase the range of applicability of the fatigue predictive model.
- It is possible to develop a predictive model by using the results from experimental ATC and moiré interferometry for different types of packages with different sizes of solder joints. The developed model would be free from any possible assumptions inherent in finite element analysis.

APPENDIX A

MATLAB CODE FOR O/DFM IMPLEMENTATION

```
clear;
%The following program implements the O/DFM method
%to increase the fringe counting accuracy of the
%deformation fringes. Four images are required.
%The images should have a constant prefix followed
%by the index number of the image.
string='filename'; %The name of the constant prefix

file1=strcat(string,'1.bmp');
file2=strcat(string,'2.bmp');
file3=strcat(string,'3.bmp');
file4=strcat(string,'4.bmp');

A1=imread(file1);
A2=imread(file2);
A3=imread(file3);
A4=imread(file4);

A1=double(A1);
A2=double(A2);
A3=double(A3);
A4=double(A4);

len=size(A1);

%A1 and A3 have a phase difference of 180 degrees
B=abs(A1-A3);

for i=1:len(1)
   for j=1:len(2)
      %This value could be between 0 to 255.
      %Smaller the value, sharper the fringes.
      %Smaller values also gives faint fringes.
      %An optimal value should be chosen.
      if B(i,j)<=15
         C1(i,j)=0;
      else
         C1(i,j)=255;
      end
   end
end
```

```
%A2 and A4 have a phase difference of 180 degrees
B=abs(A2-A4);

for i=1:len(1)
   for j=1:len(2)
      if B(i,j)<=15
         C2(i,j)=0;
      else
         C2(i,j)=255;
      end
   end
end

C3=min(C1,C2);

%The final fringe pattern image file name
final=strcat(string,'_all.bmp');
imwrite(uint8(C3),final);
```

REFERENCES

[1] R. Tummala, E. J. Rymaszewski, and A. C. Klopfenstien, "Microelectronic Packaging Handbook - Semiconductor Packaging," Second ed. vol. 2: Chapman & Hill, 1997.

[2] G. Derman, "IC Attachments, Interconnects & Packaging," in *Electronic Engineering Times*, 1994, pp. 44-51.

[3] NCMS, "Lead-free Solder Final Report, www.ncms.org," 1997.

[4] NEMI, "National Electronics Manufacturing Initiative, News Release," in *www.nemi.org/PbFreePUBLIC/index.html*, 2007.

[5] JEIDA, "Challenges and Efforts Toward Commercialization of Lead-free Solder - Road Map 2000 for Commercialization of Lead-free Solder," *Japan Electronic Industry Development Association* 2000.

[6] M. Abtew and G. Selvaduray, "Lead-free Solders in Microelectronics," *Materials Science and Engineering,* vol. 27, pp. 95-141, 2000.

[7] R. Darveaux and K. Banerji, "Constitutive Relations for Tin-Based Solder Joints," *IEEE Transactions on Components, Packaging, and Manufacturing Technology,* vol. 15, pp. 1013-1024, 1992.

[8] A. LaLonde, D. Emelander, J. Jeannette, C. Larson, W. Rietz, D. Swenson, and D. W. Henderson, "Quantitative Metallography of β-Sn Dendrites in Sn3.8Ag0.7Cu Ball Grid Array Solder Balls via Electron Backscatter Diffraction and Polarized Light Microscopy," *Journal of Electronic Materials,* vol. 33, 2004.

[9] J. A. Rayne and B. S. Chandrasekhar, "Elastic Constants of β Tin from 4.2°K to 300°K " *Physical Review,* vol. 120, pp. 1658-1663, 1960.

[10] B. Chalmers, "Micro-Plasticity in Crystals of Tin " *Proceedings of the Royal Society of London, Series A, Mathematical and Physical Sciences,* vol. 156, pp. 427-443, 1936.

[11] D. Frear and H. Morgon, in *The Mechanics of Solder Alloy Interconnects*, J. H. Lau, Ed., 1994.

[12] S. Weise, E. Meusel, and K. J. Wolter, "Microstructural Dependence of Constitutive Properties of Eutectic and SnAg and SnAgCu Solder," in *Proceedings of 53rd Electronic Components and Technology Conference*, New Orleans, 2003, pp. 197-206.

[13] G. Z. Wang, Z. Cheng, N, K. Becker, and J. Wilde, "Applying Anand Model to Represent the Viscoplastic Deformation Behavior of Solder Alloys," *Journal of Electronic Packaging,* vol. 123, pp. 247-253, 2001.

[14] T. O. Reinikainen, P. Marjamaki, and J. K. Kivilahti, "Deformation Characteristics and Microstructural Evolution of SnAgCu Solder Joints," *6th. Int. Conf. on Thermal, Mechanical and Multiphysics Simulation and Experiments in Micro-Electronics and Micro-Systems, EuroSimE 2005,* pp. 91-98, Apr 2005 2005.

[15] S. Weise, A. Schubert, and H. Walter, "Constitutive Behavior of Lead-Free Solders vs. Lead-containing Solders - Experiments on Bulk Specimens and Flip-Chip Joints," in *Proceedings of 51st Electronics Components and Technology Conference*, Orlando, 2001, pp. 890-902.

[16] H. L. J. Pang, B. S. Xiong, and C. C. Neo, "Bulk Solder and Solder Joint Properties for Lead-Free 95.5Sn-3.8Ag-0.7Cu Solder Alloy," in *Proceedings of 53rd Electronic Components and Technology Conference*, New Orleans, 2003, pp. 673-679.

[17] A. Syed, "Accumulated Creep Strain and Energy Density Based Thermal Fatigue Life Prediction Models for SnAgCu Solder Joints," *Electronic Components and Technology Conference,* pp. 737-746, 2004.

[18] R. Darveaux, "Effect of Simulation Methodology on Solder Joint Crack Growth Correlation," in *Proceedings of 50th Electronic Components and Technology Conference*, Las Vegas, 2000, pp. 1048-1058.

[19] C. Han and B. Song, "Development of Life Prediction Model for Lead-free Solder at Chip Resistor," *8th Electronics Packaging Technology Conference,* pp. 781-786, 6-8 Dec, 2006 2006.

[20] H. L. J. Pang, B. S. Xiong, and T. H. Low, "Creep and Fatigue Characterization of Lead-Free 95.5Sn-3.8Ag-0.7Cu Solder," in *Proceedings of 54th Electronics Components and Technology Conference*, Las Vegas, 2004, pp. 1333-1337.

[21] F. X. Che and J. H. L. Pang, "Thermal Fatigue Reliability Analysis for PBGA with Sn-3.8Ag-0.7Cu Solder Joints," in *Electronics Packaging Technology Conference*, 2004, pp. 787-792.

[22] M. Modi, C. McCormick, and N. Armendariz, "New insights in critical solder joint location," *Electronic Components and Technology Conference,* vol. 1, pp. 977-982, May 31st - June 3rd 2005.

[23] E. A. Stout, N. R. Sottos, and A. F. Skipor, "Mechanical Characterization of Plastic Ball Grid Array Package Flexure Using Moire Interferometry," *IEEE Transactions on Advanced Packaging,* vol. 23, pp. 637-645, 2000.

[24] G. Wang, J. H. Zhao, M. Ding, and P. S. Ho, "Thermal Deformation Analysis on Flip-Chip Packages Using High Resolution Moire Interferometry," *Inter Society Conference on Thermal Phenomena,* pp. 869-875, 2002.

[25] J. Joo, K. Oh, S. Cho, and B. Han, "Thermo-mechanical and Flexural Behavior of WB-PBGA Package Using Moire Interferometry," *International Symposium on Electronic Materials and Packaging,* pp. 421-427, 2001.

[26] S. Cho, B. Han, and J. Joo, "Temperature Dependent Deformation Analysis of Ceramic Ball Grid Array Package Assembly Under Accelerated Thermal Cycling Condition," *Journal of Electronic Packaging,* vol. 126, pp. 41-47, 2004.

[27] C. Basaran, A. Cartwright, and Y. Zhao, "Experimental Damage Mechanics of Microelectronics Solder Joints under Concurrent Vibration and Thermal Loading," *International Journal of Damage Mechanics,* vol. 10, pp. 153-170, 2001.

[28] H. Ye, C. Basaran, D. C. Hopkins, and M. Lin, "Modeling Deformation in Microelectronics BGA Solder Joints Under High Current Density, Part I: Simulation and Testing," *Electronic Components and Technology Conference,* vol. 2, pp. 1437-1444, 2005.

[29] L. P. Lehman, R. K. Kinyanjui, L. Zavalij, A. Zribi, and E. J. Cotts, "Growth and Selection of Intermetallic Species in Sn-Ag-Cu No-Pb Solder Systems based on

Pad Metallurgies and Thermal Histories," *Electronic Components and Technology Conference,* pp. 1215-1221, 2003.

[30] L. P. Lehman, S. N. Athavale, T. M. Fullem, A. C. Giamis, R. K. Kinyanjui, M. Lowenstein, K. Mather, R. Pater, D. Rae, J. Wang, Y. Xing, L. Zavalij, P. Borgesan, and E. J. Cotts, "Growth of Sn and Intermetallic Compounds in Sn-Ag-Cu Solder," *Journal of Electronic Materials,* vol. 33, pp. 1429-1439, 2004.

[31] L. Snugovsky, P. Snugovsky, D. D. Perovic, T. Sack, and J. W. Rutter, "Some Aspects of Nucleation and Growth in Pbfree Sn-Ag-Cu Solder," *materials Science and Technology,* vol. 21, pp. 53-60, 2005.

[32] A. W. Gibson, S. L. Choi, K. N. Subramanian, and T. R. Bieler, "Issues Regarding Microstructural Coarsening Due to Aging of Eutectic Tin-Silver Solder," in *Reliability of Solders and Solder Joints, TMS*, R. K. E. Mahidhara, Ed., 1997, p. 97.

[33] P. L. Tu, Y. C. Chan, K. C. Hung, and J. K. L. Lai, "Growth Kinetics of Intermetallic Compounds in Chip Scale Package Solder Joint," *Scripta Materialia,* vol. 44, pp. 317-323, 2001.

[34] L. Qi, J. Huang, J. Zhang, and Y. Wang, "Microstructure and Intermetallic Growth at the Sn-Ag-Cu/Ni Interface after Thermal-shearing Cycling," *6th International Conference on Electronic Packaging Technology,* pp. 720-723, Sept 2005 2005.

[35] P. Arulvanan, Z. Zhong, and X. Shi, "Effects of Process Conditions on Reliability Microstructure Evolution and Failure Modes of SnAgCu Solder Joints," *Microelectronics Reliability,* vol. 46, pp. 432-439, 2006.

[36] T. Sayama, T. Takayanagi, Y. Nagai, T. Mori, and Q. Yu, "Evaluation of Microstructural Evolution and Thermal Fatigue Crack Initiation in Sn-Ag-Cu Solder Joints," *International Electronic Packaging Technical Conference and Exhibition,* pp. 749-756, July 2003 2003.

[37] I. Dutta, "A Constitutive Model for Creep of Lead-Free Solders Undergoing Strain-Enhanced Microstructural Coarsening: A First Report," *Journal of Electronic Materials,* vol. 32, pp. 201-207, 2003.

[38] M. V. Speight, "Growth Kinetics of Grain-Boundary Precipitates," *Acta Metallurgica,* vol. 16, pp. 133-135, 1968.

[39] A. J. Ardell, "On the Coasening of Grain Boudary Precipitates," *Acta Metallurgica,* vol. 20, 1972.

[40] M. M. Myshlyaev and O. N. Senkov, "Grain Growth in a Superplastic Zn-22% Al Alloy," *Acta Metall,* vol. 34, pp. 97-106, 1986.

[41] J. Lemaitre and J.-L. Chaboche, *Mechanics of Solid Materials*: Cambride University Press, 1990.

[42] N. E. Dowling, *Mechaniclal Behavior of Materials*, Second ed.: Prentice Hall, 1999.

[43] L. Anand, "Constitutive Equations for Hot-Working of Metals," *International Journal of Plasticity,* vol. 1, pp. 213-231, 1985.

[44] D. L. McDowell, M. P. Miller, and D. C. Brooks, "A Unified Creep-Plasticity Theory for Solder Alloys," *Fatigue of Electronic Materials,* vol. ASTM STP 1153, 1994.

[45] H. L. J. Pang, D. Y. R. Chong, and T. H. Low, "Thermal Cycling Analysis of Flip-Chip Solder Joint Reliability," *IEEE Transaction on Components and Packaging Technologies,* vol. 24, pp. 705-712, 2001.

[46] Ansys, "Ansys Theory Manual, Release 5.7. ch. 14," 1994, p. 107.

[47] Y. Guo and B. Han, "Thermal Deformation Analysis of Various Electronic Packaging Products by Moire and Microscopic Moire Interferometry," *Journal of Electronic Packaging,* vol. 117, pp. 185-191, 1995.

[48] F. Dai, J. McKelvie, and D. Post, "An Interpolation of Moire Interferometry from Wavefront Interference Theory," *Optics and Lasers in Engineering,* vol. 12, pp. 101-118, 1990.

[49] D. Post, B. Han, and P. Ifju, *High Sensitivity Moire*: Springer, 1994.

[50] Y. Guo, X. He, D. Zou, and S. Liu, "Phase-shifting Analysis in Moire Interferometry and its Applications in Electronic Packaging," *Opt. Eng,* vol. 37, pp. 1410-1419, 1998.

[51] Indium, "Product Data Sheet," in *Indium5.1 Pb-Free Solder Paste*: Indium Corporation of America, 2006.

[52] E. E. Underwood, *Quantitative Stereology*. Massachusetts: Addison-Wesley, 1970.

[53] R. T. Tummala, "Fundamentals of Microsystems Packaging," McGraw Hill, 2001.

[54] O. Salmela, "Acceleration Factors for Lead-Free Solder Materials," *IEEE Transaction on Components and Packaging Technologies,* vol. 30, pp. 700-707, 2007.

[55] K. A. Brakke, "The Surface Evolver," *Experimental Mathematics,* vol. 1, pp. 144-165, 1992.

[56] K. A. Brakke, *The Motion of a Surface by its Mean Curvature*. Princeton, NJ: Princeton University Press, 1977.

[57] K. R. Tunga, "Experimental and Theoretical Assessment of PBGA Reliability in Conjunction with Field-Use Conditions," in *Masters Thesis in Mechanical Engineering* Atlanta: Georgia Institute of Technology, 2004.

[58] Amkor, "Personal Communications with Doug Turnage from Amkor," 2008.

[59] E. P. Popov, *Engineering Mechanics of Solids*, Third Indian Printing ed.: Prentice hall of India, 1997.

[60] Isola-FR406, "Personal Communications with Staci Knight from Practical Components," 2007.

[61] Taiyo, "Personal Communications with John Fix from Taiyo America, Inc," 2007.

[62] A. Yeo, C. Lee, and J. H. L. Pang, "Flip Chip Solder Joint Reliability Analysis Using Viscoplastic and Elastic-Plastic-Creep Constitutive Models," *IEEE Transactions on Components and Packaging Technologies,* vol. 29, June 2006.

[63] J. Pyland, "Damage Metric-based Thermal Cycling Guidelines for Area-Array Packages Used in Harsh Thermal Conditions," in *Mechanical Engineering*. vol. Master of Science Altanta: Georgia Insititute of Technology, 2002.

[64] J. Lubliner, *Plasticity Theory*: Macmillan Publishing Company, 1990.

[65] R. Iannuzzelli, "Predicting Plated-Through-Hole Reliability in High-Temperature Manufacturing Process," *Proceedings of the 41st ECTC,* pp. 410-421, 1991.

[66] J. Lau and W. Dauksher, "Creep Constitutive Equations of Sn(3.5-3.9)wt%Ag(0.5-0.8)wt%Cu Lead-Free Solder Alloys," *Micromaterials and Nanomaterials,* pp. 54-62, 2004.

[67] J. Lau, W. Dauksher, and P. Vianco, "Acceleration Models, Constitutive Equations and Reliability of Lead-Free Solders and Joints," *IEEE Electronic Components and Technology Conference,* pp. 229-236, June 2003.

[68] P. Vianco, J. Rejent, and A. Kilgo, "Creep behavior of the ternary 95.5Sn-3.9Ag-0.6Cu solder—Part I: As-cast condition," *Journal of Electronic Materials,* vol. 33, pp. 1389-1400, November 2004.

[69] A. Schubert, R. Dudek, E. Auerswald, A. Gollhadt, B. Michel, and H. Reichl, "IEEE ECTC Proceedings," New Orleans, Louisiana, June 2003, pp. 603-610.

[70] J.-P. Clech, D. M. Noctor, J. C. Manock, G. W. Lynott, and F. E. Bader, "Surface Mount Assembly Failure Statistics and Failure Free Time," in *44th IEEE ECTC*, 1994.

[71] K. Tunga and K. S. Sitaraman, "An Expedient Experimental Technique for the Determination of Thermal Cycling Fatigue Life for BGA Package Solder Balls," *Journal of Electronic Packaging,* vol. 129, pp. 427-433, 2007.

[72] A. J. Hayter, *Probability and Statistics for Engineers and Scientists*: Duxbury Press, 2006.

[73] R. Darveaux, K. Banerji, A. Mawer, and G. Dody, "Reliability of Plastic Ball Grid Array Assembly," in *Ball Grid Array Technology*, J. Lau, Ed.: McGraw Hill, 1995.

[74] R. Darveaux, "Crack Initiation and Growth in Surface Mount Solder Joints," in *Proc. ISHM International Symposium on Microelectronics*, 1993, pp. 86-97.

[75] A. Schubert, R. Dudek, E. Auerswald, A. Gollhadt, B. Michel, and H. Reichl, "Fatigue Life Models for SnAgCu and SnPb Solder Joints Evaluated by Experiments and Simulation," *Micromaterials and Nanomaterials,* pp. 30-41, 2004.

[76] E. Nicewarner, "Historical Failure Distribution and Significant Factors Affecting Surface Mount Solder Joint Fatigue Life," in *Proc. IEPS*, September 1993, pp. 553-563.

[77] Y. Guo and J. S. Corbin, "Reliability of Ceramic Ball Grid Array Assembly," in *Ball Grid Array Technology*, J. H. Lau, Ed.: McGraw-Hill, 1995, pp. 223 - 265.

[78] JEDEC, "Temperature Cycling Standard - JESD22-A104C," Jedec Solid State Technology Association May 2005.